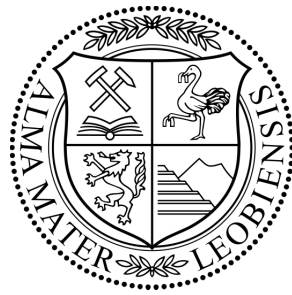


Gas-Oil Gravity Drainage in Naturally Fractured Reservoirs: Insights from a Discrete Fracture and Matrix Model

Theodor Videnberg, B.Sc.

March 2010



Master Thesis submitted to
Department of Mineral Resources and Petroleum Engineering
Chair of Reservoir Engineering
University of Leoben
in Partial Fulfillment
of the Requirements
for the Degree of

Master of Science

Supervised by: Univ.-Prof. Dr. Stephan K. Matthäi

Affidavit

I declare in lieu of oath, that I wrote this thesis and performed the associated research myself, using only literature cited in this volume.

Eidesstattliche Erklärung

Ich erkläre an Eides statt, dass ich diese Arbeit selbstständig verfasst, andere als die angegebenen Quellen und Hilfsmittel nicht benutzt und mich auch sonst keiner unerlaubten Hilfsmittel bedient habe.

Theodor Videnberg

March 2010

Abstract

According to estimates from the Schlumberger Market Analysis 2007, 60 % of fossil conventional hydrocarbons worldwide are located in naturally fractured reservoirs (NFR). In these reservoirs large volumes of hydrocarbons have been left untouched.

Gas-oil gravity drainage (GOGD) is a well-known production method that leads to high recoveries, while also being relatively inexpensive as compared to other production methods. It can occur naturally during gas cap expansion or when gas is actively injected at top of the reservoir. Gravitational forces then lead to a downward displacement of the oil, where both gas and oil are present. Although this process has been thoroughly examined for conventional reservoirs and in naturally fractured reservoirs using dual continuum approaches, very few publications exist on gravity drainage of NFR as simulated using discrete fracture and matrix approaches (DFM). This remains an active field of research explored by this thesis. My primary goal is to perform sensitivity analyses on the critical balance between capillary and gravity forces in NFR undergoing GOGD and to determine when gravity drainage is a feasible and recommended process. These questions are addressed with the help of a proprietary reservoir simulator based on the finite difference numerical method.

Three simplified models with a single vertical fracture and one more realistic layered discrete fracture and matrix model, based on field observations from Door County, Wisconsin, USA, were used as input to my simulations.

The conclusions reached for the chosen boundary conditions are that single vertical fractures do not significantly affect homogeneous models. Although the fracture helps drain the near-fracture region, the rock further away is left unaffected. Flow is mainly vertical and could be approximated by a piston-like displacement. This, however, is not the case in the more realistic model with layers. Here the fractures have a significant effect on the drainage speed and their presence increases recovery as compared with an unfractured model. The gas preferentially flows through the fractures and thereby by-passes horizontal low-permeability layers entering higher-permeability layers, where GOGD is initiated. The results also indicate that GOGD is strongly influenced by boundary conditions.

The sensitivity analysis also confirms the importance of well established critical factors like fluid density contrast, oil viscosity, relative permeability and capillary pressure. The thesis reaffirms the high production potential of gas-oil gravity drainage for NFR.

Kurzfassung

Gas-Öl Schwerkraft-Drainage (GOGD) ist eine wohlbekanntere Produktionsmethode, die zu hohen Gewinnungsraten führt und gleichzeitig relativ kostengünstig im Vergleich zu anderen Produktionsmethoden ist. Sie kann sowohl natürlich während der sogenannten Gas cap expansion als auch beim Einpressen von Gas im oberen Lagerstättenteil stattfinden. Gravitationskräfte verdrängen das Erdöl abwärts, bei gleichzeitiger Anwesenheit von Gas und Öl. Obwohl dieser Prozess schon gründlich für konventionelle Lagerstätten und für natürlich geklüftete Lagerstätten (NFR) mithilfe von Dual continuum-Modellen untersucht ist, existieren sehr wenige Publikationen, welche sich mit der Schwerkraft-Drainage mithilfe von Discrete fracture and matrix-Modellen beschäftigen. Dies ist ein aktives Forschungsgebiet, das durch meine Diplomarbeit untersucht wird.

Mein primäres Ziel ist das Durchführen von Sensitivitätsanalysen über die kritische Balance zwischen Kapillar- und Schwerkraft in NFR unter GOGD-Zuständen. Ich möchte auch die Bedingungen untersuchen, wann GOGD in NFR ein empfehlenswerter und vorteilhafter Prozess ist.

Diese Fragen werden mit Hilfe eines kommerziellen Reservoirsimulators, welcher auf der Finite-Differenzen-Methode basiert, adressiert. Drei einfache Modelle mit einer einzigen Kluft und ein realistischeres geschichtetes Discrete fracture and matrix-Modell, basierend auf Feldbeobachtungen aus Door County, Wisconsin, USA, werden als Input für meine Simulationen verwendet.

Ich komme zu dem Schluss dass eine einzelne Kluft ein homogenes Modell nicht ausreichend beeinflussen kann. Die Kluft beeinflusst die Region in ihrer Nähe, weiter entferntere Zonen werden nicht beeinflusst. Der Fluss ist vertikal und kann als piston-like displacement angenähert werden. Dies wurde jedoch nicht im realistischeren Modell beobachtet. Hier beeinflussen die Klüfte die Drainage-Geschwindigkeiten und können die Gewinnungsraten im Vergleich zu einem ungeklüfteten Modell erhöhen. Das Gas fließt vor allem durch die Klüfte und kann dadurch horizontal niedrig-permeable Schichten umgehen und tritt vorallem in den höher-permeablen Schichten ein, wo GOGD eingeleitet wird. Die Resultate deuten auch an, dass GOGD durch die Randbedingungen beeinflusst wird. Die Sensitivitätsanalyse bestätigen den Einfluss von kritischen Faktoren wie Dichtedifferenz der Flüssigkeiten, Ölviskositäten, relativen Permeabilitäten und Kapillardruck. Die Diplomarbeit bestätigt das hohe Potenzial der Gas-Öl Schwerkraft-Drainage in NFR.

Acknowledgements

I want to thank Professor Dr. Stephan Matthäi for supervising this thesis. I want to thank Professor Dr. Clemens Brand for answering my questions concerning numerical methods.

The help with CMG simulator and numerous fruitful and challenging discussions with Mr. Shaho Bazrafkan are also highly appreciated. My sincerest gratitude also goes to Dr. Julian Mindel, who always gave me good advice. It was a pleasure to have known those persons.

I would also like to thank the Austrian petroleum companies OMV and RAG for the support of Petroleum Engineering at the University of Leoben under the Petroleum Engineering Program for Excellence (PEPE) and for using PEPE hard- and software.

“Omnia ad maiorem Dei gloriam.”

Motto of the Societas Iesu

“Don’t ever let somebody tell you... You can’t do something. You got a dream... You gotta protect it. People can’t do somethin’ themselves, they wanna tell you you can’t do it. If you want something, go get it. Period.”

Will Smith in “The Pursuit of Happyness”

“If you know the enemy and know yourself, you need not fear the result of a hundred battles. If you know yourself but not the enemy, for every victory gained you will also suffer a defeat. If you know neither the enemy nor yourself, you will succumb in every battle.”

Sun Tzu in “The Art of War”

Dedication

I dedicate this master thesis to my family:

To **Galina Laleva Decheva**, my mother, who raised me alone in a foreign country and without the support of anybody. She has always been a wonderful and protective mother to me and has taught me to love learning.

To **Lalio Georgiev Dechev** (1938-2009), my grandfather, who taught me numerous important lessons in life and whom I really loved and admired. He was a wonderful person, whose early death shocked me and made me depressed.

To **Ruska Hristova Decheva** (1939-2009), my grandmother, who aided my mum a lot in upbringing and educating me and who frequently took me along to church, where I started to love God.

Nomenclature

S_o	oil saturation, dimensionless
S_{or}	residual oil saturation, dimensionless
S_w	water saturation, dimensionless
S_{wr}	residual water saturation, dimensionless
S_{wi}	initial water saturation, dimensionless
S_g	gas saturation, dimensionless
S_e	effective saturation, dimensionless
z	z-position, L
x	x-position, L
z_D	dimensionless z-position
g	gravitational acceleration, L/t ²
k	permeability, L ²
k_r	relative permeability, dimensionless
k_x	permeability in x-direction, L ²
k_z	permeability in z-direction, L ²
k^*	end-point relative permeability, dimensionless
f	fractional flow, dimensionless
ϕ	porosity, dimensionless
μ_o	oil viscosity, m / Lt
t	time, t
t_D	dimensionless time
q	flow rate, L ³ /t
\hat{q}	flow rate per unit volume, 1/t
$\Delta\rho$	density difference, m/L ³
h	height, L
A	flow area, L ²
R	recovery, dimensionless
$GOGD$	gas-oil gravity drainage
$SAGD$	steam-assisted gravity drainage
NFR	naturally fractured reservoir
$1D, 2D, 3D$	one dimensional, two dimensional, three dimensional
p_o	oil pressure, m/Lt ²
p_w	water pressure, m/Lt ²

p_g gas pressure, m/Lt²
 p_c capillary pressure, m/Lt²
 $p_{c,thr}$ threshold capillary pressure, m/Lt²
 η pore size distribution
 J Leverett J-function for capillary pressure
 λ Brooks-Corey exponent parameter, dimensionless
 α, n, m Van Genuchten parameters, dimensionless
 N_{Bo} Bond number, dimensionless
 N_{gv} Gravity number, dimensionless
 B_w water formation volume factor, dimensionless
 σ interfacial tension, m/t²
 v Darcy velocity, L/t
 c compressibility, Lt²/m
 c_ϕ rock compressibility, Lt²/m
 c_t total system compressibility, Lt²/m
 Θ wetting angle, dimensionless
 D depth, L
 γ specific gravity, m/L²t²
 Φ potential, m/Lt²
 Φ_i Basis function, dimensionless
 λ_o oil mobility, Lt/m
 λ_w water mobility, Lt/m
 λ_g gas mobility, Lt/m

Conversion factors

To Convert From	To	Multiply By
$^{\circ}F$	K	$T_K = (T_F + 459.67) / 1.8$
psi	Pa	6.894757 $E + 03$
ft	m	3.048 $E - 01$
md	m^2	9.869233 $E - 16$
lbs/ft^3	kg/m^3	1.601846 $E + 01$
cp	$Pa.s$	1.000 $E - 03$
bbl	m^3	1.589873 $E - 01$

Contents

Affidavit	ii
Abstract	iii
Kurzfassung	iv
Acknowledgements	v
Dedication	vii
Nomenclature	viii
List of Tables	1
List of Figures	3
1 Introduction	4
1.1 Literature Review	5
1.2 Claim	7
1.3 Agenda	8
2 Methodology	9
2.1 Governing Equations	9
2.1.1 Continuity Equation	9
2.1.2 Darcy's law	10
2.1.3 Saturation Equation	10
2.1.4 Immiscible Two-Phase Slightly Compressible Flow	11
2.2 Non-Equilibrium Gravity Drainage	12
2.3 Gas-Oil Gravity Drainage	13
2.4 Mathematical Models	15
2.5 Factors Affecting Drainage Rates	16
2.6 Fracture Capillary Pressure	17
2.7 Significance of Bond Number	18
2.8 CMG Reservoir Simulator	20
2.8.1 Introduction	20
2.8.2 Model Building Procedure	21
2.8.3 Models and Boundary Conditions	23
2.8.4 Initialization and Properties	28

2.8.5	Limitations of CMG simulator	35
3	Results / Analysis	36
3.1	Effect of general parameters	36
3.2	Effect of number and position of fractures	43
3.3	Effect of fracture permeability	44
3.4	Effect of fracture capillary pressure	49
3.5	Effect of relative permeability	50
3.6	Effect of bottomlayer matrix permeability	54
3.7	Cooke model simulation results	59
4	Discussion	72
5	Conclusions	75
	List of References	77
	Appendix A	83
	Appendix B	92
	Appendix C	125
	Vita	132

List of Tables

1	Gas-water capillary pressure values used as default in models 1,2, and 3	29
2	Default properties used for models 1, 2 and 3	31
3	Gas formation volume factor versus pressure	32
4	Gas viscosity versus pressure	33
5	Brooks-Corey parameters used for initialization of shale layers in Cooke model	35
6	Brooks-Corey parameters used for initialization of dolomite layers in Cooke model	35
7	Recovered oil for different specific gas gravities in Cooke model	64
8	Recovered oil for different oil densities in Cooke model	64
9	Recovered oil for different oil viscosities in Cooke model	65
10	Material properties for default simulation	112
11	Different shape factor constants in literature	129

List of Figures

1	Schematic of GOGD in field applications	14
2	Fracture capillary pressure	18
3	Finite difference stencils	21
4	Conceptual picture of model 1	24
5	Conceptual picture of model 2	25
6	Gas-water capillary pressure curve used for models 1,2, and 3	28
7	Relative permeability used for models 1,2, and 3	29
8	Relative permeability used for fracture	30
9	Fracture map of Door County, Wisconsin, and simplified model used for simulation	32
10	Effect of matrix permeability on water volume	36
11	Effect of matrix porosity on water volume	37
12	Saturation profiles for different boundary conditions	38
13	Effect of capillary pressure for model 1	40
14	Effect of water density	41
15	Change in saturation distribution with time for model 1	42
16	Effect of fracture length for model 2	44
17	Effect of fracture permeability on water volume	46
18	Effect of fracture permeability	47
19	Effect of fracture permeability for model 2	48
20	Effect of fracture capillary pressure on model 2	50
21	Effect of non-wetting phase relative permeability curvature on GOGD	52
22	Influence of gas Brooks-Corey exponent on relative permeability and capillary pressure	52
23	Effect of wetting phase relative permeability on GOGD	54
24	Influence of water Brooks-Corey parameter on relative permeability	54
25	Effect of bottomlayer permeability on model 3	56
26	Effect of layer sequence on model 3	57
27	Influence of matrix permeability on recovery in homogeneous Cooke model	60
28	Water saturation for Cooke model	62
29	Water saturation for Cooke model	62
30	Effect of fractures on recovery	63

31	Influence of pore size distribution index in dolomite on recovery from Cooke model	67
32	Influence of dolomite pore size distribution index on relative permeabilities and capillary pressure	67
33	Influence of dolomite threshold capillary pressure	68
34	Wetting phase velocity in z-direction in Cooke model	71
35	Voronoi grid with control volume ³⁴	95
36	Triangle finite element	96
37	Linear FE basis functions	98
38	Barycentric finite volumes ³⁸	102
39	1D finite-element finite-volume discretisation of a Darcian fluid flow ³⁹	103
40	Numerical solution procedure	104
41	Quadratic B-spline basis functions (a) NURBS curve (b) ³⁷	108
42	Permeability of continuous fracture model	112
43	Gas saturation of continuous fracture model after 2.5 days	113
44	Gas saturation of continuous fracture model after 13.9 days	113
45	Gas saturation of continuous fracture model after 27.8 days	114
46	Bottomlayer fracture gas saturation after 16.67 hrs	115
47	Integrated gas saturation over time	116
48	Inflow and outflow over time for continuous fracture model	117
49	Effect of bottomlayer permeability on gas saturation	118
50	Effect of bottomlayer permeability on threshold height	119
51	Effect of oil density on gas saturation	120
52	Effect of oil viscosity on gas saturation	120
53	Gas saturation histogram for different oil viscosities	121
54	Conceptual picture of discontinuous fracture model	121
55	Gas saturation of discontinuous fracture model after 2.5 days	123
56	Gas saturation of discontinuous fracture model after 13.9 days	123
57	Gas saturation of discontinuous fracture model after 27.8 days	124
58	Inflow and outflow over time for discontinuous fracture model	124

1 Introduction

According to estimates more than 60 percent of the fossil conventional hydrocarbons are estimated to be in naturally fractured reservoirs (NFR). These are preferentially in carbonate reservoirs in the Middle East and northern Africa.

According to Nelson [2001]⁵⁷ a fractured reservoir is defined as a reservoir in which naturally occurring fractures either have or a predicted to have an effect on reservoir fluid flow either in the form of increased reservoir permeability and/or reserves or increased permeability anisotropy. These fractures are planar discontinuities in the rock that can be produced by natural means, due to earth stresses and tectonics, or through artificial means, such as well stimulation or drilling. The matrix is the part of the porous medium, which contains most of the fluid volume and it is intersected by the fractures. In many cases, the matrix has a very low permeability in the micro-Darcy range and is therefore an impediment to flow.

A fracture can significantly change the flow behaviour because it is a high-velocity flow conduit and a reservoir heterogeneity with directional effects.⁴⁰

Every reservoir can be considered to be fractured to some degree.⁴⁰ The process of drilling can create fractures in the vicinity of the wellbore and the well itself can be considered as an artificial fracture. The processes of hydraulic and acid fracturing can also create fractures. However, in some reservoirs the existence of fractures does not play an enhancing role to the flow process and the fractures can be neglected, these reservoirs can be called conventional reservoirs.

Unfortunately, NFRs behave in a completely different way than conventional reservoirs. In NFRs the flow of fluids is a complex combination of viscous, gravity and capillary forces. Moreover, the number of parameters necessary for modelling and simulation is much larger than in conventional reservoirs. Obtaining those parameters for example for fractures can be also a challenging task and not so trivial. The underlying physical principles are also more complex than in conventional reservoirs.

There are several different strategies to recover oil from fractured reservoirs. Each of those depends on the specific properties of the reservoir and its fracture and matrix regions. There is no general rule, but decisions have to be made on an individual basis. One method that can be water flooding the reservoir and producing oil mainly through the fractures. To be successful this method requires that the water from the fractures imbibes into the matrix and oil is drained from there.

Another process is gas-oil gravity drainage, also known as GOGD. It can occur in response to natural and artificial means. Gas is being injected into the fractures, which due to physical reasons like capillary and gravity forces, causes oil drainage of the fracture-adjointing matrix regions into the fracture network through which the oil can be subsequently produced. The GOGD method has huge potential and leads to very high oil recovery factors. It has already been used, i.e. by PEMEX off-shore Mexico.

Water injection and GOGD can lead to unsatisfying results and low oil recovery rates, when they are not optimised for the target. Injecting water at too high rates can lead to fingering so that many regions of the reservoir remain untouched and production is mainly water.

Previous simulations of GOGD in NFR have almost entirely been done with dual continuum models (DCM), based on simplifications and idealisations. Although those models are relatively easy to understand and implement, many modifications to the original model have been proposed over the years to improve predictions. Confusion exists over the shape factor concept and whether fractures can be treated as a continuum. The reader may be referred to Appendix C for further details.

1.1 Literature Review

The theory of gravity drainage was established in the 1940's.

Leverett [1941]¹ presented experimental data and investigated capillary effects, interfacial tension and saturation-height relationships for unconsolidated sand. He also mentioned the boundary effect, a characteristic behaviour of any discontinuity in capillary properties. His work gives a starting point for further research by exploring the capillary effects.

Katz [1942]² presented both field and experimental data and discussed possibilities of secondary recovery, i.e. water flooding and gas injection, in the Wilcox sand of Oklahoma City. The significance of this publication is that it deals with the Wilcox reservoir, where gravity drainage has been a major recovery factor.

Stahl et al. [1943]³ presented an experimental study of gravitational drainage of oil and transient height-saturation curves for unconsolidated sand from the Wilcox region in Oklahoma. Stahl et al. are one of the first authors to perform a gravity drainage experiment and determine that the saturation to height relationship will follow the capillary pressure form. They use findings from Leverett [1941]¹ and Katz [1942],² substantiate it and deal with the performance of

certain types of reservoirs.

Cardwell and Parsons [1949]⁴ presented a mathematical formulation of the gravity drainage of a wetting liquid. By neglecting capillary pressure gradient terms they were able to solve the complicated differential equation analytically. They introduced the concept of a demarcator, and could solve the saturation profiles in a stack over time and subsequently estimate oil recovery. The significance of their work is that they try a mathematical formulation to account for variation in permeability to the liquid. They do not, however, take into account capillary effects.

Terwilliger et al. [1951]⁵ conducted experimental studies on gravity drainage, developed a mathematical formulation of the drainage process and recommended a method to calculate the oil recovery rate. They used a Buckley-Leverett⁶ approach in their derivation to calculate the performance of immiscible fluid displacement processes. Terwilliger et al. expand knowledge of gravity drainage from previous studies of Leverett [1941],¹ Katz [1942]¹ and Stahl et al. [1943].³

Dykstra [1978]⁷ expands the Cardwell-Parson's approach to account for residual oil saturation deriving a recovery function as a function of time. He presents the drainage modulus, a property that can be used to predict performance, and cross-validated his analytical results with experimental data. Dykstra also presents examples of how to apply the method. His work strictly deals with predicting oil recovery under free-fall gravity drainage.

Hagoort [1980]⁸ derives the governing equations for forced and free-fall gas-oil gravity drainage processes and arrives at an expression similar to that of Cardwell and Parsons. Forced gravity drainage refers to gas injection and controlled flow rate, which occurs when gas is injected into steeply dipping reservoirs. Free-fall gravity drainage, on the other hand, takes place in NFRs, after gas injection into fractures or depletion of oil in the fractures.¹¹ He also conducts an experimental test to determine oil relative permeabilities from a centrifuge. Hagoort also introduces the gravity number and capillary number in a dimensionless formulation. His results indicate that oil relative permeability is a key factor. Hagoort confirms that gravity drainage can be effective-oil recovery process in water-wet reservoirs and mentions that the magnitude of gravitational forces relative to viscous forces, shape of oil relative permeability, and reservoir geometry and heterogeneity as important factors.

Rossen and Shen [1989]⁹ describe a method of simulating gas-oil drainage and water-oil imbibition in a dual-porosity simulator by using pseudo capillary curves for matrix and fracture. Their work indicates the problematic use of

dual-porosity methods and mentions that different shape factors lead to different behaviours.

Saidi and Sakthikumar [1993]¹⁰ describe various aspects of gravity drainage in fractured reservoirs, including capillary pressures and relative permeability effects as well as diffusion. They emphasize on those effects in combination with gas injection into the reservoirs. They also give a thorough review on research and experimental data concerning these topics. Their work indicates 1D and 3D GOGD give same results and that the use of a fracture capillary pressure increases recovery factor of a block. These findings are directly related to further results of models in this thesis.

Schechter and Guo [1996]¹¹ give a thorough literature review on equilibrium and non-equilibrium gravity drainage deriving a new mathematical formulation for free-fall gravity drainage using Darcy's law and film flow theory. They also present a method to include the numerical solution of the diffusion equation to expand their mathematical formulation to non-equilibrium gravity drainage. The significance of their work is the exact definition of free-fall and forced gravity-drainage in fractured reservoirs, as well as a proposed mathematical coupling of equilibrium and non-equilibrium gravity drainage.

The interactive design of a carbon-dioxide injection pilot in Texas is presented in Schechter and Guo [1998].¹² They present a methodology for matrix and fracture characterization and conduct experiments on fluid-transfer mechanisms.

Li and Horne [2003]¹³ proposed a modified model to predict the oil recovery in free-fall gravity drainage and the average residual oil saturation and discussed the effect of pore size distribution and capillary entry pressure on gravity drainage.

Laboratory experiments of gravity drainage in fractured rock have been seldomly performed. Some recent studies from Zendehboudi et al. [2008;⁴⁶ 2009⁴⁵] of free-fall gravity drainage experiments indicate that the presence of fractures is more significant for low matrix permeability systems. They also found out that the rate of liquid exchange between fractures and matrix is dependent on the liquid level heights in the fractures and the matrix. Their work indicates that free-fall gravity drainage seems to be stable and piston-like displacement process; even in the presence of fractures.

1.2 Claim

Carrying out this research is motivated by the fact that fractured reservoirs

are still very poorly understood and modelled, even though they contain large amounts of hydrocarbons. Discrete fracture and matrix (DFDM) models are used more sheldomly than dual continuum models (DCM), especially in simulating gravity drainage problems. Injecting gas into fractured reservoirs and therefore enhancing the rate of oil drainage from the matrix blocks is a highly promising production technique. Conceptual models exist for idealized cases and idealized matrix block shapes, however more realistic geological (i.e. discrete) models have been rarely reviewed.

The goal of this study is to gain insight into the physics of gas-oil gravity drainage with the help of single-porosity conceptual models and a structured discrete fracture and matrix model, based on field observations from Wisconsin. For this purpose cross-sectional gravity drainage models have been used with the commercial CMG reservoir simulator. The primary tasks accomplished by this thesis are (a) to perform a sensitivity analyses on the critical variables, (b) examine the role of capillary and gravity effects, and (c) determine when gas-oil gravity drainage in NFR is a feasible and recommended process.

1.3 Agenda

Chapter 1 gives an introduction to gas-oil gravity drainage. **Chapter 2** explains the methodology and describes the methods used in accomplishing the set tasks. **Chapter 3** deals with the results and analysis of the simulation results. **Chapter 4** gives a discussion of findings from this thesis. **Chapter 5** gives a conclusion and makes some recommendations concerning gas-oil gravity drainage in naturally fractured reservoirs. **Appendix A** gives the .dat-file that was used for simulation of the Cooke model. **Appendix B** is an experimental section and deals with CSMP++ reservoir simulator, that was also used for some simulations. **Appendix C** gives a general overview of dual continuum models and discusses their implications and idealizations.

2 Methodology

Gravity drainage is a very powerful recovery mechanism with potentially high recovery potential and efficiencies. One of its biggest advantages is the fact that gravity drainage is a natural process, does not need much additional energy input and can keep the reservoir pressure high for a relatively long period. Conditions of free-fall gravity drainage can occur when gas is injected directly into the fracture system or when the fractures are drained from the oil. In such a case the matrix blocks are surrounded by gas to some degree and oil starts to drain out. However gravity drainage can be a time-consuming process, which has to be balanced and set into relation with economic and management considerations.

2.1 Governing Equations

Unfortunately, the exact mathematical formulations of IMEX reservoir simulator of CMG are not known and are nowhere discussed. I assume that CMG company are reluctant to give away too much detail and harm their own business interests. Therefore, the following sections are simply based on my own derivations.

2.1.1 Continuity Equation

The starting point of the mathematical derivation of the equations that I have used to simulate GOGD is the continuity equation. It can be obtained by applying a mass balance on a infinitely small volume object and using a Taylor series expansion and ignoring higher order terms on the facelets and is defined as

$$-\nabla \cdot (\rho \vec{v}) = \frac{\partial \rho}{\partial t} \quad (2.1)$$

where ρ is fluid density in mass per unit volume, v is fluid velocity and t is time. For incompressible flow the right-hand side of the equation becomes zero. The equation above is only valid for single-phase flow and porosity of unity. Dealing with a multi-phase flow and a porous medium, porosity and saturation need to be included, as well as source/sink terms to yield

$$-\nabla \cdot (\rho_\alpha \vec{v}_\alpha) + \rho_\alpha \hat{q}_\alpha = \frac{\partial (\rho_\alpha \phi S_\alpha)}{\partial t} \quad (2.2)$$

$$\alpha \in \{o, g, w\}$$

where \hat{q} is the source/sink term in inverse of time, S is the phase saturation i.e. volume fraction of the pore space that is occupied by α (i.e. oil, gas, water) and ϕ is porosity. In the equation above the gravity component is inherent but not visible yet.

2.1.2 Darcy's law

Darcy's law is named after the French hydrologist Henri Darcy who in 1856 discovered a simple linear relationship between the flow rate of water through sand and the pressure gradient. The proportionality constant depends on the flow area, fluid properties (i.e. viscosity) and rock properties (i.e. permeability). For petroleum engineering applications, however, the equation is written in its multi-phase form, which is

$$\vec{v}_\alpha = -\frac{k_{r\alpha}}{\mu_\alpha} k (\nabla p_\alpha - \rho_\alpha \vec{g}) \quad (2.3)$$

where k_r is the relative permeability, k is the permeability tensor, μ is the viscosity, p is the fluid pressure and $\vec{g} = [0, 0, -g]^T$ is the gravitational acceleration vector. The relative permeability is a function of phase saturation (e.g Brooks-Corey, Stone, Van Genuchten). The expression in the brackets is the gradient of the flow potential.

2.1.3 Saturation Equation

The saturation equation can be derived from Eq.2.2 with mathematical modifications. If we assume that fluid density is constant, the rock matrix incompressible (i.e. porosity is constant), and the fluids phases are immiscible then we obtain the classical saturation equation which is similar to the Buckley-Leverett equation⁶

$$-\nabla \cdot \vec{v}_\alpha + \hat{q}_\alpha = \phi \frac{\partial S_\alpha}{\partial t} \quad (2.4)$$

If we deal with gas-oil gravity drainage, however, this simple form of the saturation equation will not be applicable. For gas gravity drainage the equation used will be a two-phase, slightly compressible and immiscible flow.

2.1.4 Immiscible Two-Phase Slightly Compressible Flow

In order to derive the immiscible two-phase slightly compressible flow the starting point is Eq.2.4. Especially the right hand side of the equation needs further refinement. Applying the product rule of differential calculus twice we obtain

$$\frac{\partial (S_\alpha \rho_\alpha \phi)}{\partial t} = S_\alpha \frac{\partial (\rho_\alpha \phi)}{\partial t} + \rho_\alpha \phi \frac{\partial S_\alpha}{\partial t} = S_\alpha \left[\phi \frac{\partial \rho_\alpha}{\partial t} + \rho_\alpha \frac{\partial \phi}{\partial t} \right] + \rho_\alpha \phi \frac{\partial S_\alpha}{\partial t} \quad (2.5)$$

Since density and porosity are a function of phase pressure we can expand the expression within the square brackets of Eq. 2.5 to account for phase pressure

$$\phi \frac{\partial \rho_\alpha}{\partial t} + \rho_\alpha \frac{\partial \phi}{\partial t} = \phi \frac{\partial \rho_\alpha}{\partial p_\alpha} \frac{\partial p_\alpha}{\partial t} + \rho_\alpha \frac{\partial \phi}{\partial p_\alpha} \frac{\partial p_\alpha}{\partial t}$$

With the introduction of fluid compressibility, which is the measure of relative density change of a fluid with pressure at constant temperature, as well as rock compressibility

$$c_\alpha = \frac{1}{\rho_\alpha} \frac{\partial \rho_\alpha}{\partial p_\alpha}$$

$$c_\phi = \frac{1}{\phi} \frac{\partial \phi}{\partial p_\alpha}$$

and the insertion of Darcy velocity of Eq.2.3 into Eq.2.2 as well as the introduction of phase mobility $\lambda_\alpha = k_{r\alpha}/\mu_\alpha$ we obtain the following expression

$$-\nabla \cdot (-\rho_\alpha \lambda_\alpha k (\nabla p_\alpha - \rho_\alpha \vec{g})) + \rho_\alpha \hat{q}_\alpha = S_\alpha \phi \rho_\alpha (c_\alpha + c_\phi) \frac{\partial p_\alpha}{\partial t} + \rho_\alpha \phi \frac{\partial S_\alpha}{\partial t} \quad (2.6)$$

$$\alpha \in \{o, g\}$$

Eq.2.6 is also known as the full saturation equation. Note that in this derivation the fluid compressibilities are being treated as constant (i.e. slightly compressible). If gas is desired to be treated as fully compressible then its compressibility should be a function of pressure and Z-factor. We also know that the sum of the individual saturations is unity

$$\sum S_\alpha = 1$$

and the mathematical definition of capillary pressure p_{cgo} in an oil-gas system

$$p_{cgo} = p_g - p_o$$

where the subscripts g and o denote gas and oil respectively. Under the assumption that the capillary pressure derivative with respect to time is negligibly small, individually adding up the expressions in Eq.2.6 and after some mathematical transformations we obtain the immiscible two-phase slightly compressible flow equation

$$\nabla \cdot [k(\rho_o \lambda_o + \rho_g \lambda_g) \nabla p - k \vec{g} (\rho_o^2 \lambda_o + \rho_g^2 \lambda_g) + \rho_g \lambda_g k \nabla p_{cgo}] + \rho_o \hat{q}_o + \rho_g \hat{q}_g = \quad (2.7)$$

$$\phi [S_o \rho_o (c_o + c_\phi) + (1 - S_o) \rho_g (c_g - c_\phi)] \frac{\partial p}{\partial t} + \phi (\rho_o - \rho_g) \frac{\partial S_o}{\partial t}$$

Eq.2.7 above is stated as a pressure and saturation formulation. The permeability tensor is denoted by k. The pressure p refers to the oil pressure. The saturation is evaluated for oil and subsequently the gas saturation can be found.

Another formulation that gets rid of the saturation- time derivative can be obtained from the knowledge that the sum of saturations is always unity. Again, by neglecting the capillary pressure derivative with respect to time and by definition of the total compressibility $c_t = S_o c_o + S_g c_g + c_\phi$ and the total source term $\hat{q}_t = \hat{q}_o + \hat{q}_g$ we obtain the so-called pressure equation³³

$$\frac{1}{\rho_o} \nabla \cdot [\rho_o \lambda_o k (\nabla p - \rho_o \vec{g})] + \frac{1}{\rho_g} \nabla \cdot [\rho_g \lambda_g k (\nabla p + \nabla p_{cgo} - \rho_g \vec{g})] + \hat{q}_t = \phi c_t \frac{\partial p}{\partial t} \quad (2.8)$$

where p again denotes the oil pressure. Eq.2.8 is well suited for an IMPES (i.e. implicit pressure explicit saturation) approach in solving the equation numerically.

2.2 Non-Equilibrium Gravity Drainage

Non-equilibrium gravity drainage takes place when gases such as carbon dioxide are injected that are not in thermodynamic equilibrium with the oil in

the reservoir. In such cases both phases do not coexist in an immiscible state but a modified phase is established. The idea of non-equilibrium gravity drainage is to inject a gas that will mix with the oil reducing the interfacial tension and altering the capillary pressure function. If a certain layer had a height that was smaller than the capillary threshold height, then in equilibrium gravity drainage this layer would have been left untouched. The capillary threshold height can be calculated by dividing the threshold capillary pressure. Non-equilibrium gravity drainage permits to drain such layers.

Unfortunately, non-equilibrium gravity drainage is more complicated because compositional effects need to be taken into account. Therefore there are only few publications addressing this topic (e.g., Schechter and Guo [1996];¹¹ Jacquin et al. [1989]⁵⁵).

2.3 Gas-Oil Gravity Drainage

Naturally fractured reservoirs (NFR) often contain numerous fissures and fractures. In such reservoirs the use of waterflooding as a recovery method would lead to early water breakthroughs, high water production rates and a large amount of oil would be left untouched in the reservoir. Therefore GOGD in NFR can be a potentially advantageous production method.

In field applications GOGD is established by a combination of horizontal or vertical injector wells at the top of the reservoir and a producing well at the bottom of the reservoir. Figure 1 presents a schematic of this process. A horizontal injector generally is better because it intersects more vertical fractures than a vertical but due to financial or mechanical constrictions a horizontal injector is not always available.

In GOGD gas is injected at the top of the reservoir and then creates a gas-oil interface that is displaced downwards towards the horizontal producer at the bottom of the reservoir. Gas injection rates and oil production rates are balanced and controlled to make sure that the entire system is dominated by gravity effects. The injected gas then replaces the voidage volume created by the simultaneous oil production.

If production and injection rates are not balanced accurately, viscous fingering, early gas breakthrough and gas coning can occur.⁵⁶ This effects negatively affects the recovery of GOGD processes.

Assuming low viscous forces GOGD can be regarded as a continuous battle between gravitational forces that tend to displace the oil downward and capillary

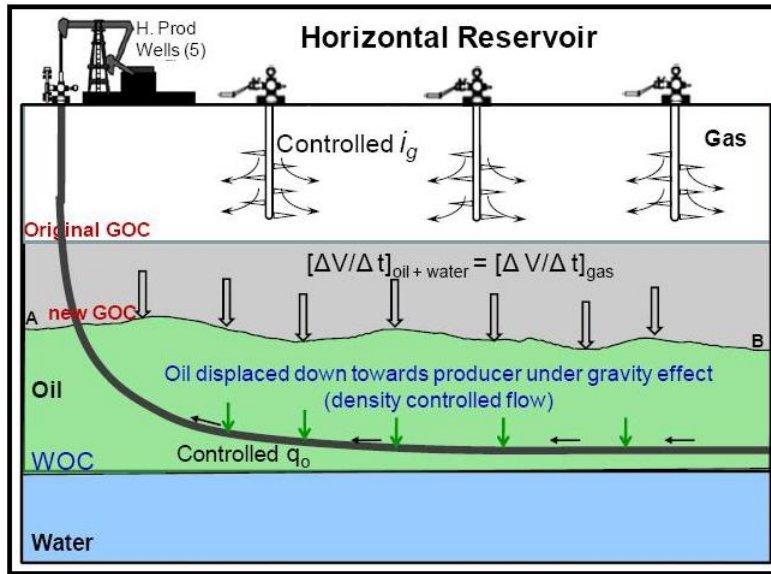


Figure 1: Schematic of GOGD in field applications (after Jadhawar and Sarma, 2008)⁵⁶

forces (rock-specific characteristic) that try to hold it back.

In theory, gravity drainage can take place in any stage of the producing life of the reservoir. Hagoort [1980]⁸ mentions that GOGD “can occur in primary stages of oil production (gas cap expansion drive or segregation drive), as well as in supplemental stages where gas is supplied from an external source”. Ideally the reservoir would be produced at pressures above the bubble point pressure, where gas is still dissolved within the oil. This is positive, because oil viscosity generally is smaller. Moreover, keeping the pressure in the undersaturated region prevents shrinkage of oil in place.

GOGD simulations in NFR have mainly been done with dual continuum models, following certain idealisations and assumptions for computational speed. Dual continuum models are relatively simple to implement and understand. Such simulations have been done with both brine or oil as the wetting phase and gas as the non-wetting phase. Terwilliger et al. [1951]⁵ have stated that there is very little difference between displacement of oil or water by gas. Some authors have also found out that GOGD in 3D can be closely approximated by 1D (e.g., Saidi and Sakthikumar [1993]¹⁰). This finding supports the setup of models within my thesis.

2.4 Mathematical Models

In the past, several authors have tried to present mathematical models to deal with gravity drainage. Some of these models are presented below:

Luan⁵¹ derives analytical solutions for gravity drainage by starting with the Darcy velocity of the oil phase and the continuity equation. Moreover from the definition of capillary pressure he comes up with a 1D reimbibition model for matrix blocks of NFRs.

$$\phi \frac{\partial S_o}{\partial t} + \frac{\Delta \rho_{og} g k'_{ro}}{\mu_o} \frac{dS_o}{dz} + \phi \sqrt{\frac{k}{\phi}} \frac{\partial}{\partial z} k_{ro} J' \frac{dS_o}{dz} = 0 \quad (2.9)$$

where J denotes the Leverett J-function. The last term of the above equation is the capillary term, which can be neglected in some conditions and under certain assumptions. He then introduces a capillary length scale and some parameters to create a dimensionless version of the above equation.

Correa et al.⁴⁹ examine the theory of gravity drainage in layered porous media. They start by mathematically describing gravity drainage in homogeneous media. They come up with the following differential equation for isothermal immiscible flow with constant porosity and an incompressible oil phase

$$\frac{\partial}{\partial z} \left[\frac{k_{ro}}{k_{ro}^o} \left(\Delta \rho g - \frac{\partial P_c}{\partial t} \right) \right] = \frac{\phi \mu_o dS_o}{k k_{ro}^o dP_c} \frac{\partial P_c}{\partial t}$$

where k_{ro}^o is the endpoint oil relative permeability value. Correa et al. then introduce dimensionless variables for the height, time and potential and come up with the respective dimensionless formulation. This formulation is expanded for layered models and leads to an initial rate of drainage

$$q_{oi} = \frac{\bar{k} A \Delta \rho g}{\mu_o} \left(1 - \frac{h_2^o}{h} \right)$$

where \bar{k} is the harmonic average permeability, h is the total height of the model and h_2^o is the threshold height as obtained from the capillary pressure function. The above equation is however only valid for single phase flow.

Schechter and Guo¹¹ also developed a mathematical model to describe free-fall gravity drainage. Based on Darcy's law and film flow theory they create a dimensionless equation for phase demarcator as a function of dimensionless time and also present an equation for oil recovery

$$R = \left(1 - \frac{S_{wr}}{S_{wi}}\right) z_D - \frac{2z_D}{3S_{wi}} \sqrt{\frac{F_s \phi z_D}{5t_D}}$$

where z_D is the dimensionless position of the demarcator, F_s is the correction factor to the Kozeny equation, S_{wi} is the initial wetting phase saturation, and t_D is the dimensionless time defined as $t_D = k_{eff} \Delta \rho g t / \mu L$. The demarcator can be regarded as the interface position between two phases. At this position the capillary pressure is constant. The Kozeny equation is used to calculate the pressure drop of a fluid through a bed of rock.

Li and Horne¹³ argue that previous mathematical models to of oil production by gravity drainage are not very successful. Therefore they propose an empirical oil recovery model that matches and predicts oil recovery in gravity drainage problems. The recovery is defined by the following expression

$$R = \frac{1 - S_{wi} - \bar{S}_{or}}{1 - S_{wi}} (1 - e^{-\beta t})$$

where β is a constant giving the rate of convergence, \bar{S}_{or} is the average residual oil saturation and S_{wi} is the initial water saturation. The parameters above can be obtained by a history match. Li and Horne also present an equation for the initial oil production rate by gravity drainage. The equation can be viewed as a multiphase extension of the single-phase oil rate formula given previously by Correa et al.

$$q_{oi} = \frac{A k k_{ro}^* \Delta \rho g}{\mu_o} \left(1 - \frac{p_d}{\Delta \rho g L}\right)$$

where p_d is the entry (or threshold) capillary pressure and L is the block height. In case of horizontal fractures the block height could be related to fracture spacing, however, the case of vertical fractures remains unclear.

2.5 Factors Affecting Drainage Rates

Permeability. Increased absolute permeability and especially vertical matrix permeability accelerates gravity drainage (e.g. Schechter and Guo [1998]¹²), but does not increase final recovery (e.g. for $t \rightarrow \infty$). Oil relative permeability is a key factor in gas-oil gravity drainage (e.g. Hagoort [1980]⁸).

Capillary pressure. The lower the threshold capillary pressure, the smaller is the capillary holdup zone. The shape of the capillary pressure curve determines

the final recovery: The smaller the capillary pressure is and the more uniform the grain sizes, the better is the final recovery and the higher is the amount of recoverable oil. The existence of fracture capillary pressure increases oil recovery from blocks (e.g. Saidi and Sakthikumar [1993]¹⁰).

Density difference. The larger the difference between density of the wetting phase and density of the non-wetting phase the more efficient is gravity drainage and the higher is the final recovery (e.g. Saidi and Sakthikumar [1993]¹⁰). In gas-oil gravity drainage studies the density of the gas is neglected sometimes. The gravitational force in gravity drainage problems is directly proportional to the absolute density difference of the wetting and non-wetting phases. Therefore, GOGD seems to be a reasonable recovery mechanism for heavy oil.

Viscosity. The viscosity of the oil (i.e. non-wetting phase in GOGD) determines the production rate. The higher the viscosity the slower does the oil drain from the matrix block. This effect is made advantage of in steam-assisted gravity drainage (i.e. SAGD), where the oil viscosity should be decreased by the injection of hot gas.

Interfacial tension. Studies have found out that the reduction in interfacial tension increased the oil recovery (e.g. Karimaie and Torsaeter [2008]⁵⁰). Interfacial tension is directly related to the capillary pressure and a reduction thereof leads to a reduced capillary pressure. For miscible displacements the capillary pressure of the phases disappears.

2.6 Fracture Capillary Pressure

Accurate knowledge of the capillary pressure curve is extremely important. Especially in NFRs capillarity plays a crucial role in the driving mechanism; much more than in conventional reservoirs. However, the shape and the use of capillary pressure within fractures has been a controversial issue and has caused a lot of disputes between scientists.

Several authors have suggested to neglect capillary pressures in fractures and treat the phase pressures as equal (e.g. Kazemi et al. [1979];²¹ Fourar et al. [1993]²²). This assumption came into popularity by a publication by Romm [1966],²³ who conducted experiments of flow between parallel plates. Treating the capillary pressure as zero has its justifications in the parallel-plate idealization, in the assumption of wide fracture apertures and hence decreasing capillary effects, as well as in a simplification of the governing equations. Moreover, direct measurement of fracture capillary pressure- saturation relationships still pose

logistical and experimental shortcoming and difficulties.

More recent publications by Firoozabadi and Hauge [1990],²⁴ Rangel-German et al. [2006]²⁵ reject the assumption that capillary pressure within the fractures can be neglected. Their research and experiments show the opposite. Firoozabadi and Hauge’s work found that fracture capillary pressure is both a function of aperture and roughness of the fracture wall. De la Porte et al. [2005]²⁶ examined the effect of the assumption of zero fracture capillary pressure on results of numerical simulation of naturally fractured reservoirs and presented guidelines for the selection of relative permeability and capillary pressure curves in fractures.

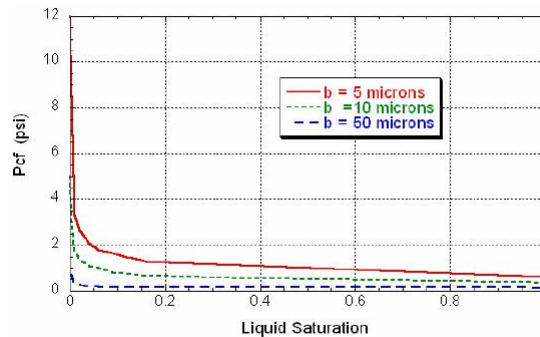


Figure 2: Fracture capillary pressure (after de la Porte et al. [2005])²⁶

To sum up, although still more work on fracture capillary pressure- saturation relationships is needed, I think that the general properties of the capillary pressure curve should be the following: non-zero capillary entry pressure, almost constant value over a large portion of the wetting phase saturation and a very low irreducible wetting phase saturation. Further developments are necessary to develop a fracture capillary pressure.

2.7 Significance of Bond Number

The Bond number is a dimensionless number in the field of fluid mechanics and gives the ratio of body (i.e. gravitational) forces to surface tension (i.e. capillary) forces. When dealing with fractured reservoirs usually the inverse

of the Bond number is of importance. Its effect has been studied by Du Prey [1978]²⁷ and Schechter et al. [1994]²⁸ and is defined as

$$N_{Bo}^{-1} = \frac{P_c}{P_g} = \sqrt{\frac{k}{\phi}} \frac{\sigma \cos \theta}{\Delta \rho g h_f} \quad (2.10)$$

where N_{Bo} is the Bond number, k and ϕ are matrix block permeability and porosity, σ and θ are the interfacial tension and the wetting angle respectively, g is the gravitational acceleration and h_f is the height of the fracture. The term $\sqrt{k/\phi}$ comes from the Leverett J-function and denotes a mean characteristic pore radius. The result of the equation has no units. The inverse Bond is a simple relationship that can help in determining the question, whether a flow is governed by capillary or gravity forces respectively. High values of N_{Bo}^{-1} indicate that the flow is governed by capillarity, while low values indicate that the flow is gravity-driven.

Schechter et al. [1994]²⁸ investigated the effect of low interfacial tensions on drainage and imbibition. They observed that gravity drainage from a matrix block begins when N_{Bo}^{-1} is less than one. Schechter et al. also argue that changing N_{Bo}^{-1} value changes the flow regime; a high inverse Bond number indicate capillary-driven counter-current flow, while low inverse Bond numbers indicate gravity-driven and segregated cocurrent flow. Cocurrent flows have higher relative permeability curves than counter-current flows.

2.8 CMG Reservoir Simulator

2.8.1 Introduction

The gas-oil gravity drainage simulations were performed with the commercial IMEX® black oil simulator from Computer Modelling Group (CMG). This section will describe the mathematical principles of the software and its limitations. It will also deal with the simulation models, the boundary conditions and the assumptions involved.

IMEX is the three-phase black-oil simulator from CMG. It includes viscous, capillary and gravity terms in the equations. IMEX makes use of the finite difference numerical method to solve the involved partial differential equations. Based on the FD technique IMEX uses Cartesian or cylindrical coordinate systems. It can solve the PDEs in explicit, fully implicit and by adaptive implicit modes. IMEX can be used to simulate single porosity (discrete) models and dual continuum models (dual porosity, dual permeability, MINC), which are a model representation for naturally fractured reservoirs.

The finite difference method (FD) is the oldest numerical method for the approximation of solutions to partial differential equations. It makes use of the Taylor series expansion, where a function in a future position is related to the function of the present position and derivatives of the function at the present position. Obviously, in order to decrease the complexity of the differential equation the derivative is being replaced with a difference quotient.

$$\frac{\partial p}{\partial x} \approx \frac{\Delta p}{\Delta x} = \frac{p_2 - p_1}{x_2 - x_1}$$

In order to apply the FD method the Taylor polynomial needs to be shortened, by neglecting higher order terms and just applying the Taylor series expansion till first order. The finite difference method is therefore first order accurate. To calculate the differences, one can use forward, backward or a combination of both called central differences. The solution of the PDE is more closely approximated by having a small grid size. The finite difference method can be used with several possible stencils, the two most popular being the 5-point and the 9-point formulation.

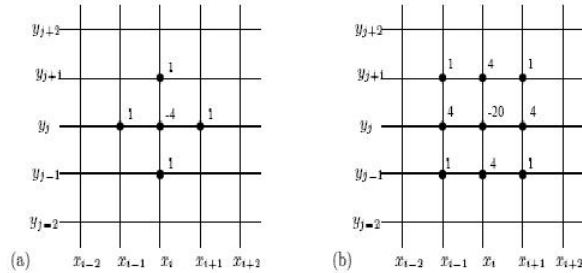


Figure 3: Finite difference 5-point formulation (a) 9-point formulation (b) (after LeVeque, 2006)³⁶

Fig.3 above gives a graphical illustration of the different stencils. The number close to the node refers to the contributions of the nodes to the finite differences. The 5-point formulation uses one central node and its north-south and east-west neighbours to compute the derivatives, while the more sophisticated 9-point formulation includes all adjacent neighbours (i.e.north east- and south-west neighbours etc.) to the central node. IMEX uses the 9-point formulation. The finite difference method can be applied to regular grids (e.g. Cartesian grid) and leads to structured grids. Different ordering of the structured grid would lead to different matrixes A to be inverted during simulation runs. In any instance, this assembled matrix would have unzero values along certain diagonals.

To sum up, the finite difference method is the oldest numerical method to solve PDEs, however it can only handle regular meshes. This means that the FD method has problems in dealing with complex geological features and therefore realistic geometries.

2.8.2 Model Building Procedure

The first step is the starting of the CMG Launcher, which is a project management application that allows the user to keep track of his simulations. In the Launcher the paths and directories are specified and a user-friendly menu manages the applications. From the Launcher various different applications like STARS, Builder and IMEX can be started by a “drag and drop” method.

The reservoir model and the simulation input files are created with the

Builder. The Builder has a model tree view that guides the user through the model setup in a step-by-step fashion. In the first step the user has to specify the simulator (GEM, IMEX, or STARS), the working units (SI, field, or lab units), the porosity model (single porosity, dual porosity, dual permeability, MINC, or subdomain) and the simulation start date. Then the grid type, K direction and number of grid blocks and the grid block dimensions in I-J-K-direction need to be specified. After having created the grid, it needs to be filled with properties. Properties include porosities, permeabilities (in I-J-K-directions), reference depths, grid thickness, bubble point pressures, and dispersion coefficients among others. Properties can be specified either for the entire grid, or for certain layers. It is also possible to access certain grid blocks manually and change parameters.

The next step is to define the component properties of the model. The user can select between a black-oil model and a gas-water model. In this section basically the PVT properties (e.g. solution gas-oil ratio, viscosity etc.) of the fluids in the model are specified as functions over pressure.

Then the so-called rock-fluid properties need to be defined. This section refers to the definition of different rock types (e.g. shale, limestone etc.) and the introduction of relative permeability-functions and capillary pressure-functions. The user can define the name of the rock, the wettability of the rock (either water wet or oil wet), relative permeability (numerical values can be entered manually with linear interpolations in between or correlations can be used instead) and capillary pressure curves. Relative permeability hysteresis can also be modelled.

After defining the rock-fluid properties, the initial conditions of the model need to be specified. This is of course necessary as to give an unique solution to the partial differential equations that are solved with the CMG reservoir simulator. The initial conditions menu are divided into 3 parts: calculation methods, PVT region parameters, and advanced parameters. In the calculation menu tab the user can define how the block saturation is initialized (for the models 1 to 3 user specified pressure and saturation values are assigned to each grid block). In the PVT region parameters like phase contact depths, capillary pressure at phase contacts and datum depth for pressure need to be defined among others. The advanced parameters tab deals with the gas cap initialization.

The last required step before a simulation can be started is the numerical section. Here the user can define numerical properties and numerical solution parameters. These include the minimum time step size, maximum time step

cuts, linear solver precision, linear solver factorization, linear solver iterations, and linear solver orthogonalizations among others. In real world examples the user can define those parameters to manage the needs. If the model is huge the user can decrease linear solver precision and numerical matrix manipulations in order to increase simulation speed and shorten simulation runs. In our case those numerical possibilities in CMG reservoir simulator are not fully exploited because the used models are fairly small. A typical simulation run for models 1, 2 or 3 lasts for approximately 2 to 3 minutes.

2.8.3 Models and Boundary Conditions

For this simulation study several different models have been built.

The first model (subsequently referred to as **model 1**) has a simple geometry and should mimic the behaviour of a core. The simulation model used was the gas-water approach because the CMG simulator does not offer the possibility of gas-oil components only. This simplification seems to be reasonable since in a real static reservoir water would be at irreducible saturation and therefore immobile. The only draining phase would be the oil.

The model is a rectangular cross-section of reservoir rock with a continuous fracture from top to bottom. The fracture is located in the center of the reservoir rock. The top, bottom and left and right boundaries are gas-filled and have high permeabilities. The rock model has no-flow left and right boundaries (which were established by setting the permeability to zero on the rock boundaries). This ensures that hydrocarbon fluids can only leave the model through the bottom, both through the fracture and the matrix.

Another simple model with a low-permeability layer on the bottom was created (subsequently referred to as **model 2**). The only difference between model 1 and model 2 therefore is the existence of a low-permeable bottom layer. This would automatically lead to a decreased fluid displacement through the matrix block and I would be able to observe the effect of single and multiple fractures. The gravity head of the wetting phase would create a vertical force; however, the existence of the horizontal low-permeable layer in the bottom would force the oil to flow in horizontal direction to the fracture. A picture of model 2 is displayed below (not drawn to scale).

The third model (subsequently referred to as **model 3**) was created to analyze the effect of fractures when the matrix has multiple layers of different permeabilities. Model 1 can be regarded as a simplified model 3. Model 3 has

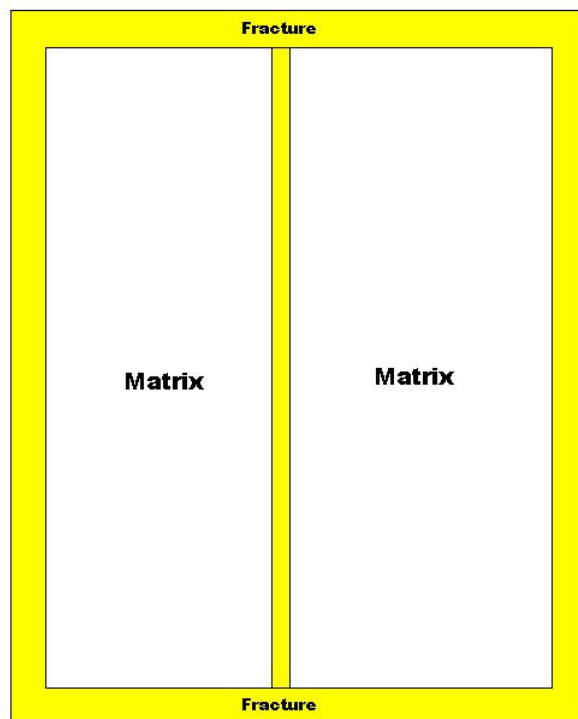


Figure 4: Conceptual picture of model 1(not to scale)

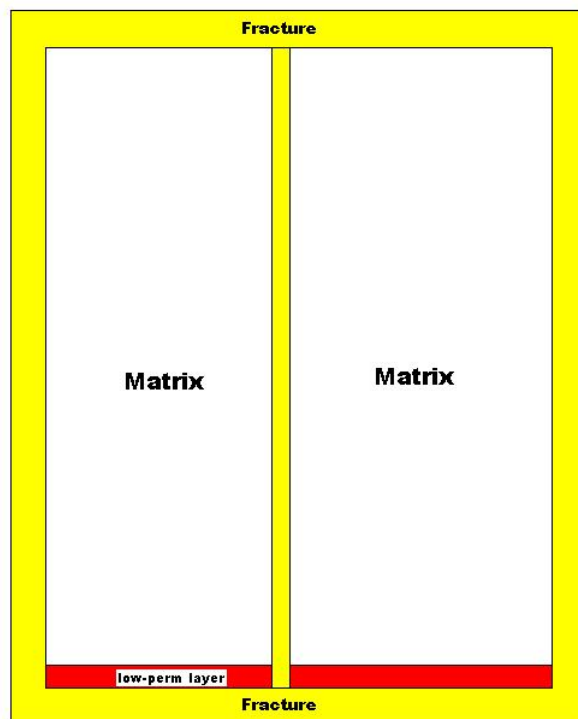


Figure 5: Conceptual picture of model 2(not to scale)

the same dimensions and properties as model 1. The only difference is that the matrix block has a reduced permeability in its lower half. The permeability was modified between 5 md and 25 md. The upper layer's permeability was kept constant at 50 md. That model was simulated and results were compared between the fractured and the non-fractured case.

A more realistic fractured cross-section of an NFR analog was taken from Cooke et al. [2006]⁴⁴ and will be referred to as **Cooke model**. In their publication the authors examined the influence of stratigraphy on fracture growth and termination and its meaning for subsurface fluid flow processes. They investigated fracture termination for two different carbonate rock sequences: one Silurian dolomite from Door County, Wisconsin, and the other being the Cretaceous Austin Chalk from Texas. Cooke et al. found that the mechanical properties of interfaces of layers control whether an initiated fracture would terminate or not. Therefore, the mechanical unit thickness not only influences the fracture height but also fracture spacing. This publication also mentions that the fracture spacing is broadly proportional to fracture height and that thicker layers therefore develop longer, widely spaced fractures than thinner layers. Cooke et al. also address the issue of groundwater flow. They believe that their findings could be useful for estimation of equivalent porous permeability and hydraulic conductivity and models that use discrete fracture networks.

Cooke et al. [2006]⁴⁴ presents various figures in their original publication that include sedimentary stratigraphy, mechanical stratigraphy and fracture map among others. The original Cooke model fracture map can be found on the top right corner on page 229 of the prementioned publication. Apart from the fracture map the sedimentary and mechanical stratigraphies are presented. The sequence consists mainly of Silurian dolomite and is located in the Door Peninsula, Wisconsin.

Unfortunately, the original Cooke model is complicated due to the numerous fractures (more than 100) and layers (about 20) of varying lengths and thicknesses. As gridding of such a model is far from trivial it was decided to make simplifications to ease the creating of the discrete fracture and matrix model in the CMG reservoir simulator. Therefore, the model had to be simplified, making several assumptions:

- Fractures that terminate within mechanical units (i.e. layers) are disregarded.

- Very thin layers are disregarded.
- All layers are assumed to be horizontal.
- Fractures are assumed to be vertical.
- Only those fractures with a certain minimum length (i.e. in this case I set the threshold length to be at least one half of layer thickness) are considered.
- In the x-direction the coordinate of the higher fracture tip was considered.
- If certain layers with a high matrix permeability fractures were neglected.
- All fractures that penetrate multiple layers or are in contact with the interface to layers thus establishing a flow conduit between those were represented.
- The fractures in the 2D model do not intersect each other in 3D. Therefore the 2D model is believed to be an appropriate representation of 3D reality.

Giving all those simplifications a new representative Cooke model was created, which consists of 8 horizontal layers and 52 vertical fractures (Fig.9). Its dimensions are 16 by 16 meters.

While models 1 to 3 could be built by manually adjusting the properties of the fracture grid, the realistic Cooke model could not be created in the CMG Builder with these primitive procedures. The fractures were numbered from 1 to 52, mainly from left to right of the Cooke model. The next step was to determine the exact position of the fractures and the extent of the layers in terms of coordinates. This was done with the help of the free digitizing software Engauge Digitizer 4.1 by Mark Mitchell. I loaded the Cooke model as a bitmap file into the digitizer and defined three points and their coordinates. Then the exact horizontal and vertical coordinates of the fractures can be determined. Simple mathematical operations lead to grid cell thicknesses, which can be entered without problems in CMG Builder.

2.8.4 Initialization and Properties

Simulation start date needs to be specified early in the model building procedure. A default simulation start date was chosen to be January 1, 2000.

The gas-water capillary pressure function for the models 1 to 3 was generated automatically by the CMG Builder with the help of correlations. For the particular problem of course the drainage cycle of the capillary curve was used and no hysteresis modelled. The irreducible water saturation was set at 15 percent. The plot of the gas-water capillary pressure curve is presented below.

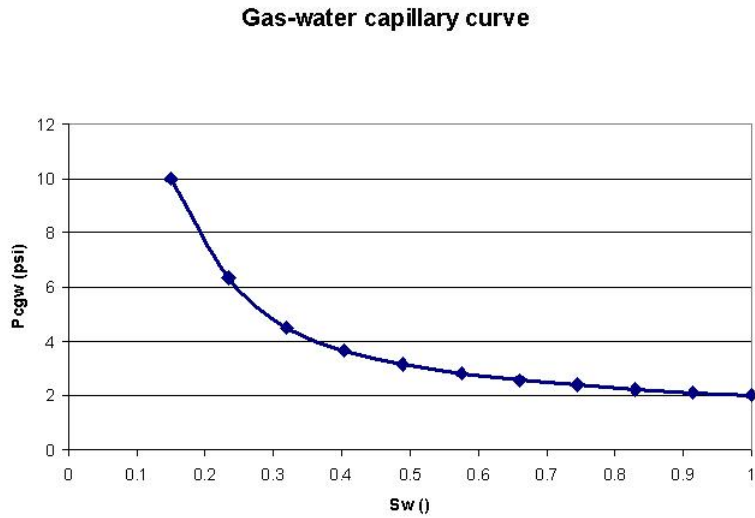


Figure 6: Gas-water capillary pressure curve used for models 1,2, and 3

On the x-axis the water saturation as a fraction is presented, while on the y-axis the capillary pressure of the gas-water system is presented in psi. At an irreducible water saturation of 0.15 the gas-water capillary pressure is 10 psi. The threshold pressure at which gas enters the model is set to 2 psi. As initially no gas is present in the model the threshold pressure corresponds to a water saturation of one. The figure above is valid only for the rock material grids of the models. For the fracture domain a gas-water capillary pressure function of zero is assumed, which is a proper assumption because of the wide fracture aperture. An approximation of a zero capillary pressure within the fractures is also found in other research publications.

$S_w()$	$P_{c_{gw}}(\text{psi})$
0.15	10
0.235	6.32
0.32	4.47
0.405	3.65
0.49	3.16
0.575	2.83
0.66	2.58
0.745	2.39
0.83	2.24
0.915	2.11
1	2

Table 1: Gas-water capillary pressure values used as default in models 1,2, and 3

For the relative permeability functions the drainage cycle was used and they were generated within CMG with the help of correlations.

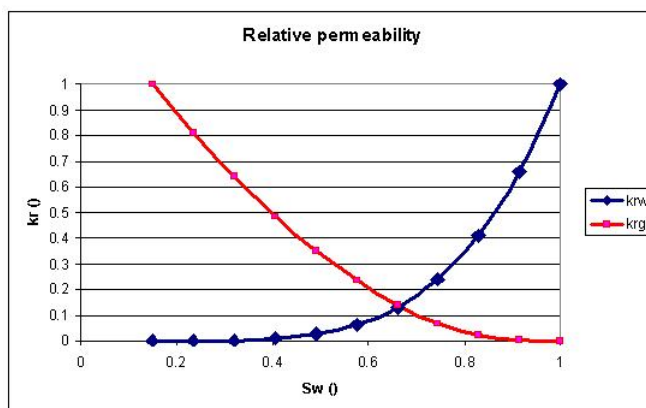


Figure 7: Relative permeability used for models 1,2, and 3

On the x-axis the wetting phase saturation (i.e. in our case it is water) is displayed in increasing order, while on the y-axis the dimensionless relative permeabilities of gas and water are displayed. It was assumed that the end-point relative permeabilities are one. This approximation can be considered justifiable because at an initial water saturation of one (i.e. a fully water saturated core with water) only water is available for flow. For a connate water saturation of 15 percent the gas relative permeability was set to one. The wettability of the system was set to water-wet. The wettability character can be seen in the

relative permeability figure from the intersection point between water and gas relative permeability curves. The position of the intersection point confirms water-wet conditions.

For the fracture domain linear relative permeability relationships were used. The endpoint relative permeability values are one. It is assumed that in the fracture there is a zero connate water saturation. This is a plausible assumption for parallel-plate fractures or fractures, whose walls have a low roughness.

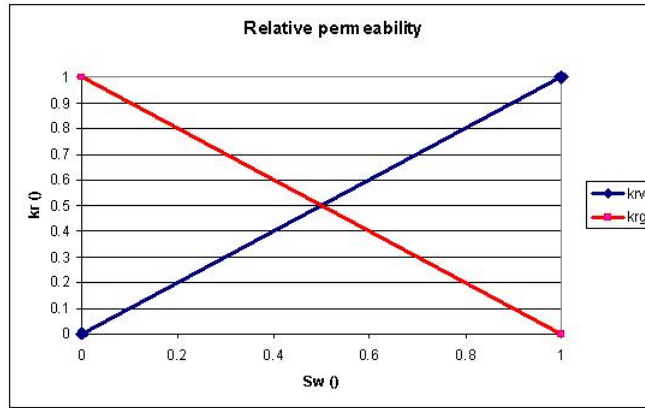


Figure 8: Relative permeability used for fracture

In the fracture relative permeabilities the following formulas were used.

$$k_{rw}(S_w) = S_w$$

$$k_{rg}(S_w) = 1 - S_w$$

Linear relative permeability curves as defined above have also been used in previous research publications.

Other properties that have been used for the default initialization purposes for models 1 to 3 are shown below in Table 2. The properties are given in field units (e.g. psi, md, etc.) because the models 1,2 and 3 were designed in field units.

Table 4 presents the relationship between pressure and gas formation volume factor that was used in the default model simulations. The gas formation volume

Property	Value
ϕ_f	0.999
ϕ_m	0.2
k_m	50md
k_f	$10^6 md$
c_w	$3.19387 * 10^{-6} psi^{-1}$
c_ϕ	$10^{-5} psi^{-1}$
T_{res}	100°F
SG_{gas}	0.8
ρ_w	62.04lbs/ft ³
B_w	1
μ_w	1cp
P_{res}	500psi

Table 2: Default properties used for models 1, 2 and 3

factor (B_g) is the quotient of the gas volume at reservoir conditions and gas volume at standard conditions. It can be viewed as an exchange rate about how to refer reservoir volumes to surface volumes. The behaviour is absolutely typical and consistent. The higher the pressure becomes, the lower is the gas formation volume factor (i.e. a large pressure means that larger volumes of gas can be compressed which results in larger surface volumes).

Table 4 presents the gas viscosity versus pressure that was used for the default simulations. The viscosity-pressure relationship is almost linear with a very small curvature.

For an explanation of the used variables and abbreviations please refer to the nomenclature.

Pressure (psi)	B_g (bbl/ft ³)
14.696	0.190628
80.38	0.0344016
146.07	0.0186825
211.76	0.0127149
277.44	0.00957258
343.13	0.00763312
408.82	0.00631672
474.51	0.00536481
540.19	0.00464444
605.88	0.00408047
671.57	0.00362709
737.25	0.00325486
802.94	0.002944
868.63	0.00268071
934.31	0.00245511
1000	0.00225991

Table 3: Gas formation volume factor versus pressure

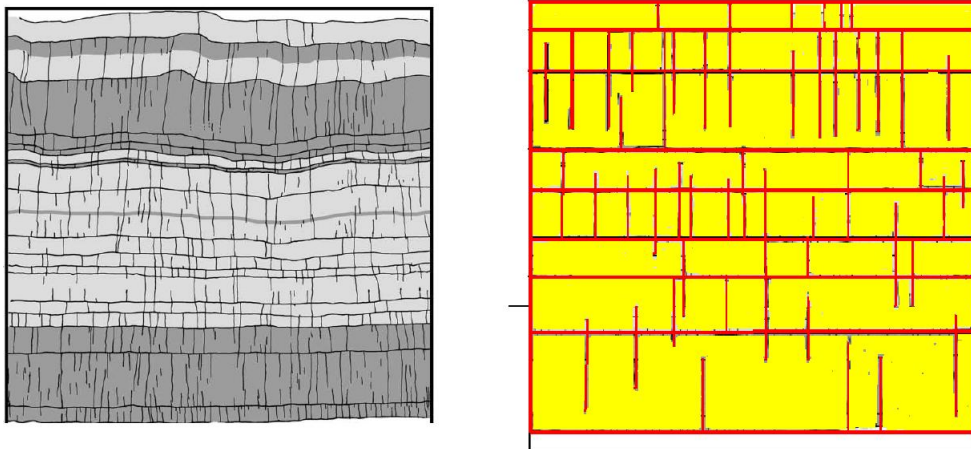


Figure 9: Fracture outcrop map of Door County, Wisconsin, (left),⁴⁴ simplified model used for simulation (right). The original Cooke model fracture map can be found on the top right corner on pg.229 of the Cooke et al. publication

The figure above presents the original Cooke model on the left side and the simplified Cooke model on the right side that was used in the simplifications. The Cooke model has dimensions of $16m \times 16m$. The horizontal red lines rep-

Pressure (psi)	μ_g (cp)
14.696	0.0106345
80.38	0.0107085
146.07	0.010804
211.76	0.0109149
277.44	0.0110394
343.13	0.0111768
408.82	0.0113272
474.51	0.0114907
540.19	0.0116677
605.88	0.011859
671.57	0.0120651
737.25	0.0122868
802.94	0.0125251
868.63	0.0127808
934.31	0.0130548
1000	0.0133481

Table 4: Gas viscosity versus pressure

represent the interfaces between the individual layers, while the vertical red lines represent the fractures. The matrix blocks are displayed in yellow. Please notice, that the colours have no meaning whatsoever and should not represent same properties. They are just meant as a visual guidance.

Unfortunately, Cooke et al.[2006]⁴⁴ do not give any numerical values for the properties of the outcrop study in their Silurian dolomite model from Door County,WI. They only present the mechanical and sedimentary stratigraphy but neither give fracture apertures, nor porosities or permeabilities. This is of course a setback in the aim of realistically modelling the example. Therefore, it was chosen to assume numerical values for the properties that were unknown. This was done based on several principles.

For the fracture aperture I assumed a value of $1mm$. With its help an intrinsic permeability can be defined with the help of

$$k_f = \frac{w_f^2}{12} = \frac{(10^{-3}m)^2}{12} = 8.33 \times 10^{-8}m^2 \approx 83300d$$

I considered this value to be non-physical. I assumed that during the dolomitization process this absolute fracture aperture would be modified (i.e. decreased) by crystallization processes. Therefore I assumed that this high intrinsic fracture permeability would be lower; I chose a more realistic fracture

permeability value to be $10^6 md$. Backcalculating from this fracture permeability value I obtain an effective (i.e. for free-flow) fracture aperture of $0.1mm$. This would mean that the initial fracture aperture would be 90%-blocked with crystals, thus leaving eventually just $0.1mm$ open to flow and therefore a fracture permeability of $10^6 md$.

For the permeability in the matrix block regions of the Cooke model I and my advisor Dr. Stephan Matthäi decided to use typical permeability values for dolomites. The dark regions in figure 3 (C) of Cooke et al. [2006]⁴⁴ represent lower permeability regions, while the lighter-coloured regions represent higher permeability regions. The darker regions are thought to represent shale regions, which are generally characterized by low permeabilities and relatively large crystal particles. The brighter-coloured regions are thought to represent Silurian dolomite regions from Door County, Wisconsin. As for the permeability extreme values of $1md$ (for dark regions) and $100md$ (for brighter regions) were chosen.

For the porosity values I used a typical value of 0.2 for the dolomite rocks. The fractures have a porosity that is close to unity; it was chosen to be 0.999 (CMG simulator does not allow a 100% porosity). Unfortunately, those low permeable shale layers have an unknown porosity; therefore, I decided to use a typical porosity value (i.e. 6%) for the fairly well-analyzed Barnett Shale (e.g., Utley [2005],⁵² Reed [2007]⁵³) in Texas. This of course introduces a certain amount of uncertainty.

For the relative permeability functions of the shale and dolomite regions a Brooks-Corey model was used. In the fracture a linear relative permeability was used. The modified Brooks-Corey drainage equations use the following formulas

$$k_{rw} = k_{rw}^* (S_e)^{3+2/\eta}$$

$$k_{rg} = k_{rg}^* (1 - S_e)^{1+2/\eta}$$

$$P_c = P_{c,thr} (S_e)^{-1/\eta}$$

where S_e is the effective (normalized) saturation and η is a measure of the maximum pore size distribution.

Parameter	Value
k_{rw}^*	1
k_{rg}^*	0.5
S_{wr}	0.18
P_{thr}	1psi

Table 5: Brooks-Corey parameters used for initialization of shale layers in Cooke model

Parameter	Value
k_{rw}^*	1
k_{rg}^*	0.7
S_{wr}	0.15
P_{thr}	1.5psi

Table 6: Brooks-Corey parameters used for initialization of dolomite layers in Cooke model

2.8.5 Limitations of CMG simulator

Since IMEX is a finite-difference simulator it is restricted to regular meshes and therefore has problems in representing realistic features. Layer boundaries that are curves can only be represented as steps. The geometry can only be refined by a decrease of the global dimensions of the grid blocks. Unfortunately, this comes at the expense of computational efficiency. Another setback is that IMEX is restricted to certain model sizes and number of grid blocks. The University of Leoben licence can handle a maximum of 50 000 grid blocks.

3 Results / Analysis

3.1 Effect of general parameters

In this section the effect of general parameters is examined, in order to gain some insights into the process of gravity-drainage and make some sensitivity analysis on governing parameters. The extra gain from this simulations might be the establishment of general criteria over when gravity-drainage might be an option of recovering the hydrocarbons.

In the first several simulation runs the matrix permeability [50 md, 100 md, 250 md, 500 md] was modified. It generally accepted that the higher the matrix permeability the faster does the oil drain from the model. This is absolutely intuitive because permeability is directly related to the drainage velocity through Darcy equation. The above mentioned principle can also be observed for the simulated model 1. In the subsequent plot the average water saturation in percent is on the y-axis, while the date of simulation is on the x-axis. It can be observed that a high matrix permeability increases the drainage velocity. Please notice also that the matrix is open to flow; therefore the existence of a fracture does not improve the drainage performance.

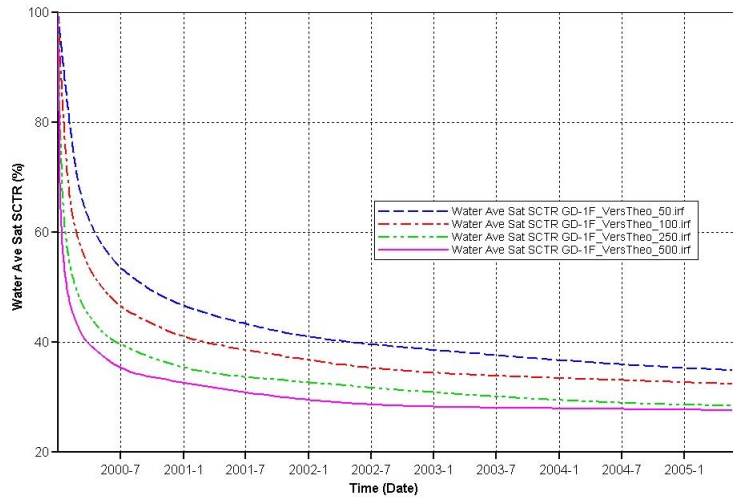


Figure 10: Effect of matrix permeability for model 1

The difference in average water saturation can be dramatic especially for the early time-period of the simulation. The longer the simulation runs the more do the drainage curves approach each other. In the end of the simulation the final water saturation for the 50 md case it is about 35 percent; 32.4 percent, 28.5 percent and 27.7 percent for the respective cases of 100 md, 250 md, and 500 md. To sum up, matrix permeability is one of the main governing parameters for the success of gravity drainage.

Several other simulation runs have shown that a decrease in matrix porosity in model 1 also increases the drainage velocity. At first this observation seemed odd to me, however, it is also intuitive and has a simple explanation. The drainage velocity of the matrix block is related to the interstitial velocity, which is the Darcy velocity divided by the porosity [$u = v/\phi$]. The interstitial velocity can be thought of as the velocity of the fluid within the pores. Therefore the lower the porosity the higher will be the interstitial velocity. Generally, there is no mathematical relation between porosity and permeability of a reservoir, although some attempts have been made. In many cases a low porosity will also mean a low permeability, but this is not always the case. The plot below shows the average water saturation in percent on the y-axis and the simulation date on the x-axis. This behaviour was obtained by keeping the permeability unchanged, while modifying the porosity.

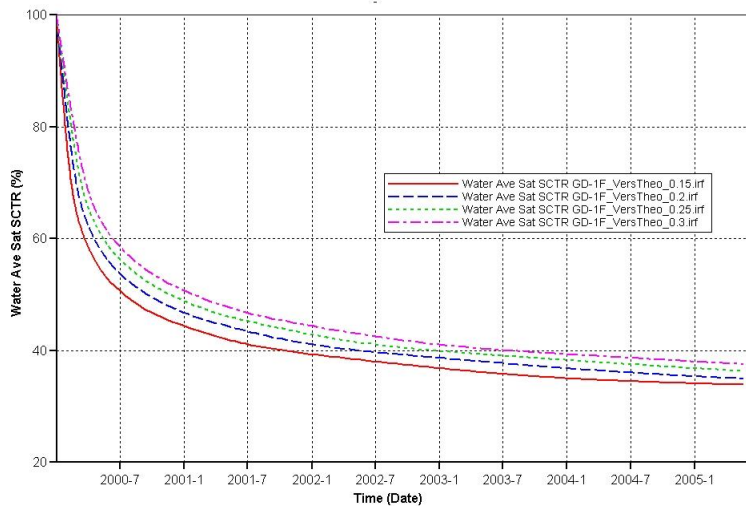


Figure 11: Effect of matrix porosity for model 1

The influence of the matrix porosity is not that dramatic as the influence of permeability. We can, however, also observe that during the beginning of the simulation the difference between the different porosity cases (i.e. 0.15, 0.2, 0.25, 0.3) is larger and then decreases in the end of the simulation. The final average water saturations range between 33.8 percent (0.15 matrix porosity case) and 37.5 percent (0.3 matrix porosity case). The porosity of the system might also be a factor in determining the potential of gravity drainage in certain reservoirs.

Depending on the boundary conditions different saturation profiles can develop.

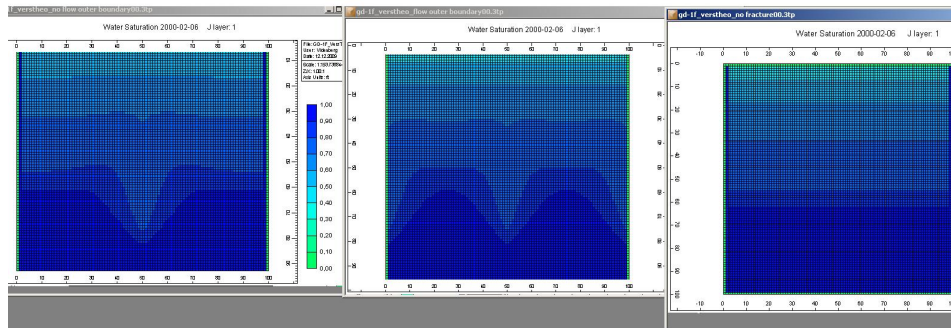


Figure 12: Saturation profiles for no-flow outer boundary (left), flow outer boundary (middle), and no fracture (right)

All three cases are for model 1. The left pictures shows the case, where the left and right model boundaries are no-flow boundaries, which is achieved by setting its permeabilities to zero. We can clearly see that the fracture causes a spike in the saturation profile. This just means that the region closer to the fracture is drained faster as compared to the region further away from the fracture. This implies that in the region close to the fracture there is some amount of fluid flow from the matrix region into the fracture region. This effect decreases with an increased distance away from the fracture. In the middle picture the left and right model boundaries are assumed as to be flow boundaries (permeability was left unchanged at 50 md). It produces spikes in the water saturation profile in the middle and at the left and right boundaries (because they are connected to a fracture) of the model. The right picture in the figure shows the case where there is no fracture in the middle of the model. We can see the vertical piston-like displacement fronts.

Plotting the average water saturation in percent over the entire simulation

duration is consistent with observations from before: There is no difference in the curves of the three cases (i.e. no fracture model, no-flow outer boundary, flow outer boundary). Therefore, no matter if we have a flow or no-flow outer boundary or even a model without a fracture there is no difference in the results. Left and right boundaries (i.e. vertical) do not seem to make an effect. As for subsequent results it will be shown that rather top and bottom boundaries (i.e. horizontal) influence gravity drainage.

Another simulation was performed to verify the effect of capillary pressure. From literature (see introduction section) it has been stated that gravity drainage is a battle between gravity and capillary. While gravitational forces try to expel the wetting phase downward, capillary pressure tries to hold back the wetting phase. Capillary pressure is closely related to the grain radii and sorting. Usually the smaller the radii of the pores the higher is the capillary pressure and the more resistance is provided against gravity drainage. In the simulation the default capillary pressure curve from Table 1 is used and other modified capillary curves. A very easy and neat way to modify the capillary pressure curves without making sacrifices on the curvature is by simply multiplying it with a prefactor. For this case I introduced a dimensionless variable that I called normalized capillary pressure defined below. In my simulations I changed the normalized capillary pressure between values of 0.5 and 1.5.

$$P_{cgw,normalized} = \frac{P_{cgw}}{P_{cgw,default}}$$

The expected behaviour was confirmed. A higher capillary pressure leads to lower recoveries and more oil is held back. Although for the first couple of months of the simulation the recovery is the same in all models, the curves start to deviate from about 3 months onward. Final average water saturations lie between 32.6 percent (case, where normalized capillary pressure is 0.5) and 37.3 percent (case for $P_{cgw,normalized} = 1.5$). This difference is quite significant and can determine the difference between economic and uneconomic case. Furthermore, the threshold capillary pressure leads to an effect known as capillary holdup. This means that at the bottom of the model there will be some wetting phase that cannot be produced and where the wetting phase saturation is one., no matter what we do. The same phenomenon was observed in our simulation. The capillary holdup is proportional to the capillary threshold pressure

(i.e. threshold capillary pressure can be “converted” to capillary holdup height). When the normalized capillary pressure was 0.5 then this zone had a height of 2 cells (which is equivalent to 2 feet), while this same height was 4 cells (equivalent to 4 feet) for the case when normalized capillary pressure was 1. The effect of the normalized capillary pressure on gravity drainage performance is presented below.

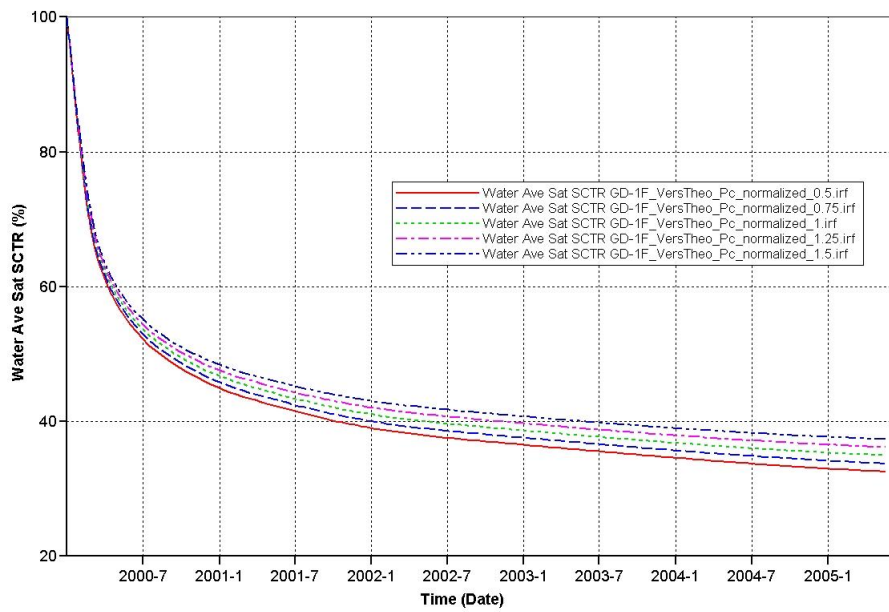


Figure 13: Effect of capillary pressure for model 1

Another simulation was run as to simulate cases where the wetting phase has different densities in order to observe the effect of wetting phase density. In this example the water densities were varied between $900 \frac{kg}{m^3}$ and $1050 \frac{kg}{m^3}$. It was shown that the effect is small but definitely not negligible. Final average water saturations were between 34.4 percent and 36.2 percent. The simulations showed that the higher the density of the wetting phase, which is to be drained, the higher is the ultimate recovery and the better does gravity drainage work. This indeed makes sense because gravity drainage depends on the gravity contrast between wetting phase and non-wetting phase. The higher the difference in densities between wetting phase and non-wetting phase the better. The weight of the hydrocarbons is a function of its density. This specific characteristic would seem to indicate that gravity drainage would be a preferred production method for heavy-oil reservoirs.

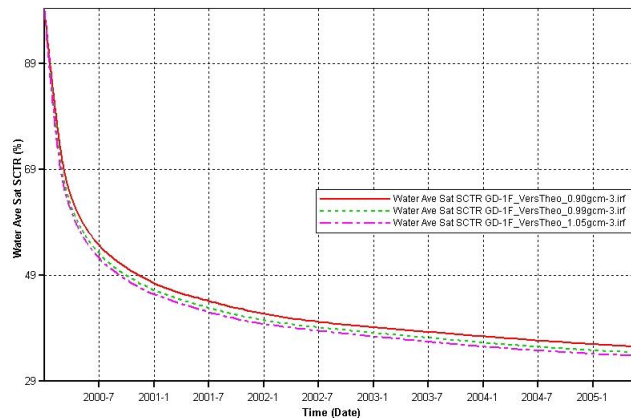


Figure 14: Effect of water density

The effect of gas gravity, which is the ratio of the gas density to the density of air, was also examined. In the trial simulation runs the numerical value of the gas gravity was changed between 0.6 and 1.0. The results also confirm the observation from above that an increased difference in gas and oil densities works advantageously in favour of gravity drainage and recovery curves. Therefore, the case where the gas gravity is lowest (at 0.6) is the best, while the case where the gas gravity is highest (at 1.0) is the worst in terms of oil production. What is interesting, however, to note is that the effect of gas density is negligibly

small and delivers curves that are almost identical. This makes sense because the density of gas is very low as compared to the density of the oil and therefore these minor changes do not affect the results. As to sum up, the main factor in those density considerations is the density of the oil, while the density of the gas plays a subordinate role.

I have also plotted the saturation distribution over depth and time for model 1. The results are presented in fig.38. On the x-axis the water saturation is plotted, while the height percentage* is plotted on the y-axis. Differently coloured lines represent saturation distributions for different times (in days). In the beginning the entire model has a constant water saturation of 1. Then the process of gas-oil gravity drainage starts modifying the curve. During this “transient” time the saturation over height (or, equivalently, depth) function approaches the drainage capillary pressure curve, which is represented in the plot as red hollow balls. It can also be inferred from the plot that for late times production will come mainly from shallower depths, where still a significant amount of the water exists untouched. Ideally, for an infinite time the saturation distribution will exactly match the drainage capillary pressure curve. The results for fig.38 have been known for a long time and are in agreement with Terwilliger et al. [1951].⁵

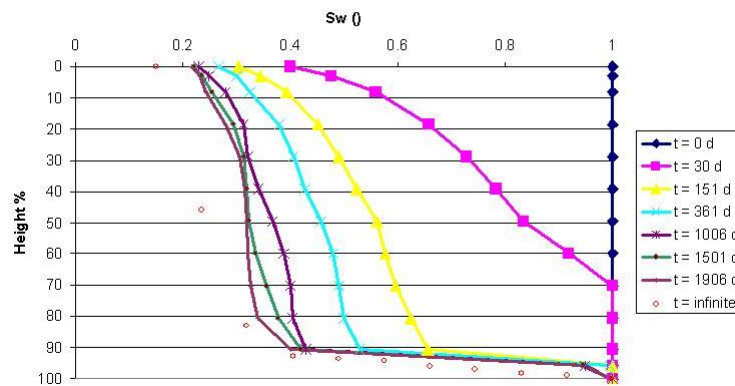


Figure 15: Change in saturation distribution with time for model 1

*Height percentage is a normalized height. For sake of simplicity the reader can assume y-axis of fig.38 to be height.

3.2 Effect of number and position of fractures

Fractures do not improve the gravity-drainage performance of model 1. It does not play any role how many fractures and where those fractures are, all recovery curves follow closely a very similar path. The reason for this is that the matrix itself is open to flow and all acting forces are mainly acting downward (i.e. gravitational direction). The oil sees no motivation to move in a vertical direction as to be displaced through the fracture.

Simulating model 2 has shown that the length and position of the fracture influences gravity-drainage performance. The most important factor is that the fracture is actively connected to the well and therefore establishes a high-permeability flow conduit through the low-permeability zone. Generally we would expect that an increased fracture length has a positive effect on the gravity-drainage performance. This effect was observed and can be confirmed. The longer the fracture length the faster is the wetting phase discharged from the payzone. The contact of a larger portion of oil with the high-permeability conduit displaces fluid more quickly. However, the interesting observation is that the effect can be significant if the fracture terminates within the low permeability bottomlayer or very close to it (e.g. 5 to 10 feet long fracture). If the fracture is longer and stretching further into the model (e.g. say 20 feet) then the effect between a 20 feet and a 50 feet or 98 feet long fracture is negligible small. For engineering purposes this means that as long as the fracture goes through the low-permeability zone and has a certain minimum size, then the length of fracture can be neglected and does not determine drainage success. During early simulation times the fracture length plays a minor role in speeding up the drainage. It must be noted, however, that at the end of the simulation this observation is reversed; models with fractures of shorter lengths have recovered slightly more oil (difference lies in the range of about 0.5 percent of average saturation).

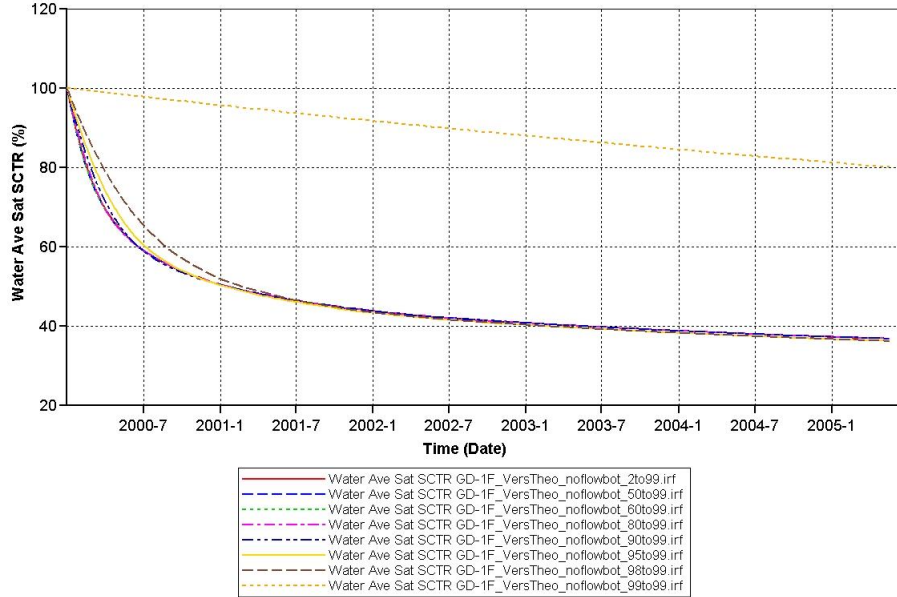


Figure 16: Effect of fracture length for model 2

The plot above shows the above mentioned details. On the y-axis the average water saturation in percent is displayed, while on the x-axis the date of simulation in year and month is shown.

3.3 Effect of fracture permeability

Changing the fracture permeability between 10^6 and 10^3 md in model 1 showed no influence on the recovery curves. This means that as long as flow occurs in the vertical direction through the matrix the effect of the fracture is not apparent. Only in the vicinity of the fracture the oil flows in a horizontal direction towards the fracture. It is interesting to observe that although the fracture permeability influences the near-fracture matrix region and increases the drainage-rates in those regions, the overall effect for the entire model is negligible small. Similar observations have been made in experimental setups by Zendehboudi et al. [2009],⁴⁵ who also confirmed that liquid communication exists only between the near-fracture vicinity matrix and the fracture, while further

away parts of the matrix are plainly unaffected by fracture presence. Fractures alone therefore do not necessarily influence gravity-drainage processes. Flow in model 1 is a vertical **piston-like 1D displacement process**. Zendehboudi et al. [2009]⁴⁵ have also found out from experimental studies that draining a model at low withdrawal rates makes the drainage similar to a piston-like displacement. The reader may also be referred to Hernandez [2002],⁴⁸ who found out that 3D flow in gravity drainage problems can be accurately represented by a 1D model. Furthermore, he mentions in his conclusions that **flow in lateral directions** in a gravity drainage problem is **negligible**. Graphically, the model can be imagined as a glass with water, whose bottom is open to flow. The water just experiences a gravitational force and has no motivation to flow to a fracture because the bottom is open anyhow.

Model 1 has such a geometrical configuration that the definition of an effective permeability would be with the help of a (parallel-series) weighted average permeability. However, calculation of such an average permeability gave a very high effective permeability. This result unfortunately contradicts the result from the recovery curves and the observation that gravity drainage of model 1 no way is affected by the presence of a fracture.

$$k_{eff} = \frac{\sum_{i=1}^n k_i w_i}{\sum_{i=1}^n w_i} = \frac{10^6 md \times 0.01 ft + 50 md \times 50 ft \times 2}{2 \times 50 ft + 0.01 ft} \approx 150 md$$

where w_i is the width of respective feature i . This result could lead to the conclusion that averaging permeabilities in naturally fractured reservoirs in order to obtain effective permeabilities could be problematic. Correa et al. [1996]⁴⁹ have also pointed out that averaging permeability in gravity drainage studies in layered porous media may be dubious.

The figure presented here shows the influence of modified fracture permeabilities on the drainage performance. On the y-axis we can see the average water saturation in percent, while on the x-axis the date of simulation is displayed. All displayed curves follow the same path and we cannot observe any difference. Just if we zoom into the results very strongly we can observe a very, very small difference in the hundredths digit. As for everyday engineering purposes this minor difference is insignificant. The plot also tells us that the drainage has most effect in the first couple of months after the start of the simulation. For later times that change in average water saturation becomes smaller and

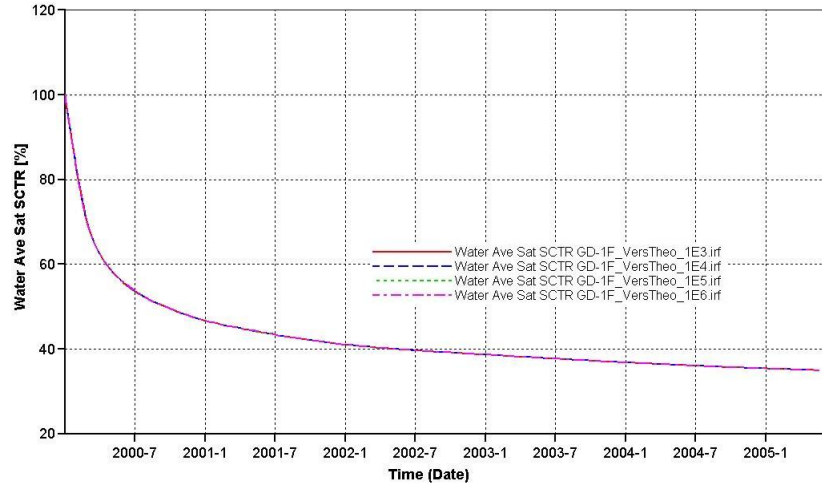


Figure 17: Effect of fracture permeability for model 1

smaller. The final water saturation at the end of simulation is approximately 35 percent. Gravity drainage is a pretty efficient recovery method, but it works slow as compared to other recovery methods.

As seen above when the matrix blocks are open to flow, then the fracture permeability does **not** play a very significant role. Even if we simulated a 1 md matrix then the fracture does not have any influence. Scaling the system to an effective permeability based on harmonic averaging (i.e. taking into account fracture widths) does not yield satisfying results. However, something completely different is observed when we simulate model 2. Here the fracture permeability plays a significant role, as it increases the speed of the drainage process. Basically, it can be said that the higher the fracture permeability, the better is the drainage. The difference in average payzone water (i.e. wetting phase) saturation between the individual cases can be significant. At a fracture permeability of about 1000 md the curve decreases in an almost linear fashion, while in the other cases the curve decreases in an exponential fashion. The final recovery is the same for all fracture permeabilities and lies at about 36 to 37 percent. After about three years all curves (with exception of the 1000 md curve)

follow the same path. The existence of fractures alone does not increase the recovery rate itself, but only increases the drainage speed. The result obtained in this simulation can be easily explained. High amounts of hydrocarbons try to leave the model through the fracture, but if the fracture permeability is too low the drainage is slow. Graphically it can be visualized by a train station and large amounts of people trying to leave a city. The higher the train frequency (representing permeability) the faster will those people (representing the oil) be discharged. Results are plotted below. On the x-axis we have the date of simulation, while on the y-axis we have the average water saturation in percent and the water volume at reservoir conditions in cubic feet.

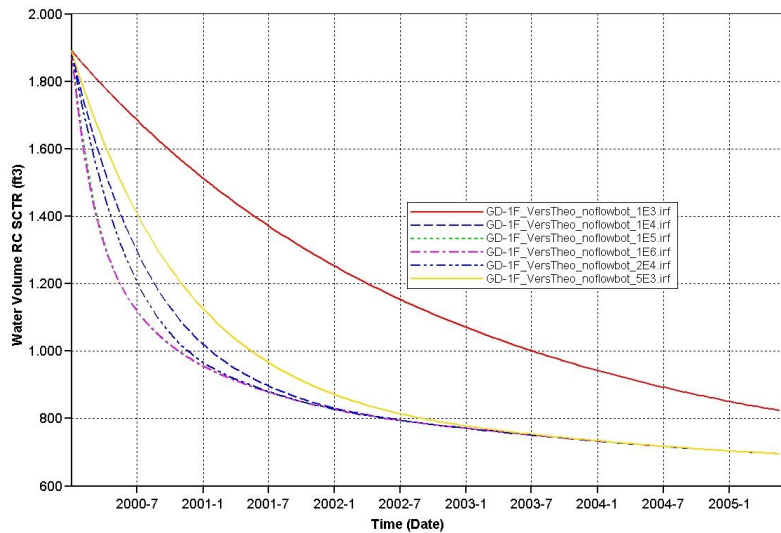


Figure 18: Effect of fracture permeability for model 2 (on water volume)

The fracture permeabilities were then modified with the simulation of model 3 (two layers reservoir and fracture). In the model the upper layer matrix permeability was 50 md, while the bottom layer matrix permeability was lower at 10 md. The simulation shows that the fracture permeability plays a small role on the early time recovery, as a high fracture permeability has better fluid transport potential. The matrix block drains faster in the beginning of the simulation, however for later times the recovery curves follow the same path. It is interesting to note, that the curves fall together approximately one year

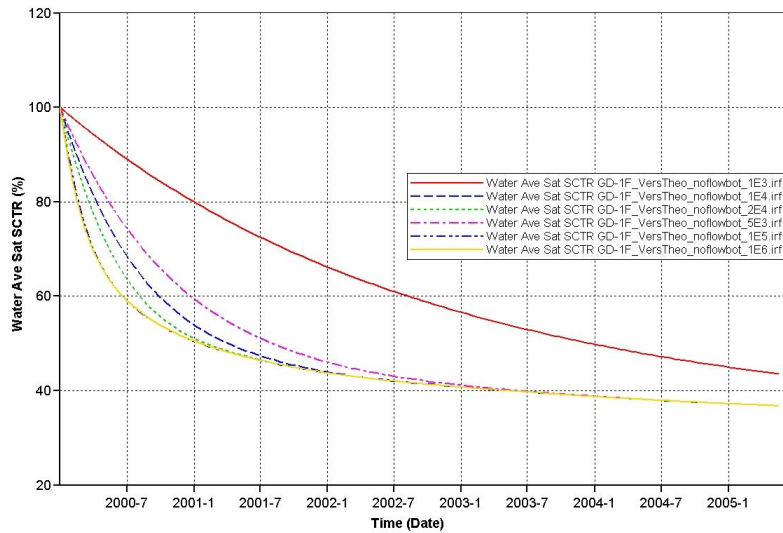


Figure 19: Effect of fracture permeability for model 2

and one month (i.e. January 2001) after the simulation has started. This would imply that the existence of fractures only enhances performance on the short term. As for engineering purposes it seems as if the company has to make the decision whether that early time extra gain would justify increased operational costs of gravity-drainage processes.

3.4 Effect of fracture capillary pressure

Several simulations were performed to see the influence of fracture capillary pressure. Experimental results of fracture capillary pressure curves are very sheldom because of the difficult experimental setup. Here, as to make life more simple, capillary pressure within the fracture was related to the pore radii (i.e. half of the fracture aperture in this case), interfacial tension between water and gas and contact angle. The formula is presented below

$$P_{cf} = \frac{2\sigma \cos \theta}{r_f}$$

where σ is the interfacial tension for water-gas system, θ is the contact angle between water and gas, and r is the fracture radius. As the fracture aperture (and therefore fracture radius) is constant along the vertical axis, this should automatically lead to a constant capillary pressure in the fracture. The numerical values for the parameters of interfacial tension ($\sigma_{wg} = 50^{\text{dyne/cm}}$) and contact angle ($\theta_{wg} = 0^\circ$) were taken from Graves [2008].⁴⁷ Those parameters lead to a constant capillary pressure as function of water saturation.

Changing the fracture capillary pressure between values of 0.01psi and 0.05psi for model 1 did not influence the results. This is evident because previous simulation on model 1 have shown that the fracture does not influence free-fall gravity drainage. Therefore it would be absolutely inconsistent if fracture capillary pressure had an effect on gravity drainage for this model.

The same simulation was also applied on model 2 with the same results. No matter how much the fracture capillary pressure was changed, the recovery curves over time looked the same. The plot of average water saturation over time is presented below for model 2. This would lead to the notion that the fracture capillary pressure is a force in gravity drainage processes that can be neglected. **The choice of fracture capillary pressure does not significantly affect drainage rates.** (Note: If we strongly zoom into the average water saturation versus time plot we can see that the case of 0.05psi - fracture capillary pressure drains more wetting phase from the matrix than the case of lower fracture capillary pressures. This could lead to the assumption that the higher the fracture capillary pressure, the better is the oil drained from the matrix. However, the difference is so small that it cannot be seen with the eye and can be safely disregarded for engineering purposes).

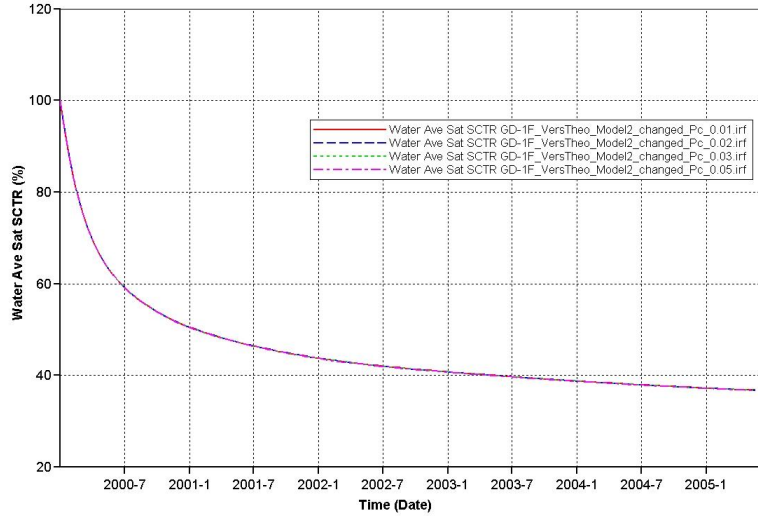


Figure 20: Effect of fracture capillary pressure on model 2

3.5 Effect of relative permeability

During the course of work some simulations have been made as to get a qualitative understanding of the effect of relative permeabilities of the gas and the water phases. The Brooks-Corey relative permeability model (see section 3.2) was employed to compute relative permeability curves, as well as the matrix capillary pressure curve. Necessary parameters are immobile (or residual) water saturation, threshold capillary pressure, Brooks-Corey (abbrev. BC) parameters for water and gas, as well as water and gas endpoint relative permeability values. The gas residual saturation was assumed to be zero, which is a valid assumption because gas is the non-wetting phase. The following equations were used

$$k_{rw} = k_{rw}^* \left(\frac{S_w}{1 - S_{wr}} \right)^{\lambda_w} = k_{rw}^* (S_e)^{\lambda_w}$$

$$k_{rg} = k_{rg}^* \left(\frac{1 - S_g}{1 - S_{wr}} \right)^{\lambda_g} = k_{rg}^* (1 - S_e)^{\lambda_g}$$

with a fixed residual water saturation S_{wr} of 0.15. Here S_e is a normalized

saturation known as effective saturation.

First the endpoint gas and water relative permeability values were kept constant at 1, while the gas Brooks-Corey parameter λ_g was modified for values between 2 and 4. I on purpose decoupled the exponents λ_w and λ_g from the exponent I used in the capillary pressure function. I did this to remove the rigorous restriction of exponent relationship in the original Brooks-Corey model. A plot of average water saturation versus simulation time is presented below. It can be seen that a higher gas BC parameter delivers better recoveries than lower gas BC parameters. The final water saturations lie between 34 and 35 percent. Although a slight difference in recovery curves can be seen, the difference is very small and almost negligible. If we plot the gas relative permeability and the capillary pressure both as functions of gas BC parameter, we can see the effect and get a clue why a high λ_g is advantageous. A high gas BC parameter decreases non-endpoint gas relative permeability values, when compared to lower gas BC parameters. This effect has to do little with gas-oil gravity drainage. What is even more important is the effect of λ_g on the gas-oil capillary pressure curve. Higher values of the gas BC parameter decrease the capillary pressure. The capillary pressure approaches to an almost constant value with ever increasing λ_g . This is related to an uniform sorting of grain sizes. I believe that the (small) difference in average water saturation over time is mainly due to the effect of gas BC parameter on the capillary pressure. A similar finding is presented in Li and Horne [2003],¹³ who say that “(...) average residual oil saturation increases with the decrease in pore size distribution index” and that “oil recovery by gravity drainage may increase with the pore size distribution index”. Notice also that the size of the capillary holdup region is not affected by the gas BC parameter (it only affects curvature). However, the plot shows that **gas relative permeability** (or non-wetting phase relative permeability) **does not influence gravity drainage** performance significantly. Therefore, the laboratory determination of the **non-wetting phase relative permeability is non a critical factor**. Nevertheless, carelessness is not recommended.

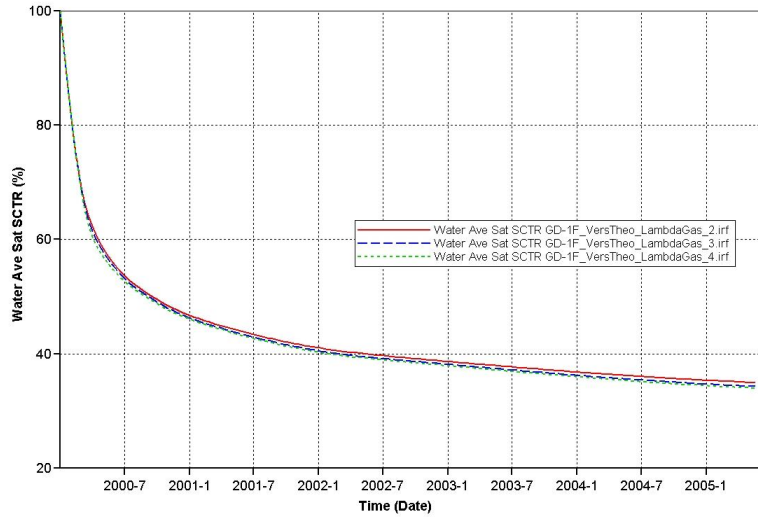


Figure 21: Effect of non-wetting phase relative permeability curvature on GOGD

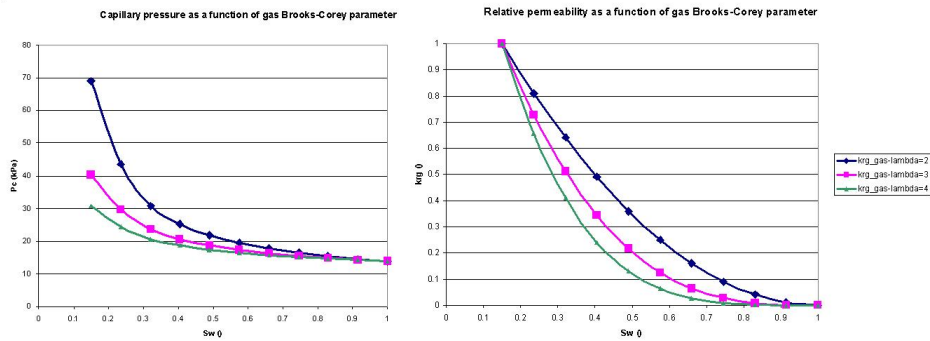


Figure 22: Influence of gas Brooks-Corey exponent on relative permeability and capillary pressure

Also, some simulations with changed water BC parameters (between $\lambda_w = 2$ and $\lambda_w = 4$) were performed, while the other parameters were kept constant (e.g. $S_{wr} = 0.15$, $k_{rw}^* = 1$, $k_{rg}^* = 1$. $P_{c,thr} = 2 \text{ psi}$, etc.). A plot of gravity drainage recovery curves for different water BC parameters is presented below. It can be clearly seen that a low λ_w significantly affects the final recovery. The lower the λ_w the more efficient is the gravity drainage. For a water BC parameter of 2 the final average water saturation is 23 percent, while it is about 35 percent for a water BC parameter of 4. While in the previous case a high gas BC parameter improves drainage performance because it modifies the capillary pressure curve and therefore increase the amount of recoverable fluid, the reason why a decreased water BC parameter is a different. Decreasing the λ_w affects the water relative permeability curve as it increases the non-endpoint values (i.e. all values except relative permeability values at residual water saturation and initial water saturation). This then increases the wetting-phase effective permeability (i.e. product of absolute permeability and wetting-phase relative permeability), which is a major governing factor for vertical gravity-drainage. From the formulas above we can also see that water BC parameter does not affect the capillary pressure curve. As a conclusion, it must be said that the water relative permeability (i.e. **wetting-phase relative permeability**) is a **major factor** on the success of gravity drainage. The oil relative permeability has also been confirmed to be a key factor in gravity drainage processes in a study by Hagoort [1980].⁸ Therefore, I recommend an accurate laboratory measurement of wetting-phase relative permeabilities.

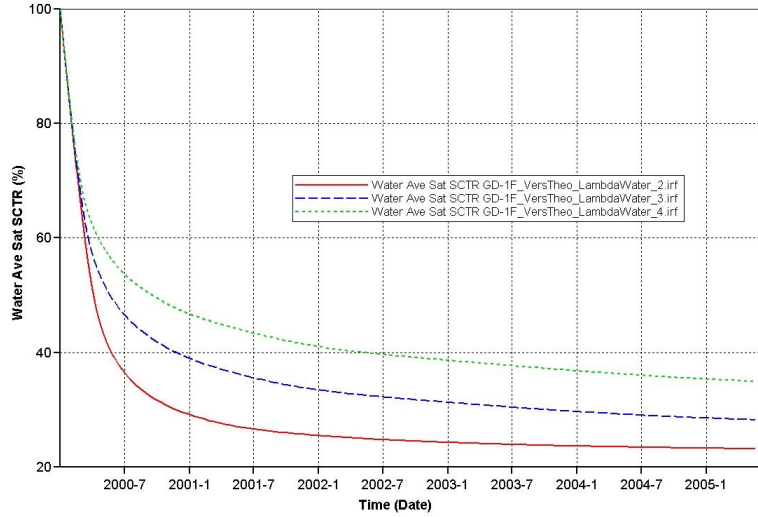


Figure 23: Effect of wetting phase relative permeability on GOGD

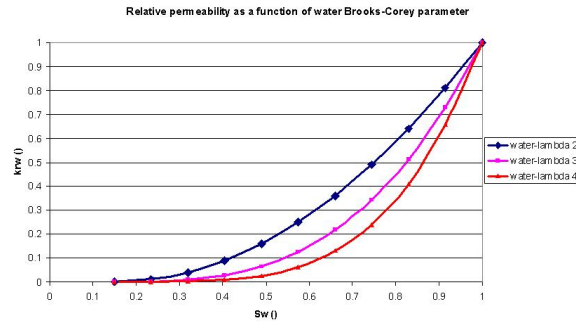


Figure 24: Influence of water Brooks-Corey parameter on relative permeability

3.6 Effect of bottomlayer matrix permeability

Previous subsections have indicated that fractures do not influence gravity-drainage performance for a one layer model (model 1). This was explained by the openness of the matrix and the lack of horizontal flow. The vicinity of the

fracture experiences flow directed towards the fracture, however, on an overall scale this effect can be neglected.

If the bottomlayer is sealed or impermeable (model 2), then the fracture has an effect only if it goes through the non-permeable layer; thus establishing a pathway for the oil to escape the model. This indicates that the boundary conditions play an important role for gravity-drainage.

Now the question arised whether gravity-drainage in a layered model with a fracture would be different to the same layered model but without a fracture. For analyzing purposes model 3 was set up. The upper layer matrix permeability was kept at 50 md, while the lower bottomlayer's permeability was changed between 5 and 25 md. The observations show the following: Fractures do have an influence on the recovery curves when the model is layered and has different permeabilities. The only prerequisite is that the bottomlayer has a very small permeability as compared to the upper layer. The larger those permeability contrasts are the bigger is the effect of the fracture. In the case where zone B (i.e. lower layer) has a permeability of 25 md and zone A (i.e. upper layer) has a permeability of 50 md, there is no clear difference in recovery curves between the fractured and the unfractured model 3.

However, if we change zone B to 10 md then there exists a small difference in average water saturation in the beginning of the simulation. It is clear that the fracture quicklier drains the water from the model. The difference in fractured and unfractured model 3 is even bigger if we decrease the permeability of zone B to 5 md. However, in both cases the differences in average water saturation decrease over time. There is a specific time, when the recovery curves between fractured and unfractured model fall together. In the zone B 10 md case this specific time is about 1.6 years after simulation start (i.e. July 2001), while it is about 3.1 years after simulation start (i.e. January 2003) in the zone B 5 md case.

To sum up, the lower the permeability of zone B the bigger is the influence of the fractures. Moreover, the lower the permeability of zone B the later does the characteristic time, where recovery curves are the same for the fractured and the unfractured model, occur. This would lead to the conclusion that gravity-drainage in fractured reservoirs would be advised for heterogeneous and layered reservoirs, that have several low-permeability layers.

Fractured models therefore have an advantage over unfractured models on gravity drainage performance just for **layered models** that have some **low-**

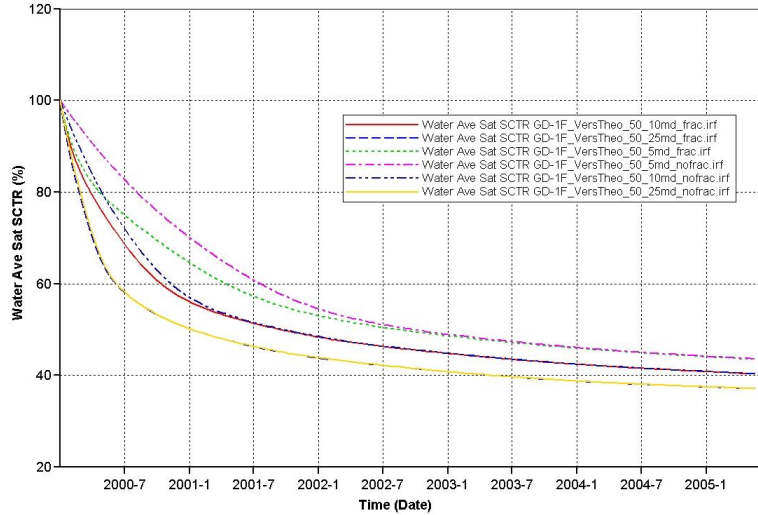


Figure 25: Effect of bottomlayer permeability on model 3

permeability layers. These low-permeability layers are believed to enhance lateral flow and to direct wetting phase towards the fracture. Experimental tests from Zendehboudi et al.[2008]⁴⁶ have come to a similar conclusion. They found out that the effect of fractures on the liquid recovery is more pronounced in systems of low-permeability matrix. If the matrix on the other hand has quite a high permeability, then the presence of fractures is not significant for the recovery.

A possibility could be to evaluate the permeability ratio between upper and lower layer and thereby try to make a relationship between the effects of fractures. There should a minimum permeability ratio, when the effect of fractures starts to be significant. Further research is needed concerning this point.

During the course of work the question arised whether the recovery curves are affected by the order of occurrence of different permeability layers in vertical direction. My expectation was that the different order of layers would affect the gravity drainage performance and the recovery curves. I think it would be appropriate to assume that in cases where the higher permeable layers are at the bottom while the lower permeable layers are at the top, the average saturation over time would decrease faster than in an exactly opposite case (i.e. higher permeable layer at the top and lower permeable layer in the bottom). However,

I assumed that for later times of the simulation both cases would lead to the same final recovery. So much about my expectation.

I made several simulations where I changed the order of layers as to observe if there would be any different gravity drainage behaviour. The original combination of 50 md and other cases with 5, 10 and 25md were simulated. The result is presented below.

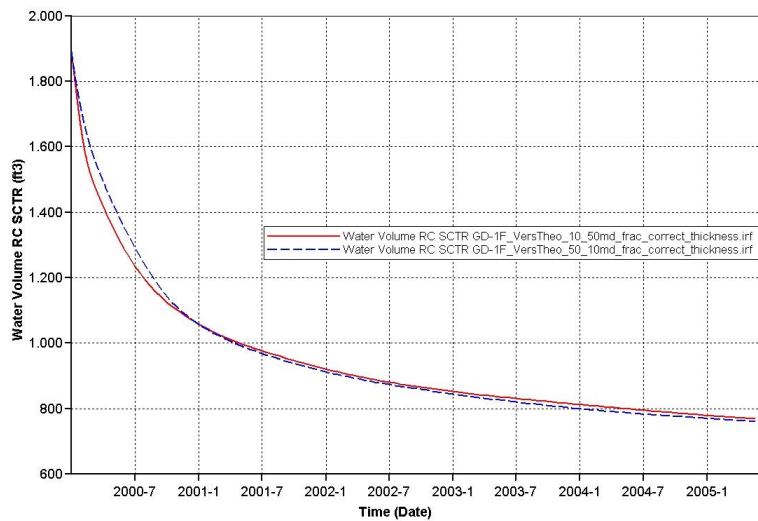


Figure 26: Effect of layer sequence on model 3

On the y-axis the volume of wetting phase (i.e. water) in reservoir condition and in cubic feet is shown versus the date of simulation. The result is for the case of 10 and 50 md. It can be seen that the recovery curves are different based on the vertical position of the layer. As expected the case where the higher permeable layer is at the bottom drains faster for early times. This is shown in the red line in the figure (10_50md in the legend). However, for later times this trend is changed and the case, where the higher permeable layer is in the top (dashed blue line) is slightly more efficient in terms of recovered fluid. This is a surprising result and contradicts my expectation that in the end of the simulation both cases will lead to the same final recovery.

I obtained similar results when I simulated the 5 and 50 md, as well as the 25 and 50 md models. The main deviating aspects are that the early-time difference

is smaller for smaller matrix permeability quotients (e.g. could be defined as the ratio between the high-perm and the low-perm layer) and the difference in the late time also decreases with this decreasing ratio. I want also to mention that there is a specific time, when the recovered value becomes the same for both cases. The appearance of this specific time is delayed for cases when the permeability contrast between those layers is large (and similarly vanishes if the permeability ratio is very small).

As to sum up, the higher the permeability contrast and the permeability ratio between the layers the greater is the difference in recovery curves. Also it seems that the gravity drainage recovery curves for model 3 are a function of the sequence of layers (i.e. recovery curves of a layer sequence A-B will not necessarily be the same as sequence B-A). As a consequence **the success of gravity drainage is also related to the sequence of layers**. The reader may also be referred to Correa et al. [1996],⁴⁹ who studied gravity drainage in layered homogeneous models and found out that “the permeability order affects gravity drainage performance in layered systems”. Further research is recommended concerning this point and its confirmation.

3.7 Cooke model simulation results

After having set up the Cooke model, I performed some simulations that were similar to those applied on models 1 to 3.

At first I wanted to gain some insights on the effect of fractures on a homogeneous model. I assumed that all the eight layers of the modified Cooke model had the same properties in terms of permeability, porosity, Brooks-Corey parameters etc. For the permeability I assumed a value of $50md$. This basically leads to a quadratic homogeneous model with 52 vertical fractures. I compared this special type of the Cooke model with a model that has the same properties but no fractures. Applying a free-fall gravity drainage experiment showed that fractures do in fact have an influence on gravity drainage. Fractures do not increase the final recovery, however, they **increase the drainage speed**. This increase in drainage speed can be a crucial aspect in terms of economic considerations. There is a time, however, where both recovery curves (fractured homogeneous and unfractured homogeneous model) coincide. I prefer to call this time the characteristic time. I believe that it can have significance for economic evaluation and prediction purposes. It could also give an idea whether fracturing could be advantageous to produce the field by GOGD. In the $50md$ matrix permeability case this time is about two and a half years after simulation start.

I performed the same simulation with a decreased matrix permeability of $10md$. In this case even after 5 years of simulation this characteristic time was not reached. The gravity drainage recovery curves are almost parallel. This leads to the conclusion that **fractures are especially advantageous in case of a low permeability matrix**. Fractures are not that useful in higher permeable formations. The smaller the matrix permeability the more pronounced is the influence of the fractures.

In the figure 27 we can see the average wetting-phase saturation on the y-axis and the simulation time on the x-axis. The blue discontinuous line represents the unfractured homogeneous case with a matrix permeability of $10md$, while the red continuous line represents a homogeneous fractured case with the same matrix permeability. Both lines are almost parallel, and time when both curves become indistinguishable is not reached. The other two stippled lines (Fig. 27) represent an unfractured homogeneous (i.e. pink line) and a fractured homogeneous (i.e. green line) case with a matrix permeability of $50md$. After a simulation time of

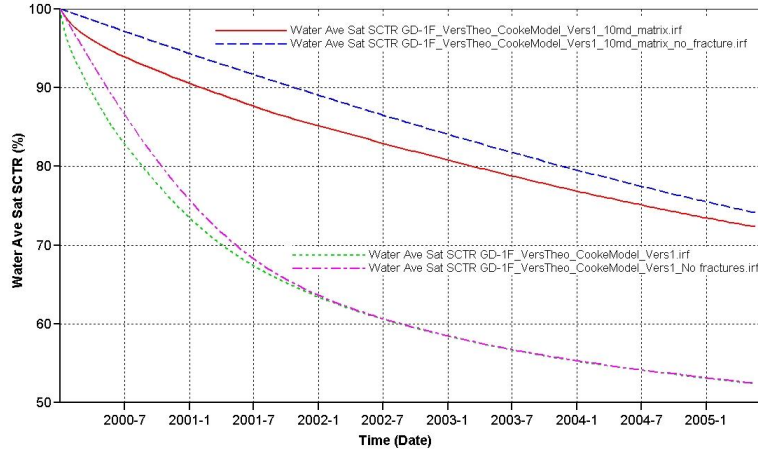


Figure 27: Influence of matrix permeability on recovery in homogeneous Cooke model

about two and a half years these curves start to overlap.

I then made several other simulations to confirm observations made from models 1 to 3. However, Cooke model behaves differently to models 1 to 3. While it was important for the fracture to be connected to the well in the simple model this is not true for the Cooke model. The existence of numerous vertical fractures seems to increase the effective vertical permeability. For the Cooke model without fractures the effective vertical permeability is 0.2 md^\dagger . As a result drainage velocity is increased. Also there seems to be a “threshold number” for vertical fractures: If the fracture number is smaller than this number, then the fractures do not increase effective vertical permeability and the model can be simplified by only taking into account the fractures that are directly connected to the well. If this “threshold number”, however, is surpassed then even the fractures that are not connected to the well play a certain role and increase effective vertical permeability.

The plot 53 presents water saturation as a function of simulation time. It can be seen that the fractures, which are connected to the top and bottom

[†]The horizontal permeability for Cooke model was 100 md and 1 md for dolomite and shale layers respectively. The vertical permeability was set to one tenth of that value

boundaries, are the first to be affected by gravity drainage. This is intuitive due to the large fracture permeability. Gas first enters the fractures that are directly connected to the (imagined) horizontal well at the top of the model and is transported downward (similarly, the fractures that are connected to the horizontal well at the bottom of the model are the first to be depleted of the wetting phases). The gas in the vertical fractures builds up a gravitational force which is resisted by the capillary forces in the matrix blocks. In tiny models, gas mainly enters the higher permeability dolomite layers, while gas entrance rates into the lower permeable shale layers are much smaller (Fig. 28 and Fig. 29). Gas invades the matrix blocks from top and creates an almost logarithmic non-wetting phase saturation profile in the matrix block. Whenever, the gas reaches a nearby vertical fracture, this fracture almost immediately is drained and becomes gas-filled. In addition, the existence of vertical fractures close to that already gas-filled fracture “attracts” the gas and these regions have increasingly lower wetting phase saturations. To sum up, the existence of vertical fractures leads to gas infiltration of higher-permeable layers while the low permeable formations are bypassed. Different layers drain at different speeds. I prefer to call this observation **gas-channeling**.

If I compare the Cooke model with fractures and a model that has the same absolute and relative permeabilities and porosity but **no** fractures then the difference becomes evident. While in the regular Cooke model the fractures help the gas in by-passing less permeable layers, which are thus less attractive for production, this is not possible in an unfractured case. The unfractured case would simply be a cake layer model of different permeability layers. Here the saturation and drainage displacement profiles are horizontal (i.e. perpendicular to gravitational pull). Therefore no by-passing of the lower permeable layers is possible. This drainage speed is proportional to the permeability and therefore very low. These layers act as obstacles to the GOGD process.

While the final recovery is only about 8 % for the unfractured case, it is about 35 % for the fractured case (Fig.30). At the end of the simulation, after 5.5 years, the saturations in blocks with the same depth are almost the same. The influence of fractures is dramatic.

The **effect of gas density** on recovery from the Cooke model has also been studied. The results are in agreement with results from previous studies as they suggest that a large density contrast between wetting and non-wetting phases

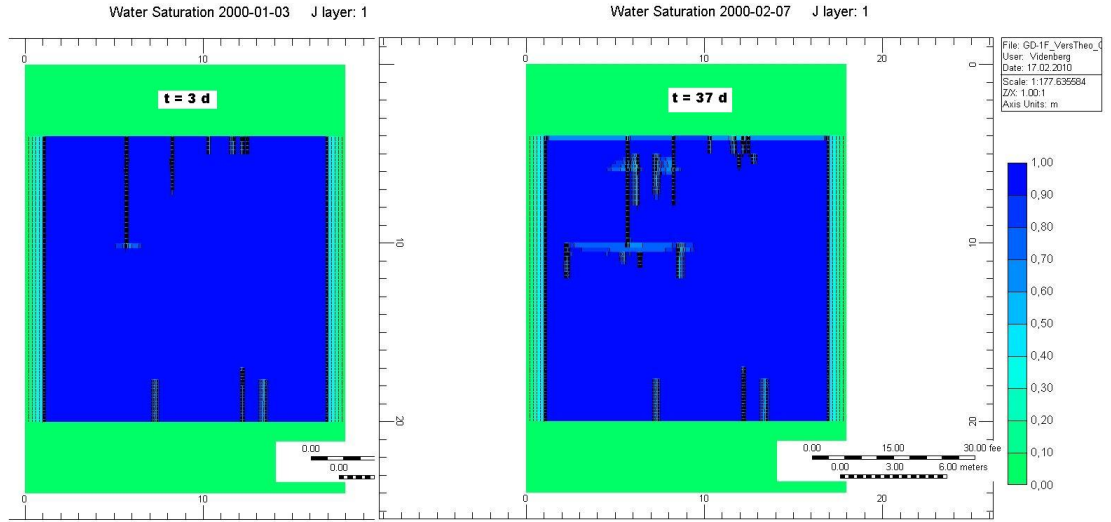


Figure 28: Water saturation for Cooke model

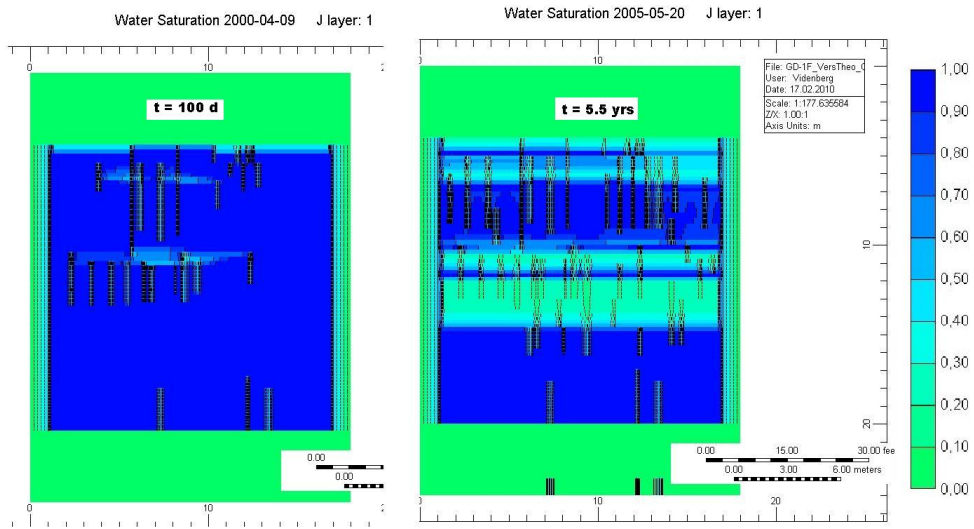


Figure 29: Water saturation for Cooke model

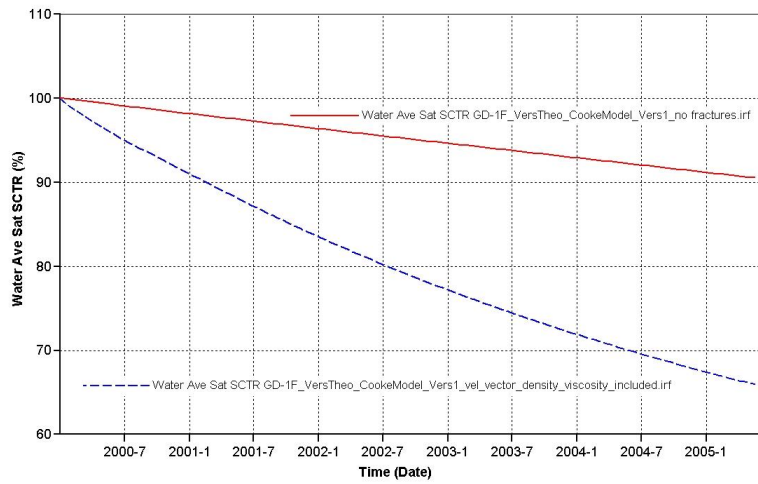


Figure 30: Effect of fractures on Cooke model recovery. The blue discontinuous line represents the Cooke model with the fractures, while the red continuous line represents the same model but with no fractures. One can clearly see the dramatic influence of fractures on gas-oil gravity drainage.

has an advantageous effect on recovery (e.g., Luan [1994]⁵¹). In GOGD formulations gravity drainage is supported by a gravity term ($\Delta\rho g = (\rho_o - \rho_g)g$), which is related to absolute density difference between oil and gas. The smaller the gas density, the larger is the percentage of recovered oil. Nevertheless my results indicate that gas density is not a very critical factor because its numerical value is much smaller than the oil density. Gas density differences are so small that the gas density can be assumed negligible. Table 7 shows that the difference in GOGD recovery after 5 years is less than half of a percent.

	$SG_{gas} = 0.8$	0.9	1.0	1.1	1.2
after 30 days	1.11%	1.1%	1.1%	1.1%	1.1%
after 151 days	4.3%	4.28%	4.26%	4.24%	4.23%
after 361 days	8.92%	8.88%	8.84%	8.80%	8.77%
after 3 years	22.81%	22.72%	22.63%	22.54%	22.45%
after 5 years	32.61%	32.5%	32.39%	32.28%	32.16%

Table 7: Recovered oil for different specific gas gravities in Cooke model

Table 7 presented the recoveries for different gas densities and showed that gas density is not an important factor simply because of the low gas densities. The density of the wetting phase (i.e. oil), however, is a key factor that can dramatically influence success of gas-oil gravity drainage. The data in table 8 confirms the known fact, that recovery increases with a larger density difference between oil and gas phases. The ideal candidate oil for GOGD would be an oil that has a large density, while also having a small viscosity.

	$\rho_o = 750 \frac{kg}{m^3}$	800	850	900
after 30 days	0.89%	0.96%	1.03%	1.09%
after 151 days	3.36%	3.63%	3.9%	4.30%
after 361 days	7.01%	7.56%	8.11%	8.92%
after 3 years	17.89%	19.38%	20.83%	22.81%
after 5 years	26.19%	28.2%	30.09%	32.61%

Table 8: Recovered oil for different oil densities in Cooke model

From previous studies and already performed simulations of models 1 to 3 it is known that **oil viscosity** belongs to the major factors of gravity drainage processes. This is confirmed in the results of the sensitivity analysis that I performed on the Cooke model. The results clearly show that increased oil viscosities have a very negative effect on the oil recovery and greatly slow down the

GOGD. Artificial methods of decreasing the oil viscosity therefore are justifiable (e.g. steam-assisted gravity drainage). An accurate laboratory determination of oil viscosities is vital for GOGD and strongly recommended. Table 9 presents the recovered oil in percent for different oil viscosities and simulation times.

	$\mu_o = 1 \text{ cp}$	1.5 cp	2.0 cp	2.5 cp
after 30 days	1.11%	0.79%	0.62%	0.52%
after 151 days	4.30%	3.02%	2.37%	1.95%
after 361 days	8.92%	6.31%	4.97%	4.14%
after 3 years	22.81%	16.65%	13.09%	10.79%
after 5 years	32.61%	24.92%	20.11%	16.84%

Table 9: Recovered oil for different oil viscosities in Cooke model

I also made several simulations to examine the effect of fracture permeability on the recovery in GOGD processes. At first I changed the **fracture permeability** for values between $10^5 md$ and $10^7 md$. The larger the fracture permeability the faster the model is drained. For a fracture permeability of $10^5 md$ the recovery after 5 years was about 32.5%, while higher fracture permeabilities (i.e. $500000 md$; $10^6 md$; $10^7 md$) had a somehow similar recovery of about 33.9%. The results indicate that when fracture permeability reaches a certain value, increased permeabilities do no influence recovery. Fracture permeability is only a factor when the permeability contrast between matrix and fracture is small.

Based on the intrinsic formula from section XX, I also modified **fracture capillary pressure**. I made several simulations with a P_{cf} of $0.2 kPa$ to $1 kPa$. Assuming that the fracture width is constant the capillary pressure function is constant over saturation. The results indicate that ultimate recovery increases with **fracture capillary pressure** (for a $P_{cf} = 0 kPa$ the ultimate recovery was 34.07%, while recovery was 34.77% for a $P_{cf} = 1 kPa$). The reason for this lies in the mathematical formulation of fluid transfer between fracture and matrix[‡] and Saidi and Sakthikumar [1993]¹⁰ have also confirmed this result.

Varying the pore size distribution index in the Brooks-Corey equations between of 2 to 3 in the dolomite layers also influences the recovery. The difference observed was about 1.8%. Generally it can be said that the higher the pore size

[‡]The capillary term of the transfer function is based on the absolute difference in capillary pressure between fracture and matrix. While matrix capillary pressure opposes GOGD, fracture capillary pressure assists in GOGD by reducing this absolute capillary pressure term.

distribution index the higher the recovery. The reason for this is both the increase of relative permeability and the simultaneous decrease in the capillary pressure curve. This means that the effective permeability of the wetting phase is increased and the amount of recoverable oil is increased. High pore size distribution indices refer to a reservoir that has well sorted rock particles. These results are in agreement with Li and Horne,¹³ who state that “oil recovery by gravity drainage may increase with the pore size distribution index”. The figures below present the influence of pore size distributions on recovery, relative permeability and capillary pressure.

Later, I also changed the pore size distribution index between values of 2 and 3 for the shale layers. The results also confirm that increased pore size distribution indices have a positive albeit small effect on recovery of GOGD. Recovery was 34% for $\eta = 3$ and 33.42% for $\eta = 2$. The difference is about 0.58% and much smaller than in the dolomite case. This result indicates that the determination of the pore size distribution index is important for the higher permeable (dolomite) layers. I expected this outcome, because from previous simulations I had observed that GOGD process was especially dependent on the higher permeable layer and its wetting phase saturations. Saturations changes are negligible in the shale layers and shale relative permeabilities values do not change significantly during the simulation.

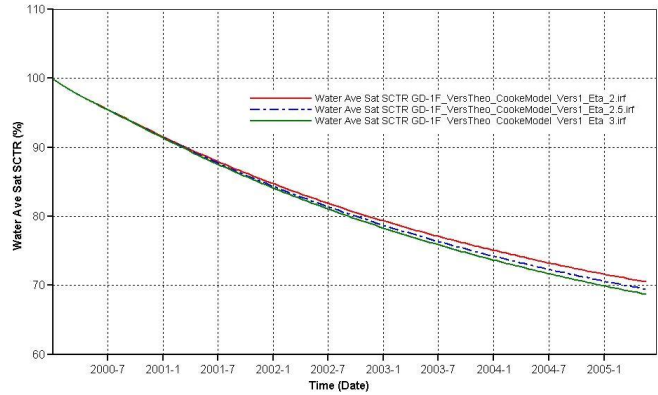


Figure 31: Influence of pore size distribution index in dolomite on recovery from Cooke model

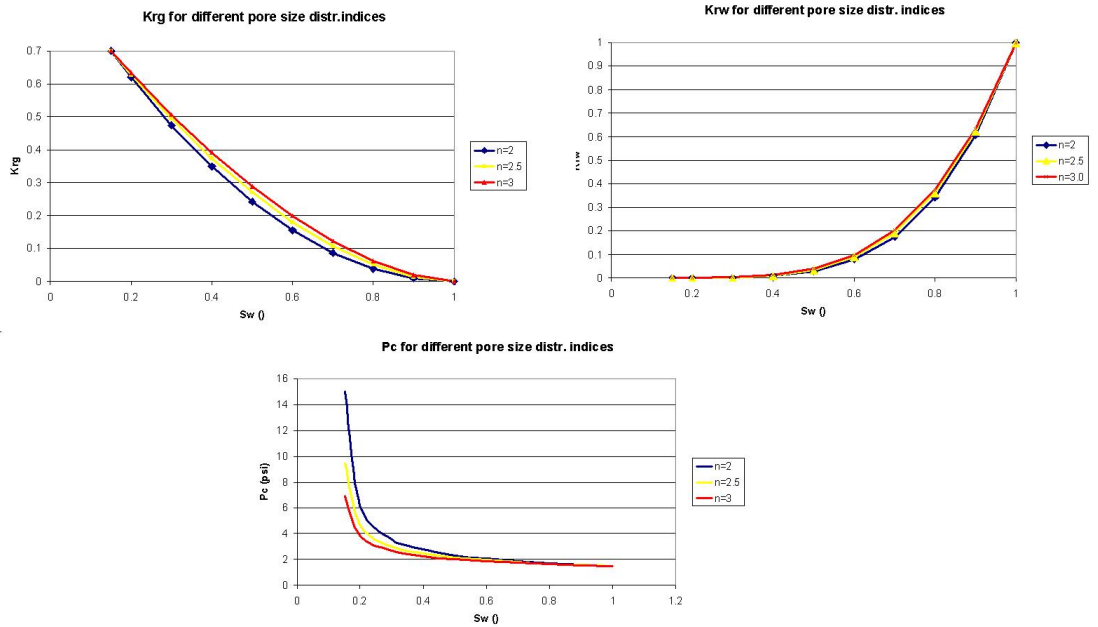


Figure 32: Influence of dolomite pore size distribution index on K_{rg} (top left), on K_{rw} (top right) and P_c (bottom)

The capillary pressure entry can be translated to a threshold columns height. If the gas in the fracture cannot build up enough gravitational forces to overcome this threshold capillary resistance, then the layer will not experience GOGD and will be left behind with its original wetting phase saturation. Importantly, calculations with the simple threshold formula that translates threshold capillary pressure to column block height (using gravitational acceleration and density difference of fluids) did not give the exact height of the capillary hold-up zone as the increase of threshold capillary pressure strongly decreases recovery. To analyse this, threshold capillary pressures were modified between $1psi$ (red continuous line) and $3psi$ (pink discontinuous line) (Fig.33). Assuming that in the ideal case the gas saturation in the Cooke model would be as large as possible, it can be said that small threshold pressures achieve this. An interesting observation I could make is that the modification of the threshold capillary pressure in the dolomite layers also has an influence on the recovery from the low permeability layers.

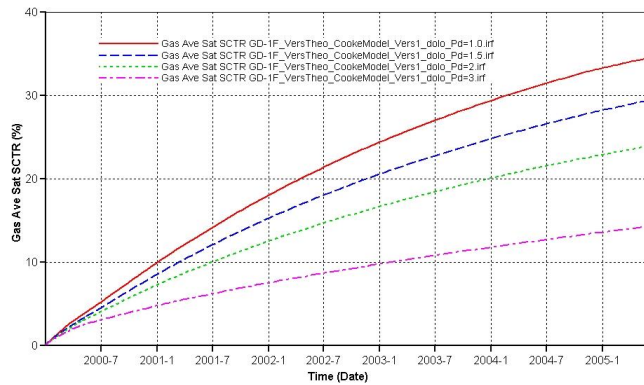


Figure 33: Figure presents the average gas saturation as a function of time and a function of threshold capillary pressure for the Cooke model. The y-axis of this figure can also be regarded as recovery.

For the Cooke model I then calculated the **dimensionless gravity number**.

$$N_{gv} = \frac{(\rho_w - \rho_g) g k}{\mu_w v_T \phi}$$

where v_T is the total velocity, g is the gravitational constant ($9.81 \frac{m}{s^2}$), and k is the absolute permeability. The gravity number gives the ratio between gravity to viscous forces and helps to determine whether flow is gravity-dominated or viscous-dominated. The gravity number N_{gv} has been defined in Hagoort [1980]⁸ and Juanes and Patzek [2003].⁵⁴ I calculated the absolute permeability by applying a geometric mean

$$k = \sqrt{k_x k_z}$$

where k_x and k_z are the permeabilities in x- and z-directions. Computing total velocity in CMG requires some post processing because IMEX simulator just gives vector components of the water and gas velocities. Therefore some computational manipulations are needed. For the total velocity vector I used the sum of gas and water vectors

$$\vec{v}_T = \vec{v}_g + \vec{v}_w = \begin{pmatrix} v_{gx} + v_{wx} \\ v_{gz} + v_{wz} \end{pmatrix}$$

The total velocity is found from the norm of the vector

$$v_T = \|\vec{v}_T\| = \sqrt{(v_{gx} + v_{wx})^2 + (v_{gz} + v_{wz})^2}$$

The motivation for the computation of N_{gv} was to identify regions where gravity effects dominated over viscous effects. The gravity number as a function of time was obtained for the entire Cooke model. The results shows very high gravity numbers in the fractures. This is logical because of the large fracture permeability. In general, layers that were drained and whose saturations had been lowered had higher N_{gv} than layers that remained untouched. At the end of the simulations a slight relation between wetting phase saturation and gravity number existed. I also observed that N_{gv} increases in close proximity to the fractures. I assume that these regions were affected by gravity drainage.

Unfortunately, the computation of gravity number did not provide too much new information or insight.

I also plotted the wetting phase velocity components for z- and x-directions. While models 1 to 3 show only little lateral flow, this is not true for the Cooke model. Here the simultaneous existence of numerous vertical fractures as well as horizontal low-permeable layers leads to lateral flow. Lateral flow of gas and oil occurs mainly in the dolomite layers with a k_x of $100md$. Values of velocity in the x-direction are much smaller for the shale layers. Vertical flow, on the other hand, is mainly present in the fractures and to a small degree in the rock matrix. The results indicate the flow direction of the wetting phase in the Cooke model. Gas enters the fractures first and then reaches the highly-permeable dolomite layers, where it overcomes the resistance of rock capillary pressure entering the rock matrix blocks. Displacement can be seen as a combined movement in the z-direction within the fractures and the x-direction within the rock layers.

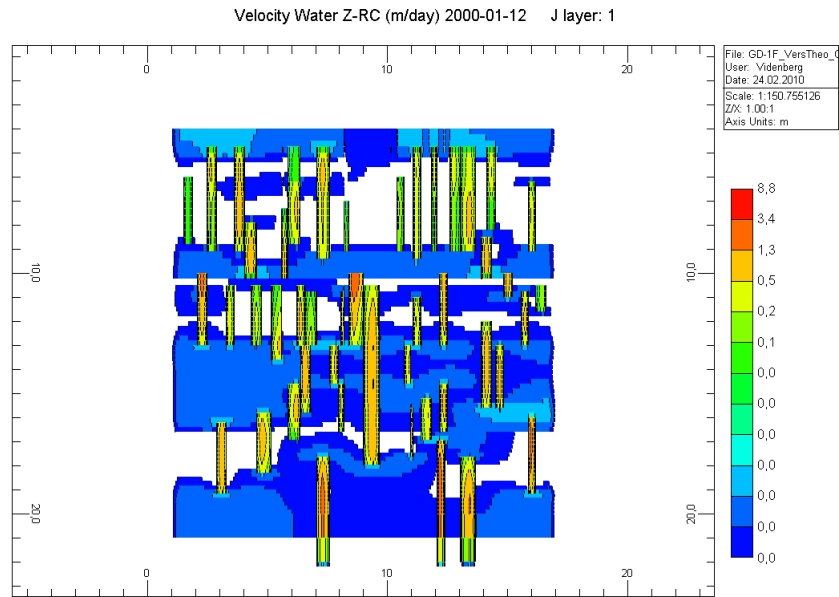


Figure 34: Wetting phase velocity in z-direction in Cooke model. The figure shows that the fractures are the pathways for vertical movement.

4 Discussion

Figures 10 and 11 present the influence of parameters like permeability and porosity on gravity drainage. They verify the already known fact that high matrix permeabilities and low matrix porosities have a positive effect on GOGD. Figure 13 confirms that the drainage capillary pressure curve is acting to hold back the oil in the model. It also suggests that the height of the capillary hold-up zone can be backcalculated from the capillary threshold pressure. The influence of large density differences between wetting and non-wetting phases on GOGD recovery is presented and follows generally accepted trends.

Figure 15 shows the change in saturation distribution over time and model height. The results show that the oil saturation changes over time to a final curve that depends on the capillary pressure curve. This is in direct agreement with findings from Terwilliger et al.[1951].⁵

For models with a single vertical fracture no increase in recovery was observed as compared to same model with no fracture. Other simulations also suggest that recovery of GOGD is affected by boundary conditions. Throughout the study I made the observations that fractures speed up GOGD recovery, when certain boundary conditions are present. For instance, the presence of low permeability barriers combined with vertical fractures increases the effect of fractures on GOGD. My suggestion is that those low permeability layers act as a flow hindrance, therefore leading to horizontal flow towards the fracture. As a further conclusion my results indicate that vertical fractures enhance GOGD in heterogeneous reservoirs that have several low permeability layers.

Results also indicate that if the fracture permeability exceeds a certain value GOGD recovery curves are identical. This would lead to the suggestion that fracture permeability is not a critical factor if a certain fracture/matrix permeability contrast is exceeded.

Further simulations seem to signal that the layer sequence (i.e. permeability order) is a factor in recovery. This issue has already been discussed with Correa et al. [1996].⁴⁹

Simulations of the realistic discrete model indicate that fractures increase the drainage speed and transport the gas to higher permeable layers, where GOGD can be initiated. Fractures are especially useful in lower permeable matrix rocks. This has also been investigated in Zandehboudi et al. [2008],⁴⁶ who note that “the presence of fractures is more pronounced in lower matrix permeability systems”. Especially in low permeable layered formations the presence of fractures

can dramatically increase GOGD drainage speed. This is an important factor that needs to be considered in terms of profitability and other economic aspects. The question of hydraulic fracturing should also be addressed.

A sensitivity analysis on the general parameters (e.g. oil density and viscosity, gas density) confirms their importance for GOGD recovery. The use of a non-zero capillary pressure in the fractures can increase the recovery that can be expected from GOGD in NFR. This is in agreement with Saidi and Sakthikumar [1993].¹⁰ However, I believe that by using a zero capillary pressure in the fracture the user is on the safe side and can only slightly underestimate recovery. I have the opinion that underestimating recovery is the better alternative than a too optimistic recovery prediction.

In addition my results suggest that increased pore size distribution indices increase GOGD recovery. I believe that the reason is the simultaneous increase in oil relative permeability and the decrease in the matrix capillary pressure. Li and Horne [2003]¹³ support that and say that “oil recovery by gravity drainage may increase with the pore size distribution index”. Dolomites usually only have secondary porosity. Pore sizes then are selectively uniform with some large vugs in places.

Unfortunately, the computation of the dimensionless gravity number for the entire model could not give any new insights. The question whether gravity number can be a predictive tool should be addressed with care.

I calculated the effective permeability for models 1 to 3. Due to the fracture the effective permeability is significantly increased. However, my simulation results did not correlate with the increased effective permeability. Calculating the effective permeability for the Cooke model is very complicated and also did not correlate with simulation results. I suggest that using the effective permeability (i.e. averaging) for fractured media is of limited advantage and should be considered with great criticism. Matthäi and Belayneh [2004]⁵⁸ state that “the k_{eff} is rarely a useful average for fractured media”.

My work disagrees with Zandehboudi et al.[2008], who mention that oil-gas contact height in the fracture needs to be controlled. My simulations indicate that the fractures are quickly drained from the oil and get gas filled. This would imply that controlling the gas-oil interface in the fracture is a challenging task.

Based on results that indicate that fractures play a minor role in cases of high-permeability layers or when they do not penetrate low-permeability layers I believe that simplifying the NFR analog in my proposed method is applicable (Fig.9). Nevertheless, the representation of fractures through structured sim-

ulators needs to be called into question. The University of Leoben license for CMG simulator has a maximum of 50 000 grid blocks. This is a restriction of the work. Unstructured simulators certainly have advantages over structured simulators in terms of accurate geologic representation.

My work is one of the first simulations of GOGD in NFR using discrete fracture and matrix models. It shows that simulation of GOGD in NFR with discrete models can be a good alternative to previously used dual continuum models, if restrictions in geometric representation of geology can be overcome. Definitely, further research is needed concerning DFM models.

5 Conclusions

I have investigated the process of GOGD with the help of three simple conceptual models and one more realistic model, based on field observations from Door County, Wisconsin, USA. These models have been simulated with a proprietary reservoir simulator and a DFM model. Following **conclusions** can be reached:

- GOGD recovery increases with a higher density difference between oil and gas.
- GOGD recovery increases with a decrease in oil viscosity.
- The shape of the oil relative permeability and capillary pressure curve determine amount of recoverable oil and drainage speed.
- GOGD in models with one single vertical fracture is just influenced when low-permeable layers exist that create some horizontal flow.
- Permeability sequence of layers influences final recovery in GOGD.
- Averaging of layer and fracture permeabilities to an overall effective permeability can lead to erroneous results.
- Recovery of GOGD is affected by boundary conditions.
- Influence of fractures on GOGD is especially evident for reservoirs with lower matrix permeabilities.
- Oil recovery in GOGD increases with the pore size distribution index.
- Increased threshold capillary pressures in the dolomite layers had a negative effect on the GOGD recovery by increasing the capillary hold-up zone. Wetting phase saturations in the low permeability layers were also affected by changed dolomite threshold capillary pressures. In the Cooke model a dolomite threshold capillary pressure of 1 psi leads to an ultimate recovery of 35 %, while a P_d of 3 psi leads to recovery of 15 %.
- If the permeability contrast between matrix and fracture is large enough, an increase in fracture permeability does not significantly increase recovery. In the Cooke model this permeability contrast was reached for $5E+03$.

- Use of fracture capillary pressure increases oil recovery in GOGD processes. The use of a zero capillary pressure in the fracture can underestimate recovery. In the Cooke model the use of a P_{cf} of 1 kPa increased ultimate recovery by about 0.8%.
- The path of the gas in the realistic discrete model is the following: It is displaced vertically through the fractures and then horizontally enters the higher permeability layers, where GOGD is initiated. The existence of fractures helps the gas to bypass lower permeable layers. Fractures speed up GOGD process in NFR.
- Simulations on the more the realistic field model from Door County confirm the high potential of gas-oil gravity drainage in naturally fractured reservoirs.

I can make the following **recommendations** for future studies and field applications of GOGD in NFR:

- Laboratory experiments on gas-oil gravity drainage in fractured cores are recommended.
- Influence of fracture properties should be investigated.
- GOGD should also be simulated with reservoir simulators that use unstructured gridding and can improve geometry representations of models. Results of simulations of discrete fracture and matrix models should be contrasted with results from dual continuum models.
- The simulation of GOGD with three-phase flow to verify results from two-phase flow is recommended.
- GOGD simulation in 3D is recommended.
- Accurate measurement of critical variables like oil density, oil viscosity, oil relative permeability and capillary pressure is recommended for field applications.

References

- [1] Leverett, M.C.: “Capillary Behaviour in Porous Solids”, Petroleum Transactions, AIME, Vol.142, pp.152-169, 1941
- [2] Katz, D.L.: “Possibilities of Secondary Recovery for the Oklahoma City Wilcox Sand”, Petroleum Transactions, AIME, Vol.146, pp.28-53, 1942
- [3] Stahl, R.F., Martin, W.A., and Huntington, R.L.: “Gravitational Drainage of Liquids from Unconsolidated Wilcox Sand”, Petroleum Transactions, AIME, Vol.151, pp.138-146, 1943
- [4] Cardwell Jr., W.T., and Parsons, R.L.: “Gravity Drainage Theory”, Petroleum Transactions, AIME, Vol.179, pp.199-215, 1949
- [5] Terwilliger, P.L., Wilsey, L.E., Hall, H.N., Bridges, P.M., and Morse, R.A.: “An Experimental and Theoretical Investigation of Gravity Drainage Performance”, Petroleum Transactions, AIME, Vol.192, pp.285-296, 1951
- [6] Buckley, S.E., and Leverett, M.C.: “Mechanism of Fluid Displacement in Sands”, Petroleum Transactions, AIME, Vol.146, pp.107-116, 1942
- [7] Dykstra, H.: “The Prediction of Oil Recovery by Gravity Drainage”, SPE paper 6548 published in *Journal of Petroleum Technology*, Vol.30, No.5, pp.818-830, May 1978
- [8] Hagoort, J.: “Oil Recovery by Gravity Drainage”, paper SPE 7424 published in *SPE Journal*, Vol.20, No.3, pp.139-150, June 1980
- [9] Rossen, R.H., and Shen, E.I.C.: “Simulation of Gas/Oil Drainage and Water/Oil Imbibition in Naturally Fractured Reservoirs”, paper SPE 16982 published in *SPE Reservoir Engineering*, Vol. 4, No.4, pp.464-470, November 1989
- [10] Saidi, A.M. and Sakthikumar, S.: “Gas Gravity Drainage under Secondary and Tertiary Conditions in Fractured Reservoirs”, paper SPE 25614 presented at Middle East Oil Show, Bahrain, 3-6 April, 1993
- [11] Schechter, D.S., and Guo, B.: “Mathematical Modeling of Gravity Drainage After Gas Injection into Fractured Reservoirs”, paper SPE 35170 presented at the SPE Improved Oil Recovery Symposium in Tulsa, Oklahoma, USA, 22-24 April, 1996

- [12] Schechter, D.S., and Guo, B.: “An Integrated Investigation for Design of a CO₂ Pilot in the Naturally Fractured Spraberry Trend Area, West Texas”, paper SPE 39881 presented at the SPE International Petroleum Conference and Exhibition in Villahermosa, Mexico, 3-5 March, 1998
- [13] Li, K., and Horne, R.N.: “Prediction of Oil Production by Gravity Drainage”, SPE paper 84184 presented at SPE Annual Technical Conference and Exhibition, Denver, Colorado, USA, 5-8 October 2003
- [14] Mattax, C.C., Kyte, J.R.: “Imbibition Oil Recovery from Fractured, Water-Drive Reservoir”, paper SPE 187 published in *SPE Journal*, Vol.2, No.2, pp.177-184, June, 1962
- [15] de Swaan, A.: “Theory of Waterflooding in Fractured Reservoirs”, paper SPE 5892 published in *SPE Journal*, Vol.18, No.2, pp.117-122, April 1978
- [16] Kleppe, J., Morse, R.A.: “Oil Production from Fractured Reservoirs by Water Displacement”, paper SPE 5084 presented at Fall Meeting of the Society of Petroleum Engineers of AIME in Houston, Texas, USA, 6-9 October, 1974
- [17] Brooks, R.H., and Corey, A.T.: “Hydraulic Properties of Porous Media”, in *Hydrol. Pap.*, Vol.3, Fort Collins, Colorado State University, 1964
- [18] Van Genuchten, M.Th.: “A Closed-Form Equation for Predicting the Hydraulic Conductivity of Unsaturated Soils”, published in *Soil Sci. Soc. Am. J.*, 44:892-898, 1980
- [19] Mualem, Y.: “A new model for predicting the hydraulic conductivity of unsaturated porous media”, published in *Water Resources Research*, 12:513-522, 1976
- [20] Lenhard, R.J., Parker, J.C., and Mishra, S.: “On the Correspondence Between Brooks-Corey and Van Genuchten Models”, published in *Journal of Irrigation and Drainage Engineering*, Vol.115, No.4, pp.744-751, July/August 1989
- [21] Kazemi, H., Merrill, L.S.: “Numerical Simulation of Water Imbibition in Fractured Cores”, paper SPE 6895 published in *SPE Journal*, Vol.19, No.3, pp.175-182, June 1979

- [22] Fourar, M., and Bories, S., Lenormand, R., Persoff, P.: “Two-Phase Flow in Smooth and Rough Fractures: Measurement and Correlation by Porous-Medium and Pipe Flow Models”, published in *Water Resources Research*, Vol.29, No.11, pp.3699-3708, November 1993
- [23] Romm, E.S.: “Fluid Flow in Fractured Rocks” (English translation) W.R. Blake (transl.), Phillips Petroleum Co., Bartlesville, Oklahoma, USA, 1972
- [24] Firoozabadi, A., and Hauge, J.: “Capillary Pressure in Fractured Porous Media”, paper SPE 18747 published in *Journal of Petroleum Technology*, Vol.42, No.6, pp.784-791, June 1990
- [25] Rangel-German, E., Akin, S., Castanier, L.: “Multiphase-flow properties of fractured porous media”, published in *Journal of Petroleum Science and Engineering*, Vol.51, Issues 3-4, pp.197-213, May 2006
- [26] De la Porte, J.J., Kossack, C.A., and Zimmerman, R.W.: “The Effect of Fracture Relative Permeabilities and Capillary Pressures on the Numerical Simulation of Naturally Fractured Reservoirs”, paper SPE 95241 presented at SPE Annual Technical Conference and Exhibition, Dallas, Texas, USA, 9-12 October 2005
- [27] Du Prey, Lefebvre E.: “Gravity and Capillarity Effects on Imbibition in Porous Media”, paper SPE 6192 published in *SPE Journal*, Vol.18, No.3, pp.195-206, June 1978
- [28] Schechter, D.S., Zhou, D., Orr, F.M.Jr.: “Low IFT drainage and imbibition”, published in *Journal of Petroleum Science and Engineering*, Vol.11, Issue 4, pp.283-300, September 1994
- [29] Matthäi, S.K., Geiger, S., and Roberts, S.G.: “Complex Systems Platform (CSP 5.0) User’s Guide”, 2004
- [30] Stüben, K.: “A review of algebraic multigrid”, published in *Journal of Computational and Applied Mathematics*, Vol. 128, Issue 1-2, pp.281-309, March 2001
- [31] Stüben, K.: “Algebraic Multigrid (AMG): An Introduction with Applications”, GMD Forschungszentrum Informationstechnik GmbH, St. Augustin, Germany, Report 70, 1999

- [32] Stüben, K., Delaney, P., Chmakov, S.: “Algebraic Multigrid (AMG) for Ground Water Flow and Oil Reservoir Simulation”, presented at Groundwater Modelling Conference “MODFLOW and MORE” at Colorado School of Mines, Golden, Colorado, USA, Sept 17-19, 2003
- [33] Helmig, R.: “Multiphase Flow and Transport Processes in the Subsurface: A Contribution to the Modeling of Hydrosystems”, first edition, 1997. Berlin, New York: Springer Verlag. ISBN 3540627030
- [34] Klima, R.: “Three-Dimensional Device Simulation with Minimos-NT”, PhD Dissertation, Technische Universität Wien, November 2002
- [35] Geiger, S., Roberts, S., Matthäi, S.K., Zoppou, C.: “Combining finite volume and finite element method to simulate fluid flow in geologic media”, published in ANZIAM J. 44(E), pp. C180-201, 2003
- [36] Randall J. LeVeque: “Finite Difference Methods for Differential Equations”, lecture notes AMATH 585, University of Washington, January 2006
- [37] Mandefro Belayneh, Stephan Matthai, Andrey Mezentsev, Richard Tomlinson: “CSP Model Building & Interface Guide”, 2005
- [38] Verma, S.K.: “Flexible grids for reservoir simulation”, PhD Dissertation, Stanford University, 1996
- [39] Matthäi, S.K., Nick, H.M., Pain, C., Neuweiler, I.: “Simulation of Solute Transport Through Fractured Rock: A Higher-Order Accurate Finite-Element Finite-Volume Method Permitting Large Time Steps”, published in *Transp. Porous Med.*, DOI 10.1007/s11242-009-9440-z (July 2009)
- [40] Wayne Narr, David S. Schechter, Laird B. Thompson: “Naturally Fractured Reservoir Characterization”, SPE, 115pp, ISBN: 978-1-55563-112-3, 2006
- [41] User’s Guide “CMG Technologies Launcher”, User’s Guide “Builder”, User’s Guide “IMEX” by Computer Modelling Group Ltd., Versions 2009
- [42] Kazemi, H.: lecture notes to “PEGN 620A: Naturally Fractured Reservoirs-Engineering & Reservoir Simulation”, Fall 2008, Colorado School of Mines, Golden, CO, USA
- [43] Gilman, J.R.: “Practical Aspects of Simulation of Fractured Reservoirs”, presented at International Forum on Reservoir Simulation June 23-27, 2003, Baden-Baden, Germany

- [44] Cooke, M.L., Simo, J.A., Underwood, Ch.A., Rijken, P.: “Mechanical stratigraphic controls on fracture patterns within carbonates and implications for groundwater flow”, published in *Sedimentary Geology*, Vol. 184, pp.225-239, 2006
- [45] Zendehboudi, S., Mohammadzadeh, O., Chatzis, I.: “Experimental Study of Controlled Gravity Drainage in Fractured Porous Media”, presented at the Canadian International Petroleum Conference (CIPC) in Calgary, Canada, June 16-18, 2009
- [46] Zendehboudi, S., Mohammadzadeh, O., Chatzis, I.: “Investigation of Gravity Drainage in Fractured Porous Media Using Rectangular Macromodels”, presented at the Canadian International Petroleum Conference (CIPC) in Calgary, Canada, June 17-19, 2008
- [47] Graves, R.M.: lecture notes to “PEGN 508: Advanced Rock Properties”, Fall 2008, Colorado School of Mines, Golden, CO, USA
- [48] Miguel-Hernandez, Nemesio: “Scaling Parameters for Characterizing Gravity Drainage in Naturally Fractured Reservoir”, PhD Dissertation, University of Texas at Austin, 2002
- [49] Correa, A.C.F., Firoozabadi, A.: “Concept of Gravity Drainage in Layered Porous Media”, published in *SPE Journal*, Vol.1, No.1, pg.101-111, March 1996
- [50] Karimaie, H., and Torsaeter: “Low IFT Gas-Oil Gravity Drainage in Fractured Carbonate Porous Media”, presented at Europec/EAGE Conference and Exhibition June 9-12, 2008, Rome, Italy
- [51] Luan, Zhi-An: “Some Theoretical Aspects of Gravity Drainage in Naturally Fractured Reservoirs”, paper SPE 28641 presented at the SPE Annual Technical Conference and Exhibition in New Orleans, LA, USA, September 25-28, 1994
- [52] Utley, L.: “Unconventional Petrophysical Analysis in Unconventional Reservoirs- Putting the Puzzle Together in Gas Shales”, presented at Houston Chapter SPWLA Spring Seminar, Houston, TX, USA, May 2005 (www.utleypetro.com/presentations/barnettshale.ppt)

- [53] Reed, R.M.: “Nanopores in the Mississippian Barnett Shale: Distribution, morphology, and possible genesis”, presented at 2007 GSA Annual Meeting, Denver, CO, USA, 28-31 October, 2007
- [54] Juanes, R., and Patzek, T.W.: “Relative Permeabilities in Co-Current Three-Phase Displacements With Gravity”, paper SPE 83445 presented at SPE Western Regional/ AAPG Pacific Section Joint Meeting in Long Beach, CA, USA, 19-24 May, 2003
- [55] Jacquin, Ch., Legait, B., Martin, J.M., Nectoux, A., Anterion, F., and Rioche, M.: “Gravity drainage in fissured reservoir with fluids not in equilibrium”, published in *Journal of Petroleum Science and Engineering*, 2 (1989), 217-224
- [56] Jadhawar, P.S., and Sarma, H.K.: “Scaling and Sensitivity Analysis of Gas-Oil Gravity Drainage EOR”, paper SPE 115065 presented at the 2008 SPE Asia Pacific Oil & Gas Conference and Exhibition, Perth, Australia, 20-22 October, 2008
- [57] Nelson, R.A.: “Geologic Analysis of naturally fractured reservoirs”, 2nd edition, Gulf Professional Publishing, ISBN 0-88415-317-7, 2001
- [58] Matthäi, S.K., and Belayneh, M.: “Fluid flow partitioning between fractures and a permeable rock matrix”, published in *Geophysical Research Letters*, Vol.31, L07602, doi:10.1029/2003GL019027, 2004

Appendix A

.dat-File used for Cooke model

```
INUNIT SI
WSRF WELL 1
WSRF GRID TIME
WSRF SECTOR TIME
OUTSRF WELL LAYER NONE
OUTSRF RES ALL
OUTSRF GRID BPP OILPOT PRES SG SO SSPRES SW VELOCRC WIN-
FLUX
WPRN GRID 0 OUTPRN GRID NONE OUTPRN RES NONE
**$ Distance units: m
RESULTS XOFFSET 0.0000
RESULTS YOFFSET 0.0000
RESULTS ROTATION 0.0000 **$ (DEGREES)
RESULTS AXES-DIRECTIONS 1.0 -1.0 1.0 **$ *
* **$ Definition of fundamental cartesian grid **$ **
*** GRID VARI 125 1 84
KDIR DOWN
DI IVAR
1 4*0.166 0.001 3*0.203 0.001 0.2 0.151 0.001 0.25 0.251 0.001 0.15 0.109 0.001
2*0.22 0.001 0.2 0.285 0.001 0.215 0.001 0.23 0.001 2*0.395 0.001 2*0.039 0.001
0.2 0.389 0.001 0.142 0.001 0.185 0.001 0.235 0.001 2*0.25 0.001 0.3 0.255 0.001
2*0.106 0.001 0.113 0.001 0.016 0.001 0.2 0.201 0.001 2*0.406 0.001 4*0.245 0.001
0.032 0.001 2*0.262 0.001 0.003 0.001 2*0.116 0.001 0.2 0.317 0.001 2*0.126 0.001
2*0.104 0.001 0.219 0.001 0.11 0.001 0.1 0.141 0.001 0.3 0.391 0.001 3*0.234 0.001
0.198 0.001 2*0.172 0.001 2*0.162 0.001 4*0.188 0.001 2*0.101 0.001 0.2 0.317
0.001 3*0.121 0.166 1
DJ JVAR 1
DK KVAR 4*1 4*0.25 10*0.2 10*0.3 4*0.25 10*0.2 8*0.2 10*0.2 20*0.17 4*1
DTOP 125*0
**$ Property: NULL Blocks Max: 1 Min: 1
**$ 0 = null block, 1 = active block
```

NULL CON 1

**\$ Property: Porosity Max: 0.2 Min: 0.2

POR CON 0.2

*MOD

2:124 1:1 5:8 = 0.2 2:124 1:1 9:13 = 0.06 2:124 1:1 14:18 = 0.2 2:124 1:1 19:28
= 0.06 2:124 1:1 29:29 = 0.2 2:124 1:1 30:30 = 0.06 2:124 1:1 31:32 = 0.2 2:124
1:1 33:36 = 0.2 2:124 1:1 37:37 = 0.06 2:124 1:1 38:42 = 0.2 2:124 1:1 43:50 =
0.2 2:124 1:1 51:60 = 0.2 2:124 1:1 61:80 = 0.06

6:6 1:1 14:24 = 0.999 10:10 1:1 29:42 = 0.999 13:13 1:1 9:25 = 0.999 16:16
1:1 59:75 = 0.999 19:19 1:1 31:42 = 0.999 22:22 1:1 9:25 = 0.999 25:25 1:1 22:28
= 0.999 27:27 1:1 31:42 = 0.999 29:29 1:1 57:70 = 0.999 32:32 1:1 31:45 = 0.999
35:35 1:1 5:8 = 0.999 35:35 1:1 9:29 = 0.999 38:38 1:1 51:62 = 0.999 38:38 1:1
9:24 = 0.999 40:40 1:1 31:42 = 0.999 42:42 1:1 43:56 = 0.999 44:44 1:1 32:42 =
0.999 47:47 1:1 9:26 = 0.999 47:47 1:1 67:80 = 0.999 50:50 1:1 43:50 = 0.999
57:57 1:1 5:25 = 0.999 55:55 1:1 32:42 = 0.999 53:53 1:1 51:60 = 0.999 60:60 1:1
29:42 = 0.999 63:63 1:1 31:68 = 0.999 70:70 1:1 14:25 = 0.999 68:68 1:1 5:8 =
0.999 75:75 1:1 56:66 = 0.999 73:73 1:1 43:50 = 0.999 78:78 1:1 33:42 = 0.999
78:78 1:1 9:26 = 0.999 81:81 1:1 54:62 = 0.999 81:81 1:1 5:8 = 0.999 84:84 1:1
9:25 = 0.999 87:87 1:1 5:8 = 0.999 87:87 1:1 63:80 = 0.999 89:89 1:1 51:60 =
0.999 89:89 1:1 29:42 = 0.999 91:91 1:1 5:8 = 0.999 94:94 1:1 9:25 = 0.999 97:97
1:1 9:25 = 0.999 97:97 1:1 67:80 = 0.999 101:101 1:1 38:55 = 0.999 101:101 1:1
24:28 = 0.999 103:103 1:1 9:22 = 0.999 106:106 1:1 43:55 = 0.999 109:109 1:1
29:32 = 0.999 114:114 1:1 32:42 = 0.999 117:117 1:1 15:25 = 0.999 117:117 1:1
58:75 = 0.999 120:120 1:1 31:35 = 0.999

1:125 1:1 1:4 = 0.999 1:125 1:1 81:84 = 0.999 1:1 1:1 1:84 = 0.999 125:125
1:1 1:84 = 0.999

**\$ Property: Permeability I (md) Max: 100 Min: 100 PERMI CON 100

*MOD

2:124 1:1 5:8 = 100 2:124 1:1 9:13 = 1 2:124 1:1 14:18 = 100 2:124 1:1 19:28
= 1 2:124 1:1 29:29 = 100 2:124 1:1 30:30 = 1 2:124 1:1 31:32 = 100 2:124 1:1
33:36 = 100 2:124 1:1 37:37 = 1 2:124 1:1 38:42 = 100 2:124 1:1 43:50 = 100
2:124 1:1 51:60 = 100 2:124 1:1 61:80 = 1

6:6 1:1 14:24 = 1e+006 10:10 1:1 29:42 = 1e+006 13:13 1:1 9:25 = 1e+006
16:16 1:1 59:75 = 1e+006 19:19 1:1 31:42 = 1e+006 22:22 1:1 9:25 = 1e+006
25:25 1:1 22:28 = 1e+006 27:27 1:1 31:42 = 1e+006 29:29 1:1 57:70 = 1e+006
32:32 1:1 31:45 = 1e+006 35:35 1:1 5:8 = 1e+006 35:35 1:1 9:29 = 1e+006 38:38
1:1 51:62 = 1e+006 38:38 1:1 9:24 = 1e+006 40:40 1:1 31:42 = 1e+006 42:42

1:1 43:56 = 1e+006 44:44 1:1 32:42 = 1e+006 47:47 1:1 9:26 = 1e+006 47:47
1:1 67:80 = 1e+006 50:50 1:1 43:50 = 1e+006 57:57 1:1 5:25 = 1e+006 55:55
1:1 32:42 = 1e+006 53:53 1:1 51:60 = 1e+006 60:60 1:1 29:42 = 1e+006 63:63
1:1 31:68 = 1e+006 70:70 1:1 14:25 = 1e+006 68:68 1:1 5:8 = 1e+006 75:75 1:1
56:66 = 1e+006 73:73 1:1 43:50 = 1e+006 78:78 1:1 33:42 = 1e+006 78:78 1:1
9:26 = 1e+006 81:81 1:1 54:62 = 1e+006 81:81 1:1 5:8 = 1e+006 84:84 1:1 9:25
= 1e+006 87:87 1:1 5:8 = 1e+006 87:87 1:1 63:80 = 1e+006 89:89 1:1 51:60
= 1e+006 89:89 1:1 29:42 = 1e+006 91:91 1:1 5:8 = 1e+006 94:94 1:1 9:25 =
1e+006 97:97 1:1 9:25 = 1e+006 97:97 1:1 67:80 = 1e+006 101:101 1:1 38:55 =
1e+006 101:101 1:1 24:28 = 1e+006 103:103 1:1 9:22 = 1e+006 106:106 1:1 43:55
= 1e+006 109:109 1:1 29:32 = 1e+006 114:114 1:1 32:42 = 1e+006 117:117 1:1
15:25 = 1e+006 117:117 1:1 58:75 = 1e+006 120:120 1:1 31:35 = 1e+006
1:125 1:1 81:84 = 1e+006 2:2 1:1 5:80 = 0 124:124 1:1 5:80 = 0 1:125 1:1 1:4
= 1e+006 1:1 1:1 1:84 = 1e+006 125:125 1:1 1:84 = 1e+006
PERMJ EQUALSI * 0.1
PERMK EQUALSI * 0.1
**\$ Property: Volume Modifiers Max: 1 Min: 1
VOLMOD CON 1
*MOD
1:125 1:1 81:84 = 1000 1:125 1:1 1:4 = 1000
**\$ Property: Pinchout Array Max: 1 Min: 1
**\$ 0 = pinched block, 1 = active block
PINCHOUTARRAY CON 1
SECTORARRAY 'PayZone' ALL
502*0 121*1 4*0 121*1 4*0 121*1 4*0 121*1 4*0 121*1 4*0 121*1 4*0 121*1 4*0
121*1 4*0 121*1 4*0 121*1 4*0 121*1 4*0 121*1 4*0 121*1 4*0 121*1 4*0
4*0 121*1 4*0 121*1 4*0 121*1 4*0 121*1 4*0 121*1 4*0 121*1 4*0
121*1 4*0 121*1 4*0 121*1 4*0 121*1 4*0 121*1 4*0 121*1 4*0 121*1
4*0 121*1 4*0 121*1 4*0 121*1 4*0 121*1 4*0 121*1 4*0 121*1 4*0
121*1 4*0 121*1 4*0 121*1 4*0 121*1 4*0 121*1 4*0 121*1 4*0 121*1
4*0 121*1 4*0 121*1 4*0 121*1 4*0 121*1 4*0 121*1 4*0 121*1 4*0
121*1 4*0 121*1 4*0 121*1 4*0 121*1 4*0 121*1 4*0 121*1 4*0 121*1
4*0 121*1 4*0 121*1 4*0 121*1 4*0 121*1 4*0 121*1 4*0 121*1 4*0
4*0 121*1 502*0
CPOR 6.894e-005
PVCUTOFF 0

MODEL GASWATER

TRES 150

PVTG EG 1

**\$ p Eg visg 101.325 0.685271 0.0144676 554.17 3.7652 0.0145029 1007.02
6.87312 0.0145517 1459.86 10.0085 0.0146098 1912.71 13.171 0.0146753 2365.55
16.3597 0.0147473 2818.4 19.5741 0.0148254 3271.24 22.8134 0.0149091 3724.09
26.0766 0.0149981 4176.93 29.3629 0.0150923 4629.78 32.6711 0.0151913 5082.62
36.0002 0.0152953 5535.47 39.3488 0.0154039 5988.31 42.7156 0.0155172 6441.16
46.0993 0.015635 6894 49.4984 0.0157573

BWI 1.08587

CVW 0

CW 6.17547e-007

DENSITY WATER 920.506

REFPW 101.325

VWI 1

GRAVITY GAS 0.8

ROCKFLUID RPT 1

SWT

**\$ Sw krw Pcgw 0.18 0 20.1603926 0.235 0.0003 16.9695127 0.32 0.0050 12.4283723
0.405 0.0207 10.6103431 0.49 0.0540 9.53534408 0.575 0.1118 8.79544671 0.66
0.2006 8.24220074 0.745 0.3271 7.80621996 0.83 0.4981 7.44993496 0.915 0.7201
7.15090739 1 1 6.89475729 SLT **\$ Sl krg 0.18 0.5 0.235 0.40598 0.32 0.285138
0.405 0.1910202 0.49 0.1202926 0.575 0.069613 0.66 0.03564226 0.745 0.01503658
0.83 0.00445528 0.915 0.00055691 1 0 RPT 2 SWT **\$ Sw krw 0 0 1 1 SLT **\$ Sl
krg 0 1 1 0 RPT 3 SWT **\$ Sw krw Pcgw 0.15 0 83.888 0.2 0.000015 37.48912 0.3
0.0011355 22.7526459 0.4 0.00836 18.0381 0.5 0.031162 15.479956 0.6 0.083230
13.80888 0.7 0.182374 12.6050 0.8 0.35040 11.6833482 0.9 0.61307 10.947584 1
1 10.3421

SLT

**\$ Sl krg 0.15 0.7 0.2 0.62349604 0.3 0. 4832 0.4 0.36 0.5 0.254185 0.6 0.166012
0.7 0.0958563 0.8 0.04420 0.9 0.011769 1 0

**\$ Property: Rel Perm Set Num Max: 1 Min: 1

RTYPE CON 1

*MOD

2:124 1:1 5:8 = 3 2:124 1:1 9:13 = 1 2:124 1:1 14:18 = 3 2:124 1:1 19:28 = 1
2:124 1:1 29:29 = 3 2:124 1:1 30:30 = 1 2:124 1:1 31:32 = 3 2:124 1:1 33:36 = 3
2:124 1:1 37:37 = 1 2:124 1:1 38:42 = 3 2:124 1:1 43:50 = 3 2:124 1:1 51:60 = 3

2:124 1:1 61:80 = 1
 6:6 1:1 14:24 = 2 10:10 1:1 29:42 = 2 13:13 1:1 9:25 = 2 16:16 1:1 59:75 =
 2 19:19 1:1 31:42 = 2 22:22 1:1 9:25 = 2 25:25 1:1 22:28 = 2 27:27 1:1 31:42 =
 2 29:29 1:1 57:70 = 2 32:32 1:1 31:45 = 2 35:35 1:1 5:8 = 2 35:35 1:1 9:29 = 2
 38:38 1:1 51:62 = 2 38:38 1:1 9:24 = 2 40:40 1:1 31:42 = 2 42:42 1:1 43:56 = 2
 44:44 1:1 32:42 = 2 47:47 1:1 9:26 = 2 47:47 1:1 67:80 = 2 50:50 1:1 43:50 = 2
 57:57 1:1 5:25 = 2 55:55 1:1 32:42 = 2 53:53 1:1 51:60 = 2 60:60 1:1 29:42 = 2
 63:63 1:1 31:68 = 2 70:70 1:1 14:25 = 2 68:68 1:1 5:8 = 2 75:75 1:1 56:66 = 2
 73:73 1:1 43:50 = 2 78:78 1:1 33:42 = 2 78:78 1:1 9:26 = 2 81:81 1:1 54:62 = 2
 81:81 1:1 5:8 = 2 84:84 1:1 9:25 = 2 87:87 1:1 5:8 = 2 87:87 1:1 63:80 = 2 89:89
 1:1 51:60 = 2 89:89 1:1 29:42 = 2 91:91 1:1 5:8 = 2 94:94 1:1 9:25 = 2 97:97
 1:1 9:25 = 2 97:97 1:1 67:80 = 2 101:101 1:1 38:55 = 2 101:101 1:1 24:28 = 2
 103:103 1:1 9:22 = 2 106:106 1:1 43:55 = 2 109:109 1:1 29:32 = 2 114:114 1:1
 32:42 = 2 117:117 1:1 15:25 = 2 117:117 1:1 58:75 = 2 120:120 1:1 31:35 = 2
 1:125 1:1 1:4 = 2 1:125 1:1 81:84 = 2 1:1 1:1 1:84 = 2 125:125 1:1 1:84 = 2
 INITIAL
 USER_INPUT
 DATUMDEPTH 50 INITIAL
 **\$ Property: Pressure (kPa) Max: 3450 Min: 3450
 PRES CON 3450
 **\$ Property: Water Saturation Max: 1 Min: 1
 SW CON 1
 *MOD
 1:125 1:1 81:84 = 0 1:125 1:1 1:4 = 0 1:1 1:1 1:84 = 0 125:125 1:1 1:84 = 0
 NUMERICAL
 DTMIN 0.000001
 NCUTS 20
 PRECC 1e-6
 NORTH 70
 SDEGREE 3
 ITERMAX 80
 RUN
 DATE 2000 1 1 DATE 2000 1 2 DATE 2000 1 3 DATE 2000 1 4 DATE 2000
 1 5 DATE 2000 1 6 DATE 2000 1 7 DATE 2000 1 8 DATE 2000 1 9 DATE
 2000 1 10 DATE 2000 1 11 DATE 2000 1 12 DATE 2000 1 13 DATE 2000 1
 14 DATE 2000 1 15 DATE 2000 1 16 DATE 2000 1 17 DATE 2000 1 18 DATE
 2000 1 19 DATE 2000 1 20 DATE 2000 1 21 DATE 2000 1 22 DATE 2000 1

23 DATE 2000 1 24 DATE 2000 1 25 DATE 2000 1 26 DATE 2000 1 27 DATE
2000 1 28 DATE 2000 1 29 DATE 2000 1 30 DATE 2000 1 31 DATE 2000 2 1
DATE 2000 2 2 DATE 2000 2 3 DATE 2000 2 4 DATE 2000 2 5 DATE 2000 2 6
DATE 2000 2 7 DATE 2000 2 8 DATE 2000 2 9 DATE 2000 2 10 DATE 2000 2
11 DATE 2000 2 12 DATE 2000 2 13 DATE 2000 2 14 DATE 2000 2 15 DATE
2000 2 16 DATE 2000 2 17 DATE 2000 2 18 DATE 2000 2 19 DATE 2000 2
20 DATE 2000 2 21 DATE 2000 2 22 DATE 2000 2 23 DATE 2000 2 24 DATE
2000 2 25 DATE 2000 2 26 DATE 2000 2 27 DATE 2000 2 28 DATE 2000 2 29
DATE 2000 3 1 DATE 2000 3 2 DATE 2000 3 3 DATE 2000 3 4 DATE 2000 3 5
DATE 2000 3 6 DATE 2000 3 7 DATE 2000 3 8 DATE 2000 3 9 DATE 2000 3
10 DATE 2000 3 11 DATE 2000 3 12 DATE 2000 3 13 DATE 2000 3 14 DATE
2000 3 15 DATE 2000 3 16 DATE 2000 3 17 DATE 2000 3 18 DATE 2000 3
19 DATE 2000 3 20 DATE 2000 3 21 DATE 2000 3 22 DATE 2000 3 23 DATE
2000 3 24 DATE 2000 3 25 DATE 2000 3 26 DATE 2000 3 27 DATE 2000 3 28
DATE 2000 3 29 DATE 2000 3 30 DATE 2000 3 31 DATE 2000 4 1 DATE 2000
4 2 DATE 2000 4 3 DATE 2000 4 4 DATE 2000 4 5 DATE 2000 4 6 DATE 2000
4 7 DATE 2000 4 8 DATE 2000 4 9 DATE 2000 4 10 DATE 2000 4 11 DATE
2000 4 12 DATE 2000 4 13 DATE 2000 4 14 DATE 2000 4 15 DATE 2000 4
16 DATE 2000 4 17 DATE 2000 4 18 DATE 2000 4 19 DATE 2000 4 20 DATE
2000 4 21 DATE 2000 4 22 DATE 2000 4 23 DATE 2000 4 24 DATE 2000 4 25
DATE 2000 4 26 DATE 2000 4 27 DATE 2000 4 28 DATE 2000 4 29 DATE 2000
4 30 DATE 2000 5 1 DATE 2000 5 2 DATE 2000 5 3 DATE 2000 5 4 DATE
2000 5 5 DATE 2000 5 6 DATE 2000 5 7 DATE 2000 5 8 DATE 2000 5 9 DATE
2000 5 10 DATE 2000 5 11 DATE 2000 5 12 DATE 2000 5 13 DATE 2000 5
14 DATE 2000 5 15 DATE 2000 5 16 DATE 2000 5 17 DATE 2000 5 18 DATE
2000 5 19 DATE 2000 5 20 DATE 2000 5 21 DATE 2000 5 22 DATE 2000 5
23 DATE 2000 5 24 DATE 2000 5 25 DATE 2000 5 26 DATE 2000 5 27 DATE
2000 5 28 DATE 2000 5 29 DATE 2000 5 30 DATE 2000 5 31 DATE 2000 6
15.00000 DATE 2000 6 30.00000 DATE 2000 7 15.00000 DATE 2000 7 30.00000
DATE 2000 8 14.00000 DATE 2000 8 29.00000 DATE 2000 9 13.00000 DATE
2000 9 28.00000 DATE 2000 10 13.00000 DATE 2000 10 28.00000 DATE 2000
11 12.00000 DATE 2000 11 27.00000 DATE 2000 12 12.00000 DATE 2000 12
27.00000 DATE 2001 1 11.00000 DATE 2001 1 26.00000 DATE 2001 2 10.00000
DATE 2001 2 25.00000 DATE 2001 3 12.00000 DATE 2001 3 27.00000 DATE
2001 4 11.00000 DATE 2001 4 26.00000 DATE 2001 5 11.00000 DATE 2001 5
26.00000 DATE 2001 6 10.00000 DATE 2001 6 25.00000 DATE 2001 7 10.00000
DATE 2001 7 25.00000 DATE 2001 8 9.00000 DATE 2001 8 24.00000 DATE

2001 9 8.00000 DATE 2001 9 23.00000 DATE 2001 10 8.00000 DATE 2001 10
23.00000 DATE 2001 11 7.00000 DATE 2001 11 22.00000 DATE 2001 12 7.00000
DATE 2001 12 22.00000 DATE 2002 1 6.00000 DATE 2002 1 21.00000 DATE
2002 2 5.00000 DATE 2002 2 20.00000 DATE 2002 3 7.00000 DATE 2002 3
22.00000 DATE 2002 4 6.00000 DATE 2002 4 21.00000 DATE 2002 5 6.00000
DATE 2002 5 21.00000 DATE 2002 6 5.00000 DATE 2002 6 20.00000 DATE
2002 7 5.00000 DATE 2002 7 20.00000 DATE 2002 8 4.00000 DATE 2002 8
19.00000 DATE 2002 9 3.00000 DATE 2002 9 18.00000 DATE 2002 10 3.00000
DATE 2002 10 18.00000 DATE 2002 11 2.00000 DATE 2002 11 17.00000 DATE
2002 12 2.00000 DATE 2002 12 17.00000 DATE 2003 1 1.00000 DATE 2003 1
16.00000 DATE 2003 1 31.00000 DATE 2003 2 15.00000 DATE 2003 3 2.00000
DATE 2003 3 17.00000 DATE 2003 4 1.00000 DATE 2003 4 16.00000 DATE
2003 5 1.00000 DATE 2003 5 16.00000 DATE 2003 5 31.00000 DATE 2003 6
15.00000 DATE 2003 6 30.00000 DATE 2003 7 15.00000 DATE 2003 7 30.00000
DATE 2003 8 14.00000 DATE 2003 8 29.00000 DATE 2003 9 13.00000 DATE
2003 9 28.00000 DATE 2003 10 13.00000 DATE 2003 10 28.00000 DATE 2003
11 12.00000 DATE 2003 11 27.00000 DATE 2003 12 12.00000 DATE 2003 12
27.00000 DATE 2004 1 11.00000 DATE 2004 1 26.00000 DATE 2004 2 10.00000
DATE 2004 2 25.00000 DATE 2004 3 11.00000 DATE 2004 3 26.00000 DATE
2004 4 10.00000 DATE 2004 4 25.00000 DATE 2004 5 10.00000 DATE 2004 5
25.00000 DATE 2004 6 9.00000 DATE 2004 6 24.00000 DATE 2004 7 9.00000
DATE 2004 7 24.00000 DATE 2004 8 8.00000 DATE 2004 8 23.00000 DATE
2004 9 7.00000 DATE 2004 9 22.00000 DATE 2004 10 7.00000 DATE 2004 10
22.00000 DATE 2004 11 6.00000 DATE 2004 11 21.00000 DATE 2004 12 6.00000
DATE 2004 12 21.00000 DATE 2005 1 5.00000 DATE 2005 1 20.00000 DATE
2005 2 4.00000 DATE 2005 2 19.00000 DATE 2005 3 6.00000 DATE 2005 3
21.00000 DATE 2005 4 5.00000 DATE 2005 4 20.00000 DATE 2005 5 5.00000
DATE 2005 5 20.00000

RESULTS PINCHOUT-VAL 0.0002

RESULTS SPEC 'Permeability K' RESULTS SPEC SPECNOTCALCVAL
-99999 RESULTS SPEC REGION 'All Layers (Whole Grid)' RESULTS SPEC
REGIONTYPE 'REGION_ WHOLEGRID' RESULTS SPEC LAYERNUMB 0
RESULTS SPEC PORTYPE 1 RESULTS SPEC EQUALSI 1 0.1 RESULTS
SPEC STOP

RESULTS SPEC 'Permeability J' RESULTS SPEC SPECNOTCALCVAL
-99999 RESULTS SPEC REGION 'All Layers (Whole Grid)' RESULTS SPEC
REGIONTYPE 'REGION_ WHOLEGRID' RESULTS SPEC LAYERNUMB 0

RESULTS SPEC PORTYPE 1 RESULTS SPEC EQUALSI 1 0.1 RESULTS SPEC STOP

RESULTS SPEC 'Permeability I' RESULTS SPEC SPECNOTCALCVAL -99999 RESULTS SPEC REGION 'All Layers (Whole Grid)' RESULTS SPEC REGIONTYPE 'REGION_ WHOLEGRID' RESULTS SPEC LAYERNUMB 0 RESULTS SPEC PORTYPE 1 RESULTS SPEC CON 10 RESULTS SPEC STOP

RESULTS SPEC 'Porosity' RESULTS SPEC SPECNOTCALCVAL -99999 RESULTS SPEC REGION 'All Layers (Whole Grid)' RESULTS SPEC REGIONTYPE 'REGION_ WHOLEGRID' RESULTS SPEC LAYERNUMB 0 RESULTS SPEC PORTYPE 1 RESULTS SPEC CON 0.2 RESULTS SPEC STOP

RESULTS SPEC 'Pressure' RESULTS SPEC SPECNOTCALCVAL -99999 RESULTS SPEC REGION 'All Layers (Whole Grid)' RESULTS SPEC REGIONTYPE 'REGION_ WHOLEGRID' RESULTS SPEC LAYERNUMB 0 RESULTS SPEC PORTYPE 1 RESULTS SPEC CON 500 RESULTS SPEC STOP

RESULTS SPEC 'Rel Perm Set Num' RESULTS SPEC SPECNOTCALCVAL -99999 RESULTS SPEC REGION 'All Layers (Whole Grid)' RESULTS SPEC REGIONTYPE 'REGION_ WHOLEGRID' RESULTS SPEC LAYERNUMB 0 RESULTS SPEC PORTYPE 1 RESULTS SPEC CON 1 RESULTS SPEC STOP

RESULTS SPEC 'Water Saturation' RESULTS SPEC SPECNOTCALCVAL -99999 RESULTS SPEC REGION 'All Layers (Whole Grid)' RESULTS SPEC REGIONTYPE 'REGION_ WHOLEGRID' RESULTS SPEC LAYERNUMB 0 RESULTS SPEC PORTYPE 1 RESULTS SPEC CON 1 RESULTS SPEC STOP

RESULTS SPEC 'Grid Top' RESULTS SPEC SPECNOTCALCVAL -99999 RESULTS SPEC REGION 'Layer 1 - Whole layer' RESULTS SPEC REGIONTYPE 'REGION_ LAYER' RESULTS SPEC LAYERNUMB 1 RESULTS SPEC PORTYPE 1 RESULTS SPEC CON 0 RESULTS SPEC STOP

RESULTS SPEC 'Grid Thickness' RESULTS SPEC SPECNOTCALCVAL -99999 RESULTS SPEC REGION 'All Layers (Whole Grid)' RESULTS SPEC REGIONTYPE 'REGION_ WHOLEGRID' RESULTS SPEC LAYERNUMB 0 RESULTS SPEC PORTYPE 1 RESULTS SPEC CON 1 RESULTS SPEC STOP

RESULTS SPEC 'Volume Modifiers' RESULTS SPEC SPECNOTCALCVAL -99999 RESULTS SPEC REGION 'All Layers (Whole Grid)' RESULTS SPEC REGIONTYPE 'REGION_ WHOLEGRID' RESULTS SPEC LAYERNUMB

0 RESULTS SPEC PORTYPE 1 RESULTS SPEC CON 1 RESULTS SPEC
STOP

Appendix B

CSMP++ Software: Experimental Part

Introduction

This chapter will describe an experimental simulation software, which is still under heavy research, and which was used for some simulation purposes of this thesis. It will give an insight into the operating principles, partial differential equations that are solved, modeling workflow and will also discuss strengths and weaknesses of the software.

Complex Systems Modelling Platform

Complex Systems Modelling Platform (CSMP++ or CSP)²⁹ is an application programmer interface (API) invented and implemented by Stephan Matthäi during research stays at ANU, Stanford University, ETH Zurich and Imperial College London. It is programmed in C/C++ language, makes use of the C++ Standard Template Library (STL) and takes full advantage of object-oriented features like polymorphism and inheritance among others. It is fully compatible with the ANSI/ISO C++ standard and can run on Windows, Macintosh and Unix-Linux environments.

CSMP++ is based on mainly on the numerical method of finite element, but can also use finite volume and finite difference methods. It can work with elements like triangles and quadrilaterals in two dimensions and hexahedral and tetrahedral elements among others in three dimensions. For an efficient and realistic representation of geometry CSMP++ can also handle so-called hybrid meshes. Complex systems platform works with an unstructured grid, as opposed to structured Cartesian grids.

Use of finite volume and finite element methods to solve the governing partial differential equations leads to a linear algebraic equations of the form $A\vec{x} = \vec{b}$ after discretization, where \vec{x} is the unknown solution vector, while A is the known coefficient matrix and \vec{b} is the known right-hand side vector. A is a sparse, symmetrical and positive definite matrix which can contain millions of equations. The system of linear equations can be solved by algebraic multigrid methods³⁰⁻³² (e.g. AMG_Solver or SAMG_Solver). These methods work relatively fast

and matrix-inversion times relate to matrix size in a $n \log n$ fashion, where n is the number of matrix rows or columns. The equations can also be solved by direct methods like Gaussian elimination or conjugate gradient schemes, which, however, work in a n^2 fashion and are thus slower for solving large systems of equations.

Complex Systems Modelling Platform can be used for the solution of a wide area of physical problems like steady-state and transient pressure multi-phase flow, advection and heat dispersion, hydraulic fracturing, calcite dissolution precipitation and others.

Equations solved by CSMP++

In chapter 2 a mathematical formulation for the immiscible two-phase slightly compressible flow is presented. Although Complex System Modelling Platform solves similar equations it must be noted that CSP uses a modified formulation. The formulation closely follows the notation presented by Helmig [1997].³³ The step-by-step derivation is shown in the Appendix. In CSP no capillary continuity is assumed, which is a reasonable assumption when dealing with highly complex and heterogenous media. In the pressure equation hydrostatic pressure is included, but capillary pressure is not included

$$\phi c_t \frac{\partial p}{\partial t} - \nabla \cdot k [\lambda_t \nabla p + \vec{g} (\lambda_w \rho_w + \lambda_{nw} \rho_{nw})] - \hat{q}_t = 0 \quad (5.1)$$

where the subscripts w , nw , t denote wetting phase, non-wetting phase and total respectively. Other variables are the same as in chapter 4. Note also that the pressure in Eq.5.1 is not specified any further and can be viewed as the total pressure acting in the pore space of the media, while the pressure in Eq.2.8 denotes the oil pressure explicitly.

The saturation equation includes the capillary pressure effects and can be solved either explicitly or implicitly.

$$\phi \frac{\partial S_{nw}}{\partial t} + \nabla \cdot \left[f_{nw} \vec{v}_t - \bar{\lambda} k (\rho_w - \rho_{nw}) \vec{g} - \bar{\lambda} k \frac{dp_c}{dS_{nw}} \nabla S_{nw} \right] - \hat{q}_{nw} = 0 \quad (5.2)$$

In Eq.5.2 f denotes the fractional flow $f = \hat{q}/\hat{q}_t$ and $\bar{\lambda} = \lambda_w \lambda_{nw} / \lambda_t$. The pressure and saturation equations can be solved using an IMPES approach. CSMP++ uses a hybrid finite element- finite volume method to solve the two governing equations. While the finite element method is employed to solve the

pressure equation, the finite volume numerical method solves the saturation equation. The principle will be explained in the following section.

Combination of Finite Element and Finite Volume Methods

Introduction

The equations that are solved by CSMP++ are complex partial differential equations (PDE). The pressure is a function of both position and time. What makes things even more complicated is the higher order of the PDEs. Mathematical sciences have extensively dealt with PDEs and their solution. By definition the partial differential equations of the second order

$$a(x, y)f_{xx} + 2b(x, y)f_{xy} + c(x, y)f_{yy} + g(x, y, f_x, f_y, f) = 0$$

can be divided into three types, each having different preferred and recommended solution techniques. The coefficients a , b , and c are all functions of the variables x , y . The subscripts refer to the derivative (i.e. $f_{xx} = \frac{\partial^2 f}{\partial x^2}$). If we define $d = ac - b^2$ then

$$d = \begin{cases} > 0 & \textit{elliptic} \\ = 0 & \textit{parabolic} \\ < 0 & \textit{hyperbolic} \end{cases}$$

describes the type of the partial differential equations. Numerical methods to solve those involved equations are finite difference, finite volume and finite element methods. This section will give a short introduction on the available methods and will then specifically explain the solution technique that is being used by Complex Systems Modelling Platform.

Finite Volume Method

While the finite difference method works with derivatives and difference quotients and uses the actual partial differential equation, the finite volume method (FV) uses the integral form of the pressure equation. If we neglect depth then the general single-phase pressure-diffusion equation is given by

$$\nabla \cdot \frac{k}{\mu} \nabla p + \hat{q} - \phi c_t \frac{\partial p}{\partial t} = 0$$

where the variables are defined in the nomenclature. Then the integral form

of the equation is

$$\int_V \left(\nabla \frac{k}{\mu} \nabla p + \hat{q} - \phi c_t \frac{\partial p}{\partial t} \right) dV = 0$$

and with further simplifications and assuming that the total compressibility and the viscosity remain constant within the control volume then follows

$$\int_V \left(\nabla \frac{k}{\mu} \nabla p \right) dV + \int_V \hat{q} dV - \phi c_t \frac{\partial}{\partial t} \int_V p dV = 0$$

and by applying the divergence theorem to relate a volume integral to a surface integral then the final form is shown below

$$\int_S \left(\frac{k}{\mu} \nabla p \right) \vec{n} dS + q = \phi c_t V \frac{\partial \bar{p}}{\partial t}$$

where \bar{p} is an average pressure taken over the control volume and \vec{n} is the normal vector pointing out on the surface plane. Numerically, the surface integral will boil down to a summation over the facets of the control volume.

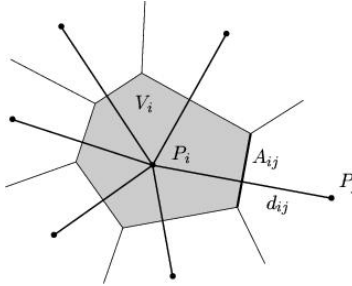


Figure 35: Voronoi grid with control volume³⁴

The figure above shows such a hexagonal Voronoi grid with the control volume. The variables (e.g. pressure) are being calculated as averages across the control volumes. The finite volume method is widely used in reservoir simulation in conjunction with so-called PEBI (or Voronoi) grids, which are hexagonal grids, because these can represent complex geometries, as well as have an improved stencil over e.g. the FD 5-point stencil. Nevertheless, the FV method is not restricted to unstructured grids only, but can be also applied to Cartesian grids. The strengths of the finite volume method lie in the fact that complex geometries can be represented and that the FV method is a conservative numer-

ical method (i.e. whatever flux enters the volume also has to leave it somewhere else). A problem with the FV method is the computation of variable values on the interfaces of such control volumes and the subsequent upstream weighting. During simulation runs, the CFL time-stepping criterion needs to be accounted for numerical stability reasons.

Finite Element Method

The finite element method (FEM) has been long known and used in solving differential equations in the fields of aeronautical and mechanical engineering. Only recently, however, has this powerful technique been applied to reservoir engineering and simulation of fluid fluid within both fractured and unfractured porous media. Similar to the finite volume technique the FEM uses the integral form of the governing PDE. The difference between these methods is that the FEM introduces weighting functions to the integral form and the whole example boils down to a minimization problem. In order to do this the domain over which we wish to compute a variable is being subdivided into so-called finite elements.

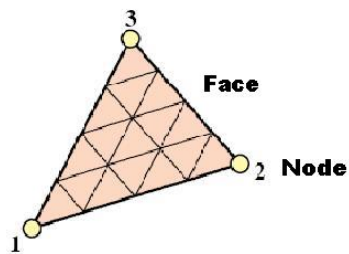


Figure 36: Triangle finite element

Fig. 4 shows a triangular finite element with the three nodes and the faces. This element form can only be applied for 2D problems. The value of the property within the element can be easily related to nodal property values. In its present form the finite element is very similar to a ternary plot in chemistry. The property (i.e. pressure) of the entire element is related to the nodal property through a linear combination as

$$\hat{p}(x, t) = \sum_{i=1}^n p_i(t) \Phi_i(x)$$

where p is the pressure at the node and \hat{p} the pressure of the entire element, and Φ are the basis (or shape) functions. Notice that the important fact of the above applied equation is the fact that the nodal pressures are just functions of time, while the basis functions are functions of position. The basis functions can be linear, quadratic, cubic etc. However, in our example the basis functions are linearly varying between the nodes with the following condition

$$\Phi_i = \begin{cases} 1 & \text{at } i \\ 0 & \text{else} \end{cases}$$

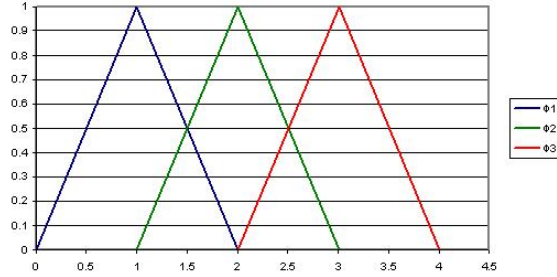


Figure 37: Linear FE basis functions

The figure above shows the linear finite element basis functions. The linear basis functions themselves can be evaluated through an easy geometrical relationship, which boils down to the equation of a plane

$$\Phi_i = a_i x + b_i y + c_i$$

where a_i , b_i , c_i are constant values that are different of every node, but can be calculated with the above condition of linear variability. The x and y refers to the coordinate position. If we assume a spacial differential operator L of the following form

$$L(\hat{p}) = \nabla \frac{k}{\mu} \nabla \hat{p} + \hat{q} - \phi c_t \frac{\partial \hat{p}}{\partial t}$$

then the FEM approximation to the solution of pressure is obtained through the following expression

$$\int_V L(\hat{p}) \Phi_i dV \rightarrow \min$$

which is a minimization problem. In the ideal case the above expression would equal zero.

Combined Element Volume Method

The combined element volume method (CEVM) refers to a combination of finite element and finite volume methods to solve the governing equations of fluid flow in porous media. The character of the pressure and the transport equations is completely different. The pressure equation is a non-linear diffusion equation

and of parabolic type (similar to heat conduction equation). The saturation (transport equation) is of hyperbolic character. A rigid discussion of numerical methods within CSP is presented in Geiger et al. [2003].³⁵ This section closely follows the refered publication.

By combining the individual phase conservation laws with Darcy's law we get the pressure equation

$$\phi c_t \frac{\partial p}{\partial t} = \nabla \cdot [k \lambda_t \nabla p] + \nabla \cdot [\bar{g} k (\lambda_n \rho_n + \lambda_w \rho_w)] + \hat{q}_t \quad (5.3)$$

where n, w , denote non-wetting and wetting respectively. In this formulation the pressure is the wetting phase pressure. Other variables are the same as defined in the nomenclature. Eq.5.3 is a simplified version of Eq.5.1. In the equation above capillary effects are neglected, because they are assumed to be insignificantly small when compared to the fluid pressure gradient on the reservoir scale. Eq.5.3 is solved by using the FEM approximation to the solution as presented on the previous page on a computational domain Ω to obtain

$$\int_{\Omega} \phi c_t \frac{\partial p}{\partial t} \Phi_i dx = \int_{\Omega} \nabla \cdot [k \lambda_t \nabla p] \Phi_i dx + \int_{\Omega} \nabla \cdot [\bar{g} k (\lambda_n \rho_n + \lambda_w \rho_w)] \Phi_i dx + \int_{\Omega} \hat{q}_t \Phi_i dx \quad (5.4)$$

If we apply the rule as given by integration by parts for higher dimensions we can simplify the right-hand side of Eq. 5.4. We obtain two parts: the first term is an integral over the boundary $\partial\Omega$ and the second term is an integral over the domain Ω . Using the weak formulation the integral involving the boundary is neglected and only the integral over the domain is accounted for to obtain

$$\int_{\Omega} \phi c_t \frac{\partial p}{\partial t} \Phi_i dx = - \int_{\Omega} k \lambda_t \nabla p \cdot \nabla \Phi_i dx - \int_{\Omega} \bar{g} k (\lambda_n \rho_n + \lambda_w \rho_w) \cdot \nabla \Phi_i dx + \int_{\Omega} \hat{q}_t \Phi_i dx \quad (5.5)$$

Notice that by this mathematical "trick" it was possible to eliminate the del operator. The next condition is that we specify the pressure as a linear combination of node pressures and a basis function as

$$p(x, t) = \sum_{j=1}^n p_j(t) \Phi_j(x) \quad (5.6)$$

where n is the number of nodes at which the pressure is evaluated. The idea

here is to decouple the pressure functionality from position, therefore pressure is just a function of time. This is very similar to the separation of variables principle used in solving ordinary (and partial) differential equations. As a consequence applying a divergence to these individual node pressures would yield zero. If we insert Eq.5.6 into Eq.5.5 and apply the product rule then we get the following expression, which is a system of coupled ordinary differential equations

$$\sum_{j=1}^n \frac{dp_j}{dt}(t) A_{ij}(t) = - \sum_{j=1}^n p_j(t) K_{ij}(t) + q_i(t) \quad (5.7)$$

where

$$A_{ij}(t) = \int_{\Omega} \phi c_t \Phi_i \Phi_j dx$$

$$K_{ij}(t) = \int_{\Omega} k \lambda_t \nabla \Phi_j \nabla \Phi_i dx$$

and

$$q_i(t) = - \int_{\Omega} \vec{g}^k (\lambda_n \rho_n + \lambda_w \rho_w) \cdot \nabla \Phi_i dx + \int_{\Omega} \hat{q}_t \Phi_i dx$$

A_{ij} and K_{ij} are coefficient matrices that change over time. These matrices are sparse and contain non-zero values along the main dia The term q_i can be viewed as an additional term comprised of a source/sink and a gravity flow part. It will later be added to the right-hand side of the equation. Given a time step Δt and a superscript k that denotes the current (known) time, Eq.5.7 can be discretized using the implicit backward Euler time scheme to obtain

$$\sum_{j=1}^n \frac{p_j^{k+1}(t) - p_j^k(t)}{\Delta t} A_{ij}^k(t) = - \sum_{j=1}^n p_j^{k+1}(t) K_{ij}^k(t) + q_i(t)$$

and finally

$$\sum_{j=1}^n (A_{ij}^k + \Delta t K_{ij}^k) p_j^{k+1} = \sum_{j=1}^n A_{ij}^k p_j^k + \Delta t q_i^k \quad (5.8)$$

which basically is an equation system of the type $Ax = b$. The variable we are solving for is the pressure vector at time level $k + 1$. Notice that the

coefficient matrices have the superscript k and are therefore lagging behind one iteration. By assuming that their values change negligibly small over time this is a sufficiently accurate simplification. The implicit Euler time discretization scheme has the advantage that it does not require to fulfill the CFL-criterion, therefore the time steps can be larger. Eq.5.8, which yields the nodal pressures, can accurately be solved with algebraic multigrid methods.³¹ The next step in CSP is the construction of a finite volume subgrid that is barycentrically centered around the nodes. This finite volume is subsequently a polygon (in the case of triangular finite elements), whose edges are the barycenters of the finite elements around the central node.

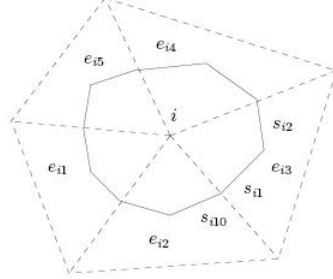


Figure 38: Barycentric finite volumes³⁸

In the figure above i denotes the node, e denotes the finite elements, while s denotes the segments of the finite volume. After the pressure equation has been solved the total velocity (i.e. sum of wetting and non-wetting velocities) can be easily calculated for the nodes with

$$\vec{v}_t = -k\lambda_t \nabla p \quad (5.9)$$

where k is the permeability tensor, and λ_t is the total mobility (i.e. sum of individual phase mobilities). Notice that the total velocity is a vector property, pointing into a certain direction. The individual phase velocities (e.g. for the non-wetting phase) can be determined by

$$\vec{v}_n = \frac{1}{1 + \lambda_w/\lambda_n} [\vec{v}_t - k\lambda_n (\rho_w - \rho_n) \vec{g}]$$

and by making use of Eq.5.9 and the fact that the wetting-phase velocity is the difference between total and non-wetting phase velocity. The velocity evaluated above is an element vector property. Velocities are piecewise constant and discontinuous across FE faces. After having calculated those properties the transport (or saturation) equation needs to be solved. The saturation equation is a non-linear advection equation and of hyperbolic character. After mathematical manipulations it has the following form in terms of non-wetting phase

$$\phi \frac{\partial S_n}{\partial t} = -\nabla [f_n \vec{v}_t] + \nabla [\bar{\lambda} k (\Delta \rho \vec{g} + \nabla P_c)] + \hat{q}_n \quad (5.10)$$

where f is the fractional flow, $\bar{\lambda}$ a type of average total mobility (see section 5.3), and $\Delta \rho$ is the difference between wetting and non-wetting phase densities.

The finite volume method makes use of both the integral form of the saturation equation, as well as the Gauss's divergence theorem, that converts a volumete integral to a surface integral by also simulataneously eliminating the del operator. Then the following is obtained

$$\int_{V_i} \phi \frac{\partial S_n}{\partial t} dV_i = - \int_{\partial V_i} [f_n \vec{v}_t] \vec{n} dA + \int_{\partial V_i} [\bar{\lambda} k (\Delta \rho \vec{g} + \nabla P_c)] \vec{n} dA + \int_{V_i} \hat{q}_n dV_i \quad (5.11)$$

Using Euler's method for the time discretization we obtain the following (explicit) expression for the future non-wetting phase saturation

$$S_{ni}^{k+1} = S_{ni}^k - \frac{\Delta t}{\phi V_i} \sum_{j=1}^{n_i} [f_{n_j} v_{t_j} - \bar{\lambda}_j k (\Delta \rho_j \vec{g} + \nabla P_{c_j})] n_j A_j - q_{ni} V_i \quad (5.12)$$

where $\sum_{j=1}^{n_i}$ is the summation over all straight line boundary segments j of the finite volume V_i , Δt is the time step, and n_j is the outward normal vector to j th segment, scaled by the lenght of the segment.

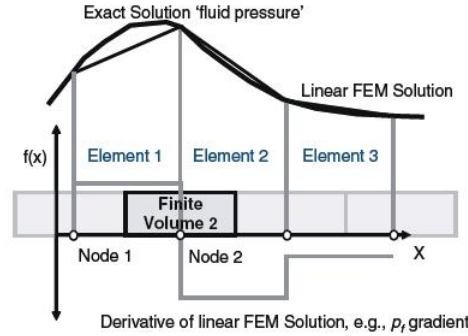


Figure 39: 1D finite-element finite-volume discretisation of a Darcian fluid flow³⁹

The figure above shows a graphical representation of a 1D dual mesh FE-FV discretization of Darcian fluid flow. The exact solution of a PDE (in this case pressure) is given at the top, which is approximation with the help of a linear finite element solution. The pressure varies piecewise linearly between the nodes. This leads to piecewise constant pressure derivatives within the elements, which are discontinuous across element boundaries (i.e. at the nodes). Those mathematical singularities are elegantly circumvented by constructing the finite

volumes around those nodes. By solving the saturation equation with the FV method the pressure derivative as well as the fluxes are evaluated at element centres, where the pressure derivative is not a singularity.

The finite volume method has the advantage of being volume conservative (i.e. whatever flows into the volume has to flow out). However, one main disadvantage is that the time step can only be of a certain size and has to fulfill the Courant-Friedrichs-Lewy (CFL) condition. In addition, in Eq.5.12 certain parameters (e.g. total velocity, non-wetting phase fractional flow etc.) are piecewise constant within the finite volumes, but need to be computed for the interfaces of the FV; calculation of the flux through the facets often causes problems. Therefore an upwinding scheme is necessary that can compute those interface values. The first-order upwinding scheme is the so-called upstream weighting. CSP uses higher-order (2nd order) upwind schemes and slope limiters that should prevent spurious oscillations associated with second-order schemes. For details the interested reader is referred to Geiger et al. [2003].³⁵

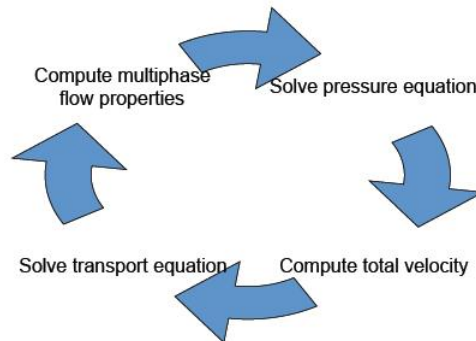


Figure 40: Numerical solution procedure

Fig.7 presents a graphical representation of the numerical solution procedure as employed by CSMP++. During every time loop first the pressure equation is solved with the help of the FE method. Next the obtained pressure field is used to compute the total velocity with the Darcy equation. Later the transport (or saturation) equation is solved with help of the FV method and phase saturations are obtained. These are then used to update the multiphase (saturation-dependent) fluid properties such as capillary pressure or relative permeability curves among others. Then the next time loop performs the same steps.

Modelling and Workflow

Introduction

Complex Systems Modelling Platform is a very flexible software that can make use of various types of input data. One very simple method is the use of 8-bit colour-coded bitmap images that represent the geological cross-section. Every colour on the 256-value scheme is related to permeability values from 10^{-21} to 10^{-12} square-meters. Internally, CSP creates a regular two-dimensional rectangular model with triangular finite elements to solve the governing partial differential equations. Another more sophisticated method to create geological cross-sections is via the use of computer-aided design (CAD) software, which facilitates the design of realistic two- or three-dimensional geological models. The CAD model needs to be meshed with other meshing software before CSP can perform the simulation. This section will deal with the steps necessary to build the model, mesh the model, perform the simulation and output the results. It will only deal with the work related to the simulation in this thesis. A good reference is the CSP Model Building & Interface Guide.³⁷

Geological Modelling

Modelling of the geological features such as fractures, layers and boundaries is done with the help of Rhinoceros (McNeel & Associates). Rhinoceros is a computer-aided design (CAD) software used in various disciplines, from construction to engineering and design applications. Rhino's fundamental objects are points, NURBS (Non-Uniform Rational B-Splines) curves, surfaces and solids. It greatly facilitates the design of objects with various design commands and perspective viewports.

The model used in this simulation comes from an outcrop analysis. The first step of the modelling is the definition of relative and absolute tolerances as well as angle tolerance in the model. These specified tolerance values obviously give a default of the model size and resolution of smallest objects. The next step is importing or setting of the outcrop picture (as pdf- or- bitmap- file) as a background to the Rhino viewport. When dealing with vertical geological cross-sections it is necessary to draw on the xy-plane in Rhino because in CSP the positive y-axis is pointing upwards. In 2D a control rectangular surface needs to be created, which will represent the model domain. After splitting the rectangular domain into four lines, these need to be named RIGHT, TOP, LEFT,

and BOTTOM in a counter-clockwise fashion. For the simulation purpose those lines will represent the boundaries upon which boundary and essential conditions can be imposed. The next step is the drawing of the geological model by copying the background picture of the outcrop and using the NURBS curves to represent geological layer boundaries and fractures. The surface needs to be cut according to geological features. Entities (e.g. layers, fractures etc.) need to be organised into families (e.g. layerA, fracturesA etc.). In Rhino this can be easily done by organising objects within layers, which can then be easily manipulated. It also becomes easier to keep track of numerous entities when they are situated on the same layer. Ideally all objects within a layer in Rhino should have the same properties (e.g. permeability, porosity etc.). Later, for simulation purposes, parameters can be set for those Rhinoceros layers. CSP also gives the possibility of individually accessing objects of a particular layer. At a final step before going to the meshing software intersecting curves need to be split. This is necessary so the meshing software can work more efficiently and more sensible finite elements can be created that follow the geology more accurately and produce a more realistic model.

NURBS curves have been in use for several decades in computer-aided design, manufacturing and engineering disciplines. Their strenghts are an accurate graphical modelling of curves, both analytical (e.g. circles, ellipse etc.) and free-form (e.g. cars, airplanes etc.), as well as a profound mathematical background. NURBS curves are specified through the degree, control points, basis functions, weights and knot vectors. They are a more generalised form of B-spline curves. A p^{th} -degree B-spline curve $C(u)$ is a piecewise polynomial function defined as following

$$C(u) = \sum_{i=0}^n N_{i,p}(u)P_i$$

where P_i are the control points, $N_{i,p}$ are the basis functions, and n is the number of control points minus one. A major difference between the B-spline curve and the NURBS curve are the so-called weights that are inherent. Therefore the definition of the NURBS curve is given by

$$C(u) = \frac{\sum_{i=0}^n N_{i,p}(u)w_iP_i}{\sum_{i=0}^n N_{i,p}(u)w_i}$$

where w_i denotes the weight of control point P_i . Weights are usually positive numbers. The term in the denominator is a normalizing factor. Control points

are needed for the computation of the NURBS curve and they can be viewed as restrictions of curve geometry. A simple way of changing the shape of the NURBS curve is by changing the position of the control points. If all control points have the same weight, then the curve is said to be non-rational, otherwise it is rational. Although in reality NURBS have the possibility of being either rational or non-rational, most of them will be non-rational. The degree of the NURBS curve can be any positive whole number, although degrees 1, 2, 3 or 5 are most common. Additionally, a knot vector, which specifies the parameter intervals over which individual curves are combined to form a B-spline, is needed to display the curve. The i -th basis function of degree p is defined recursively according to

$$N_{i,0}(u) = 1 \quad \text{if } u_i \leq u \leq u_{i+1}, 0 \text{ else}$$

$$N_{i,p}(u) = \frac{u - u_i}{u_{i+p} - u_i} N_{i,p-1}(u) + \frac{u_{i+p+1} - u}{u_{i+p+1} - u_{i+1}} N_{i+1,p-1}(u)$$

where $N_{i,0}(u)$ is a step function equal to one only within the interval $[u_i, u_{i+1}]$ and zero elsewhere. Similarly from curves also NURBS surfaces can be extracted. However, this is computer memory expensive and not necessary for two-dimensional examples. NURBS surfaces only come into importance when modelling geometry in a 3D domain.

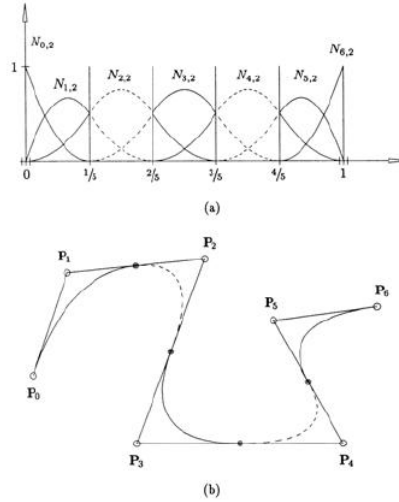


Figure 41: Quadratic B-spline basis functions (a) NURBS curve (b)³⁷

The figure above shows quadratic B-spline basis functions and their respective intervals. Moreover, the NURBS curve as well as the control points are also being displayed below. The shape of the curve is determined by the position of the control points, the weights and the degree of the basis functions.

To sum up, NURBS curves are an excellent tool of modelling complex geology and various other free-forms both accurately, as well as on a solid mathematical basis. NURBS curves are continuous and differentiable everywhere, except on the knots.

Meshing

Before we can import the geometry from Rhinoceros to mesh it in the meshing software, it needs to be converted to a readable format. This is done using Tetin, an executable programme and preprocessor of the ICEM CFD mesh generator. Meshing the geometry is done with ANSYS ICEM CFD 11.0. ANSYS ICEM CFD is a commercial meshing software, that guides the user through the required tasks in a step-by-step fashion. ANSYS ICEM CFD can work with a variety of complex free-form geometries including NURBS among others. Other strengths of the software include the robust meshing algorithms used, availability of various different types of meshes (e.g. triangles, quadrilaterals etc. for

2D; tetrahedra, hexahedra etc. for 3D).

The first task is to create points, wherever two curves intersect or touch. This is done to enable an efficient and accurate mesh, and to prohibit meshing errors such as holes, missing internal faces or negative volumes. It is also very important that two points are not very close to each other, because this could lead to some weird elements with unfavourable aspect ratios. ANSYS then requires global scaling factors and local scaling factors that determine the maximum size of the elements within a group. Other parameters that need to be specified are the mesh type and method, as well as surface and curve mesh setup parameters. Then the mesh, which in our example consists of triangles, is computed. Unfortunately, in some case the mesh will be unsatisfactorily for export to CSMP. Errors include holes, uncovered and missing faces, or duplicate elements. A useful tool is to visually examine the generated mesh and to colour the mesh according to quality. Usually, lower-quality elements are found at interfaces of groups or boundaries, and fracture tips. ANSYS also has an automatic mesh check and repair command, which increases the mesh quality. After all those tasks are done and the mesh has a high quality, the results need to be output to CSP.

ANSYS has the option of exporting the mesh directly to CSP. It produces two files, which have the model name and the extensions of *.asc and *.dat. The asc-file can be opened with a text programme and contains the individual information about the regions and the mesh element types, as well as the number of elements. Every finite element has a individual numbering and an element type (e.g. bar, triangle etc.). The dat-file cannot be opened with a text programme, but it contains information about the connectivity of the elements. This is necessary for setting up the basis functions, for integration and solving the differential equations.

Setup of Configuration and Regions Files

The next step in the simulation process is the setup of the configuration file. The configuration files must have the model name and the extension “-configuration.txt”.

The general style of the configuration files is the following: First the global material properties are set, which are valid for the entire model. They include information about model properties like permeability, porosity, fluid viscosity and initial saturation as well as relative permeability model among others. The next portion of the file specifies local material properties, which are valid only for

the region in the model. Those local properties can be assigned to the subregion boundary, interior or the complete subregion. Local properties do not need to be defined if they have the same value as the default (global) properties. The next section defines the essential conditions on model boundaries. These can either be Dirichlet or Neumann boundary conditions are necessary to have an unique solution to the differential equations. In the gravity-drainage example a gas injection rate and saturation is defined to the top of the model. Permeability of the top and bottom most triangle elements can also be specified, in order to mimic the behaviour of the horizontal injection and production wells. For a 2D model two numerical values are needed for the essential boundary conditions, which denote maximum and minimum values. Usually these two values will be equal; if not CSP assumes a linear variation between those two values along the boundary. The last blocks of the configuration file are essential flags and the computational settings. The computational settings first define the time stepping algorithm (i.e. conservative, daring, aggressive etc.) and the duration of the simulation, as well as the output time of the results.

Whenever CSP reads the configuration file it automatically checks the values for the properties and whether those properties do exist. If a value range is exceeded, the variable from the configuration file will be set to the nearest range specified in a file called "CSP-2phase-variables.txt". This is useful in order to quickly detect typos or unphysical property values.

Another file necessary for the simulation has the model name and the extension "-regions.txt". It specifies which regions of the model are used. Other discretized regions in the *.asc-file are ignored. A regions-file is only necessary for models built within ANSYS ICEM. After finishing the configuration and regions files the simulation can be started by clicking on the CSP executable programme, which produces the data output.

Data Output

Data output in CSP can be defined within the source code, prior to producing the executable programme. It can be done either through the VTK or the JPEG interfaces. In this thesis properties like absolute fluid pressure, gas saturation and total mobility among others were observed and output via the VTK interface. During the simulation CSP constantly monitors the defined properties for the output times as specified within the configurations file. These data set are recorded in *.vtk files that can easily be visualized through the MayaVi software (mayavi.sourceforge.net) or ParaView software (www.paraview.org). Both

provide the user with various data analysis options like histograms, plots or calculators. Apart from that CSMP++ records certain properties in text file format with the extensions “-monitored_regions.txt”, “-flow&ranges.txt” and “-saturation_gas.txt”.

The only setback is that the VTK format does not support the display of scalar element properties. Therefore CSP outputs the element properties as point data to VTK. These can be connected via a Delauney triangulation if a continuous field is to be displayed. Unfortunately, material boundaries will be blurred through this approach. Vector quantities like fluid velocities can be displayed with so-called glyphs.²⁹

Reservoir Case Study

Continuous Fracture

Before actually performing the gravity-drainage simulation on an actual model, I decided to perform some preliminary simulations in order to check, whether the software gives realistic results. In the first example I wanted to perform a basic simulation of gravity-drainage.

The quadratic model has a height and width of 100 ft (30.48m). It is divided into two equal regions called toplayer and bottomlayer. Both layers have the same properties, with the exception that the toplayer has a lower permeability than the bottomlayer. Running vertically all the way to the bottom is a fracture that has a width of 1cm, a porosity of 1 and a permeability of 10^{-11} m² (10 000 md). The fracture is located exactly at the middle of the model. Due to the relatively narrow fracture, the fracture cannot be seen on the plot, which displays the permeability below.

Into this model gas is injected at the top through a horizontal injector well and produced exactly at the bottom through a horizontal well. At the top of the model the nodal fluid volume source (i.e. injection rate) and the oil and gas saturations are specified, while at the bottom only the pressure is fixed (i.e. constant pressure boundary) at $3.44738 \cdot 10^7$ Pa (5000 psi). The left and right boundaries are no flow boundaries. Table 10 gives a summary of the material properties and the initial conditions used in the default simulation.

For the fracture a linear Brooks-Corey relative model was used. A note on the top boundary condition: For a gravity drainage process another boundary condition could be to set the pressure constant at the top. The only prerequisite is to have such a high top boundary pressure as to make sure that the gas enters

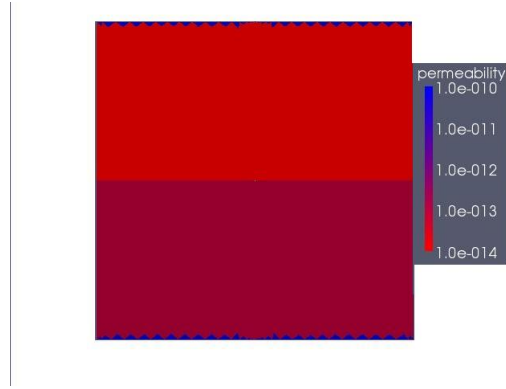


Figure 42: Permeability of continuous fracture model

the fracture.

Parameter	Value
X dimension	30.48 m
Y dimension	30.48 m
Porosity	0.25
Oil density	1000 kg/m ³
Gas density	100 kg/m ³
Oil viscosity	10 ⁻³ Pa.s
Gas viscosity	10 ⁻⁵ Pa.s
Total compressibility	10 ⁻⁷ Pa ⁻¹
Brooks Corey Parameter	2.0
Well permeabilities	10 ⁻¹⁰ m ²
Toplayer permeability	10 ⁻¹⁴ m ²
Bottomlayer permeability	10 ⁻¹³ m ²
Fracture permeability	10 ⁻¹¹ m ²
Fracture porosity	1.0
Fracture aperture	0.01 m
Nodal fluid volume source	2.1505*10 ⁻⁷ m ³ /(m.s)
Initial oil saturation	0.95
Initial gas saturation	0.05

Table 10: Material properties for default simulation

If we plot the saturation over time, we obtain the following figures.

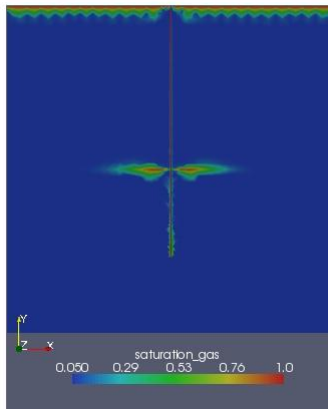


Figure 43: Gas saturation of continuous fracture model after 2.5 days

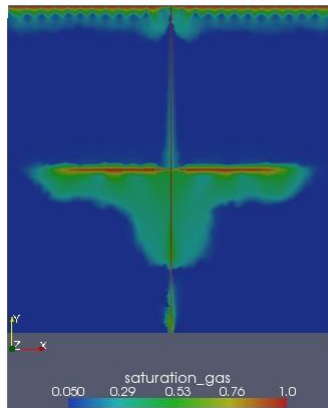


Figure 44: Gas saturation of continuous fracture model after 13.9 days

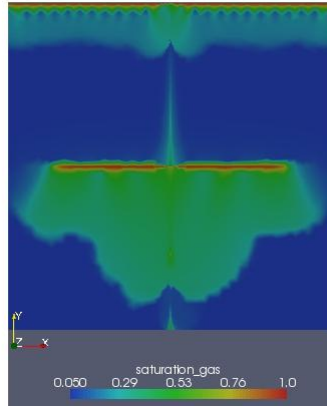


Figure 45: Gas saturation of continuous fracture model after 27.8 days

From those figures above we can see the changes in gas saturation over time. In our drainage processes we are trying to increase the gas saturation as much as possible to recover a higher amount of oil. Oil saturation is one minus the gas saturation. Gas enters the system at the top boundary, but has no chance to enter at the toplayer first. The reason for this is the relatively low permeability of 10 md. Therefore the gas preferentially floods the high-permeability fracture and is being transported down to the bottomlayer. After reaching a threshold height the gas first enters in the bottomlayer and starts to displace the oil. By doing so, the gas also increases the total mobility of the pore fluids which in turn also enhances the drainage process.

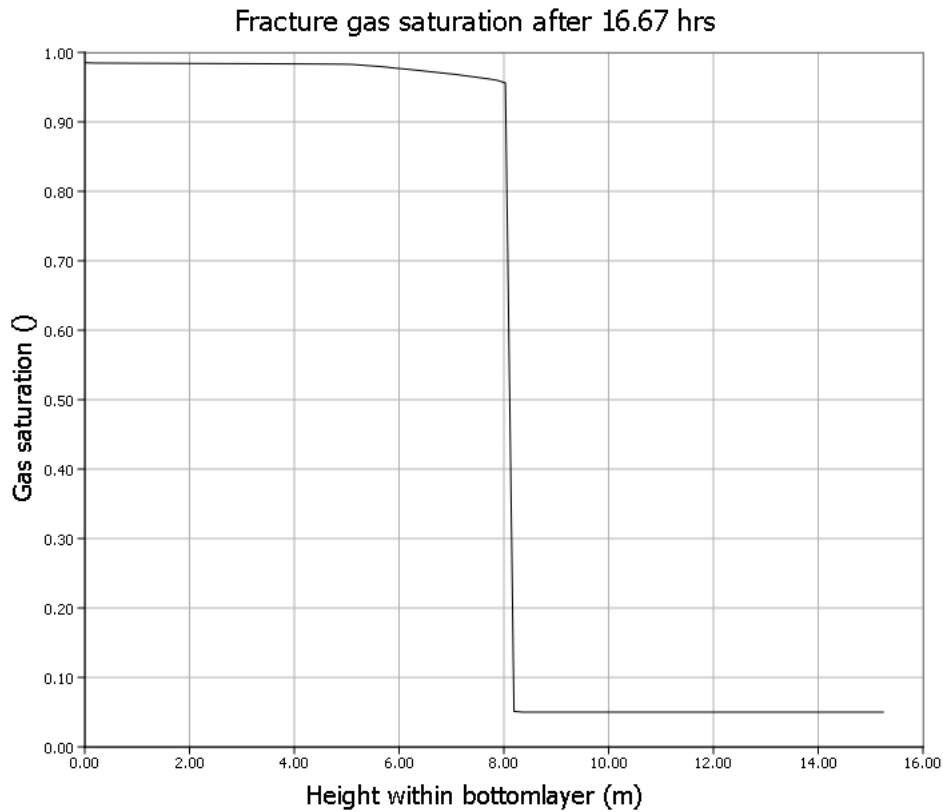


Figure 46: Bottomlayer fracture gas saturation after 16.67 hrs

The picture above shows that gas starts to enter the bottomlayer after about 16 hours and after reaching a threshold height of about 8.5 meters. The displacement front in the bottomlayer has a mushroom profile. After some time the drainage process also begins in the toplayer. Here, however, the displacement front does not have this mushroom shape but is horizontally constant (i.e. piston-like). Another observation that I make is that on the interface between the toplayer and the bottomlayer a highly gas-saturated region develops, which however does not extend to the left or right model boundary. The drainage efficiency is better within the higher permeable layer. Obviously the fracture enhances the transport of the gas to the advantageous (high-permeable) regions and acts like an accelerator to the drainage process.

The figure above shows the integrated gas saturation (i.e. gas volume in

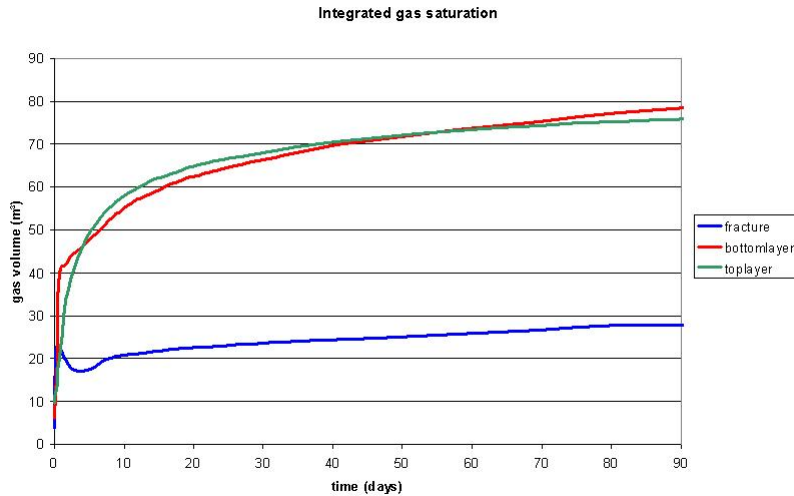


Figure 47: Integrated gas saturation over time

cubic meters) over time for the perspective regions. The gas volume within the fracture first increases and after reaching an apex decreases and forms a trough and finally stabilizes for a constant value. My explanation for this would be that due to the injection the gas volume increases in the fracture. The trough then appears after gas has started to flow into the bottomlayer. Finally, there is a stabilization of gas present in the fracture. For small times in the beginning of the simulation the bottomlayer has more gas present than the toplayer. The reason for this is the fact that we are injecting gas directly from the top of the model and gas preferentially enters in the bottomlayer first. Then for about 45 days of the simulation it is true that more gas is present in the toplayer, however for later times of the simulation more gas is present in the bottomlayer. From this observation I can make the assumption that for early times the oil displacement seems to be better in the toplayer. Probably, this is due to the gas entering more uniformly, whereas in the bottomlayer the gas enters in a bubble- or mushroom-like form. However, on the long term the displacement efficiency is better for the bottomlayer, which seems to be natural due to the higher layer permeability.

A note on symmetry: If we cut the model vertically along the fracture, the left and right sides should be mirror-symmetric. Due to different meshes on left and right sides this symmetry does not appear in the pictures.

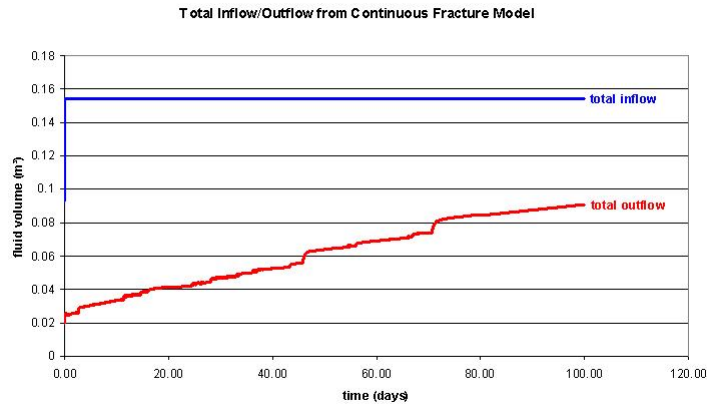


Figure 48: Inflow and outflow over time for continuous fracture model

The figure above presents the total fluid inflow and outflow of the model. This can be thought of as injection and production rates. The inflow stays constant, which is not surprising because we fixed the injection rate on the top. The outflow which is mainly oil is increasing over time. The numerical value of the inflow is different to the nodal fluid volume source because the nodal fluid volume source is only the gas fluid volume injected for each node and normalized per 1 meter, while the inflow itself gives the total fluid amount injected at the top. Another observation that can be made is that the volume of fluid injected is larger than the volume of fluid produced. This happens because we have a slightly compressible model with gas being more compressible than oil. For incompressible fluids injection and production rates would be equal.

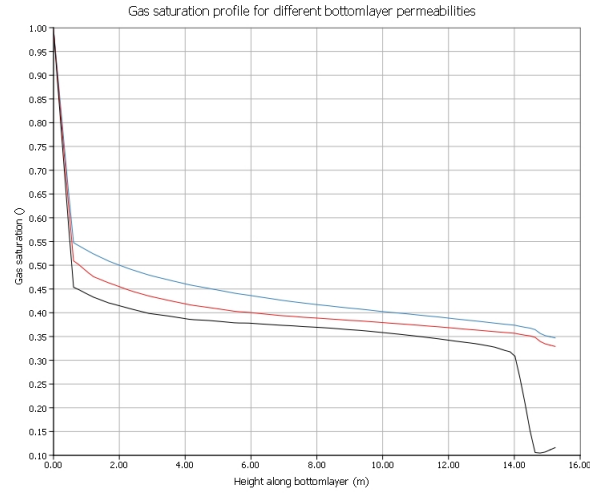


Figure 49: Effect of bottomlayer permeability (100 md,200 md,500 md) on gas saturation after 13.89 hrs

The figure above shows the vertical gas saturation profiles for different bottomlayer permeabilities after about 13.89 hours. The toplayer properties have not been changed. The profile is drawn in ParaView software between points (2,0,0) and (2,-15.24,0). The different lines represent bottomlayer permeabilities of 100md, 200md and 500md. We can see that the higher the bottomlayer permeability the better and more efficient is the gas-oil gravity drainage process (i.e. more oil can be recovered).

The bottomlayer permeability also has an effect on the threshold height that needs to be build up before gas can enter the bottomlayer. Usually the higher the permeability the lower is the gas threshold height and the more easy can the gas enter the formation. This behaviour is shown in the figure below. It shows the gas saturation profile within the fracture in the bottomlayer. For the blue line (permeability of 500 md) the threshold height is about 8.2 meters, while it is higher at about 8.4 meters for the black line (100 md) and for the red line (200 md). The difference in threshold height between the 100 md and the 200 md case can barely be seen with the naked eye but also confirms that higher permeability decreases the threshold height. This observation has been made already in earlier research.⁴⁰

I also changed the nodal fluid volume source from $2.1505 \cdot 10^{-5}$ to $2.1505 \cdot 10^{-11} \text{ m}^3/\text{ms}$ to see whether it in anyway affected the saturation profile. I was surprised to see that obviously the nodal fluid volume source does not affect the

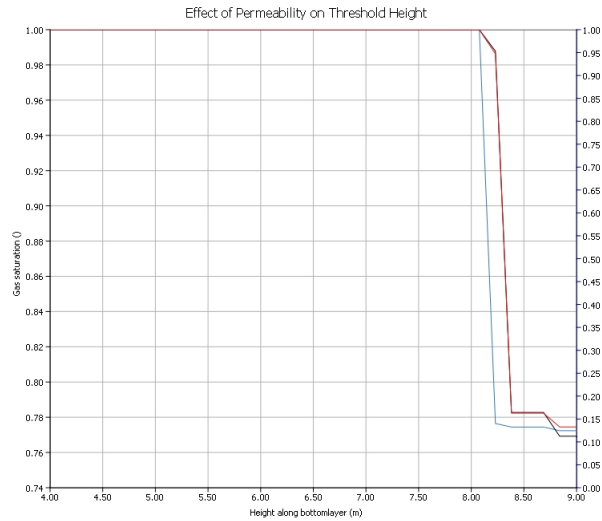


Figure 50: Effect of bottomlayer permeability (100md, 200md, 500md) on threshold height

outcome in any way.

From previous research⁴⁰ on gas-oil gravity drainage it is known that the density contrast between oil and gas plays an important role in determining drainage efficiencies. I tried to confirm this observation by performing simulations with changes in the oil densities. The gas density was left unchanged at 100 kg/m³, while the oil density was set to 800 kg/m³, 900 kg/m³, 1000 kg/m³ and 1100 kg/m³. The figure below shows the gas saturation on the vertical line from (2,15.24,0) to (2,-15.24,0) at the end of the simulation run for about 92 days. We can see that the higher the density contrast between wetting and non-wetting phase the higher is the gas saturation and therefore the better is the drainage performance. A denser oil has a larger weight and therefore is more easily drainage out of the model. If we observe the figure below we can see that the density contrast plays a negligible role exactly on the top of the model and on the interface between toplayer and bottomlayer.

Another simulation was performed to observe the effect of the oil viscosity on the gravity drainage. The oil viscosity was changed from 1.2*10⁻³ to 10⁻³ and 10⁻⁴Pas. It was found that an increased oil viscosity has a negative effect on the drainage efficiency. The less viscous the oil the higher recoveries can be expected. Especially within the toplayer the effect of increased oil viscosities can be observed and is significant. The lower the oil viscosity the faster is

the toplayer drained. For the bottomlayer, however, the gas enters to form a mushroom-like profile which is quickly changed to a cone or pyramid-like gas profile. My suggestion is that the high permeable layer combined with a low viscous oil leads to this phenomenon. Apparently, a lower viscosity oil is better drained from a reservoir that has lower permeability. The figure below shows the gas saturation profile across the vertical line from (2,15.24,0) to (2,-15.24,0). It confirms the observation made above. On the next page also the gas saturation histograms are presented for oil viscosity values mentioned above. We can also clearly see that the lower viscous oil shifts the gas saturation histogram values to the right (advantageous conditions).

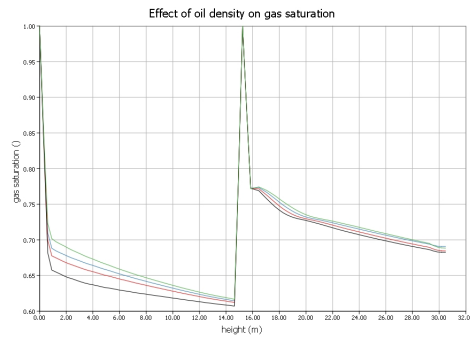


Figure 51: Effect of oil density on gas saturation

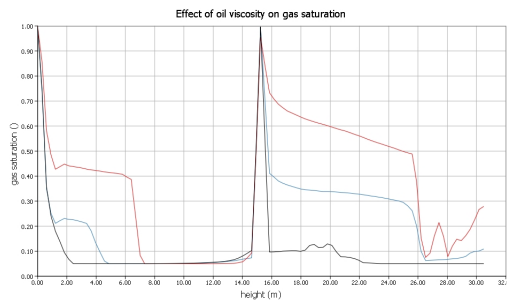


Figure 52: Effect of oil viscosity on gas saturation

To sum up, those performed simulations have confirmed the validity and correctness of the 2D reservoir simulator executable program for the gas-oil gravity drainage example.

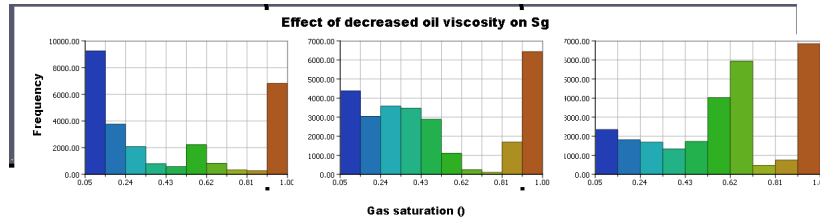


Figure 53: Gas saturation histogram for different oil viscosities

Discontinuous Fracture

As we have already seen the 2D reservoir simulator already gives satisfying results for the continuous fracture model. However, in the next step I wanted to perform exactly the same simulations with the same initial and boundary conditions on a model that has a fracture that is not running continuously through the toplayer and the bottomlayer. In this model, which I call discontinuous fracture model, the fracture is running vertically through the toplayer and the bottomlayer. It, however, ends and starts 2 meters before the TOP and the BOTTOM boundaries. Therefore the fracture has a length of 26.48 m and a width of 1 cm. The initial default simulation properties are presented in Table 1. A conceptual picture of the model is presented below (dimensions not to scale).

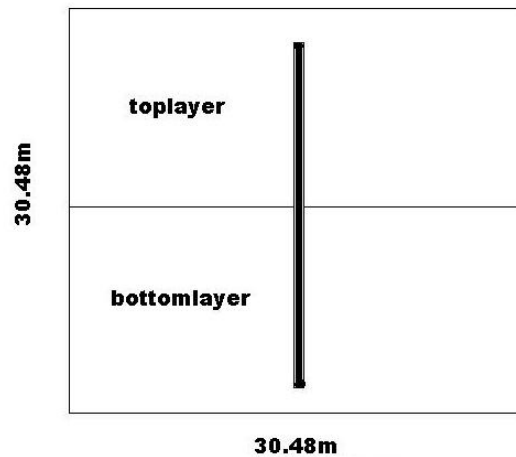


Figure 54: Conceptual picture of discontinuous fracture model

If we plot the gas saturation for different time steps we get the following plots.

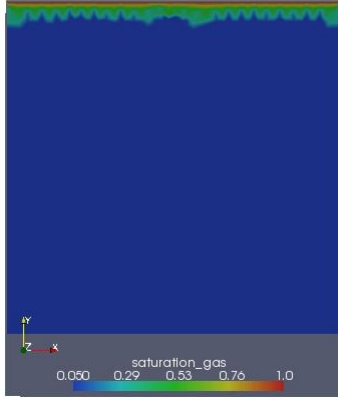


Figure 55: Gas saturation of discontinuous fracture model after 2.5 days

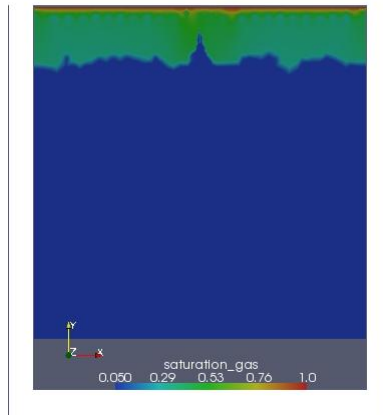


Figure 56: Gas saturation of discontinuous fracture model after 13.9 days

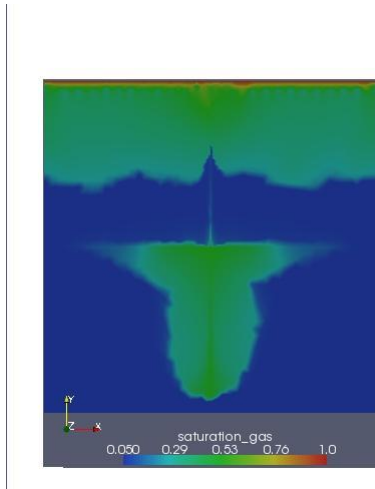


Figure 57: Gas saturation of discontinuous fracture model after 27.8 days

Those gas saturation plots clearly indicate that first the gas enters in the toplayer and has no access to the fracture. Even after about 13.9 days of injection the gas has not yet reached the fracture. Gas reaches the fracture after approximately 20 days and quickly is transported towards the bottomlayer. Due to the high permeability the gas enters the bottomlayer region. One interesting observation, however, is that the created saturation profile within the bottomlayer changes during the simulation. In the beginning it has an upside-down pyramid shape, which then changes to conical and finally pyramid shape.

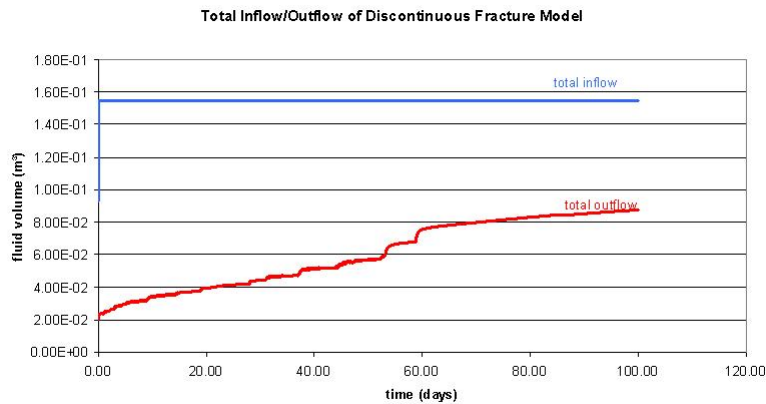


Figure 58: Inflow and outflow over time for discontinuous fracture model

Appendix C

The Dual-Continuum Model

The principles of the dual-continuum model were formulated by Barenblatt et al.[1960], who recognized that infiltration theory at that time could not adequately describe flow in porous media, that was fractured to some degree. By simplifying the problem and making certain assumptions he was able to derive an equation for the fluid pressure within the fractures. Therefore the equations for a porous media with double-porosity are derived. The difference between the dual-continuum model and previous models is the introduction of two pressures (i.e. for fracture and for matrix) for each point in space. Continuum models by definition assume the existence of a representative elementary volume (REV), the smallest volume over which a certain parameter will become a representative value for the whole model. Therefore the REV concept ensures that mean properties (i.e. permeability, porosity etc.) can be used.

Several important characteristics of naturally fractured reservoirs can be captured with the use of a dual-continuum model:⁴³

- Higher permeability as obtained from core measurements.
- Early breakthrough of injection fluids
- Flow predominantly comes from a small portion of the open interval
- Flow experiences a high directionality
- Produced rates are not directly proportional to drawdown

The dual-continuum model can be basically divided into two models: the dual-porosity and the dual-permeability model. Both models have different underlying assumptions and work differently well for certain examples. Whether a dual-porosity or a dual-permeability formulation is preferred for a particular reservoir should be decided individually.

The dual-porosity (also known as the sugar cube) model assumes that the fractures are interconnected and form a continuum. The sugar cubes are thought to represent the matrix blocks. These matrix blocks are not connected to each

other. Therefore, viscous flow can only occur through the fractures and between fractures and matrix but not between matrix blocks themselves. The fluid volume transfer between matrix and fracture is evaluated with the use of transfer functions, which take into account so-called shape factors among others. Its name is derived from the fact that the governing equations have two porosities (i.e. matrix, fracture).

The other model is known as the dual-permeability model. In this case, however, communication between the matrix blocks is allowed. Therefore flow in the dual-permeability model occurs in the fractures, in the matrix blocks themselves and between matrix and fracture. The dual-porosity model can be viewed as a more specialized dual-permeability model, where the flow between matrix blocks equals zero. To sum up, the dual-permeability model is more complicated than the dual-porosity model and therefore used more sheldom in publications and research. Its name is derived from the fact that the governing equations here are mainly based on the two permeabilities (i.e. matrix, fracture). In general, studies and research have shown that for the horizontal cross-section a dual-porosity formulation is applicable, while a dual-permeability formulation is preferred for the vertical cross-section.

The derivation of the dual continuum model is pretty straightforward. By principle the steps presented above in this previous sections of this chapter are followed. The starting point is the continuity equation, which is individually manipulated for the fracture and the matrix regions independently. Those individual portions (i.e. for matrix and fracture systems) can be combined by the introduction of a shape factor. This shape factor's main aim was to model the fluid (and later heat) flow from the matrix to the fracture and vice versa. Warren and Root [1963] formulated the single-phase equations and applied them to pressure transient testing to gain some insights into characteristic behaviour of (dual-porosity) naturally fractured reservoirs. Kazemi et al. [1976] extended those differential equations to immiscible black-oil fluids (i.e. oil and water) and two-phase flow. The extra equations needed for multi-phase conditions are that the sum of all saturations is one and the coupling of wetting and non-wetting phase pressure through the definition of capillary pressure.

The dual-porosity formulation for three-phase flow (oil, water and gas) is presented below. The nomenclature is taken from Kazemi notes.⁴²

$$\nabla (k\phi\lambda_w)_f (\nabla p_{of} - \gamma_w \nabla D - \nabla p_{cwof}) - \tau_w + \hat{q}_{wf} = \quad (5.13)$$

$$\phi_f \left[S_{wf} (c_\phi + c_w)_f \frac{\partial p_{of}}{\partial t} + \frac{\partial S_{wf}}{\partial t} \right]$$

$$\nabla (k\phi\lambda_o)_f (\nabla p_{of} - \gamma_o \nabla D) - \tau_o + \hat{q}_{of} = \quad (5.14)$$

$$\phi_f \left[S_{of} (c_\phi + c_o)_f \frac{\partial p_{of}}{\partial t} + \frac{\partial S_{of}}{\partial t} \right]$$

$$\nabla (k\phi\lambda_g)_f (\nabla p_{of} - \gamma_g \nabla D + \nabla p_{cogf}) - \tau_g + \hat{q}_{gf} = \quad (5.15)$$

$$\phi_f \left[S_{gf} (c_\phi + c_g)_f \frac{\partial p_{gf}}{\partial t} + \frac{\partial S_{gf}}{\partial t} \right]$$

The equations above are the continuity equations for the fracture continuum. The transfer functions for the three phases are presented below

$$\tau_w = \sigma k_m \lambda_{wf/m} (\Phi_{wf} - \Phi_{wm}) \equiv \phi_m \left[S_{wm} (c_\phi + c_w)_m \frac{\partial p_{wm}}{\partial t} + \frac{\partial S_{wm}}{\partial t} \right] \quad (5.16)$$

$$\tau_o = \sigma k_m \lambda_{of/m} (\Phi_{of} - \Phi_{om}) \equiv \phi_m \left[S_{om} (c_\phi + c_o)_m \frac{\partial p_{om}}{\partial t} + \frac{\partial S_{om}}{\partial t} \right] \quad (5.17)$$

$$\tau_g = \sigma k_m \lambda_{gf/m} (\Phi_{gf} - \Phi_{gm}) \equiv \phi_m \left[S_{gm} (c_\phi + c_g)_m \frac{\partial p_{gm}}{\partial t} + \frac{\partial S_{gm}}{\partial t} \right] \quad (5.18)$$

where σ is the shape factor, τ is the transfer function, Φ is the potential, c is the compressibility, γ is the specific gravity and $\lambda_{\alpha f/m}$ is the upstream-weighted mobility of phase α (i.e. the upstream-weighting needs to be performed on the matrix and fracture of the same node).

The dual-permeability formulation for multiphase flow could not be found in a satisfying and complete way in any research or publication. Therefore, I expanded the single-phase dual-permeability formulation as presented in Gilman [2003]⁴³ with the help of above's formulation from Kazemi⁴² to obtain the following

$$\nabla (k\phi\lambda_\alpha)_f (\nabla\Phi_\alpha)_f - \tau_\alpha + \hat{q}_{\alpha f} = \phi_f \left[S_{\alpha f} (c_\phi + c_\alpha)_f \frac{\partial p_{\alpha f}}{\partial t} + \frac{\partial S_{\alpha f}}{\partial t} \right] \quad (5.19)$$

$$\nabla (k\phi\lambda_\alpha)_m (\nabla\Phi_\alpha)_m + \tau_\alpha + \hat{q}_{\alpha m} = \phi_m \left[S_{\alpha m} (c_\phi + c_\alpha)_m \frac{\partial p_{\alpha m}}{\partial t} + \frac{\partial S_{\alpha m}}{\partial t} \right] \quad (5.20)$$

where all the occurring variables have been explained above. The variable α can be either denoting oil, gas or water phase. The two equations are the continuity equations for the matrix and the fracture domains. Notice that both equations are coupled with a transfer term τ , which has opposite signs in both equations. This of course is important as to make sure that the formulation is consistent. The transfer function's form is explained above.

Limitations of the Dual Continuum Model

As the dual continuum models aims at being a model simplification of reality, there are several unresolved questions and limitations, when dealing with it.

Can the fractures be treated as a continuum?

In its general development Barenblatt assumed that the fracture system is sufficiently well developed. He also assumed that every flow block has a large number of fractures, which are all well inter-connected and therefore establishing a high-capacity flow conduit.

However, there are reservoirs where the fracture system is poorly inter-connected and are not continuous through the reservoir. For example, Cooke et al.[2006] have developed a sedimentary stratigraphy from core data and outcrop studies of carbonates in Texas and Wisconsin. She has observed that very often due to structural and mechanical reasons fractures tend to terminate at layer boundaries. Studies of fracture growth processes over time have also indicated that fractures not always form inter-connected continua.

Moreover, one also has to be critical of the assumption that the system of fractures is sufficiently well developed. Numerical studies and field studies indicate otherwise; fracture systems seldomly are well developed, many of them are in fact underdeveloped.

To sum up, users should be critical of treating the fractures as a continuum. Decisions need to be made on a case-to-case basis.

Shape factor

The concept of the shape factor was also introduced by Barenblatt, but has since experienced several changes or proposals for modified forms. In its original form it is a time-independent variable, that takes into account the geometry of matrix blocks to model the fluid or heat transfer between the matrix and the fracture blocks. The original formula for the shape factor is the ratio of a constant C and fracture spacing L to the square.

$$\sigma = \frac{C}{L^2}$$

In research literature (e.g., Warren and Root [1963], Kazemi et. al [1976], Coats [1989], Lim and Aziz [1995]) many different shape factors have been proposed and there is a lot of discussion about the physical meaning and the functional form of the shape factor among scholars. Table 11 presents some of the formulas proposed for the constant in the literature.

Set of fractures	Warren and Root	Kazemi and Gilman	Coats	Lim and Aziz
1	12	4	8	π^2
2	32	8	16	$2\pi^2$
3	60	12	24	$3\pi^2$

Table 11: Different shape factor constants in literature

In the above mentioned form the fracture spacing is constant. However, in reality the fracture spacing (i.e. or equivalently matrix block dimensions) may well be different in x-y-z directions. Therefore the above formula could also have a more complicated shape. Also it must be kept in mind that the above presented formula for the shape factor is valid just for a isotric permeability case; otherwise the shape factor formula should also take into account the permeability in x-,y-, and z-directions.

Others (e.g., van Heel et al. [2008], Rangel-German and Kovscek [2005]) have tried to define it as a function of time, because the shape factor works for a steady-state condition and significantly underpredicts early-time production from matrix blocks. Some researchers have even proposed that the shape factor should be a function of saturation, of mobility ratios and of the fracture-matrix oil interface area. Nowadays it is generally agreed upon that the shape factor

in its original form does not sufficiently take into account underlying recovery physics.

A problem in the practical application is the estimation of the numerical value of the shape factor. The question of how a discrete fractured model can be “translated” into a dual continuum model also poses certain intricacies. Although Warren and Root [1963] have derived a means of applying pressure transient tests to fractured reservoirs, the practical execution is difficult because many naturally fractured reservoirs do not exhibit their idealized behaviour. Often the shape factor is considered a history matching parameter. This approach is appropriate, however, users should be aware that the shape factor then just degrades to a fudge factor and loses its physical significance.

Characteristic lengths in fractured media?

The dual continuum model by definition assumes that properties like permeabilities, porosities or apertures among others have a characteristic length or representative elementary volume (REV). This means that those properties should follow Gaussian or log-normal distributions, which both have clearly defined mode, mean and other statistical parameters. This assumption is necessary to formulate the mathematical principles for the respective continua.

Unfortunately, recent studies (e.g., Bonnet et. al [2001], Gale [2002]) have shown that fractured reservoirs are best described by power laws and fractal geometries. Even though some fracture systems are best characterized by the above mentioned Gaussian and log-normal distributions, it is recognized that power law distributions are an excellent way for fracture system characterization. Unfortunately, power law distributions are in direct opposition to the continuum models, because they do not have a characteristic length scale (i.e. no physically sound average parameters can be obtained). For example, fracture permeability is related mathematically to the square of the fracture aperture; unfortunately, if the aperture follows a power law distribution then no fracture permeability can be calculated for the entire system. Geophysicists model fracture growth processes with certain growth laws that give rise to power law distributions in naturally fractured reservoirs. They believe that while homogeneous media have Gaussian and log-normal distribution of properties, the high degree of heterogeneity in fractured systems highly favours power law distributions (e.g., Barton and Zoback [1995]).

To sum up, the lack of a characteristic scale length means that a continuum formulation cannot be applied because the involved parameters do not behave that regular. Not being able to determine matrix block dimension or even difficulties in defining a “matrix block” makes the determination of a shape factor complicated. The major setback in dual continuum model simulations usually is the difficulty in determining the involved parameters.

Vita

Theodor Videnberg was born in Burgas, Bulgaria, on August 12, 1985, the son of Todor Temelkov Videnliev and Galina Laleva Decheva. He attended Europagymnasium Klagenfurt in Klagenfurt am Wörthersee, Austria, from 1996 to 2004. In the same year he entered Montanuniversität Leoben in Leoben, Austria, where he received the degree Bachelor of Science in Petroleum Engineering in June 2008. He immediately continued in the graduate program at Montanuniversität Leoben, pursuing a Master of Science degree in Petroleum Engineering. In the fall semester of 2008 he was a non-degree graduate exchange student at Colorado School of Mines in Golden, CO, U.S.A.

Permanent address:
Rosentalerstr. 74 / 22
9020 Klagenfurt am Wörthersee
Austria / E.U.
tvidenbe@gmail.com

This thesis was typed by the author.